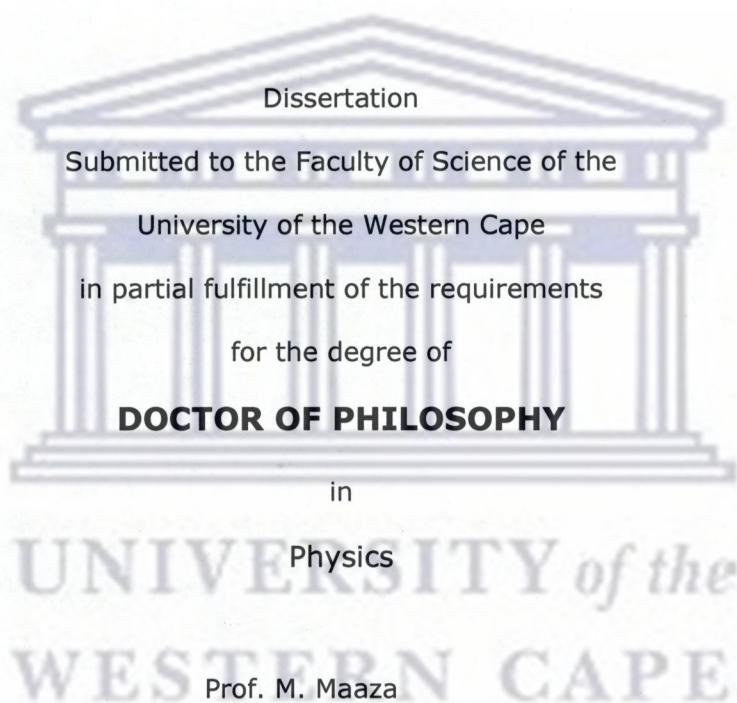


TOWARDS STIMULI-RESPONSIVE FUNCTIONAL
NANOCOMPOSITES: SMART TUNABLE
PLASMONIC NANOSTRUCTURES Au-VO₂

By

Jean Bosco Kana Kana



Advisor:

Prof. M. Maaza

Materials Research Department

iThemba LABS-NRF

Co-Advisor:

Prof. D. Knoesen

Department of Physics

University of the Western Cape

September 2010

ABSTRACT

The fascinating optical properties of metallic nanostructures, dominated by collective oscillations of free electrons known as plasmons, open new opportunities for the development of devices fabrication based on noble metal nanoparticle composite materials. This thesis demonstrates a low-cost and versatile technique to produce stimuli-responsive ultrafast plasmonic nanostructures with reversible tunable optical properties. Albeit challenging, further control using thermal external stimuli to tune the local environment of gold nanoparticles embedded in VO₂ host matrix would be ideal for the design of responsive functional nanocomposites. We prepared Au-VO₂ nanocomposite thin films by the inverted cylindrical reactive magnetron sputtering (ICMS) known as hollow cathode magnetron sputtering for the first time and report the reversible tuning of surface plasmon resonance of Au nanoparticles by only adjusting the external temperature stimuli. The structural, morphological, interfacial analysis and optical properties of the optimized nanostructures have been studied. ICMS has been attracting much attention for its enclosed geometry and its ability to deposit on large area, uniform coating of smart nanocomposites at high deposition rate. Before achieving the aforementioned goals, a systematic study and optimization process of VO₂ host matrix has been done by studying the influence of deposition parameters on the structural, morphological and optical switching properties of VO₂ thin films. A reversible thermal tunability of the optical/dielectric constants of VO₂ thin films by spectroscopic ellipsometry has been intensively also studied in order to bring more insights about the shift of the plasmon of gold nanoparticles imbedded in VO₂ host matrix.

Keywords: Vanadium dioxide; Transition temperature; Thermochromism; Optical constants; Gold nanoparticles; Nanocomposites; Thermal stimuli-responsive; Plasmons; Inverted cylindrical reactive magnetron sputtering

DECLARATION

I, the undersigned, hereby declare that the work contained in this Ph.D. thesis is my own original work, that it has not been previously submitted for any degree or examination in any other university, and that all the sources I have used or quoted have been clearly indicated and acknowledged by complete references.

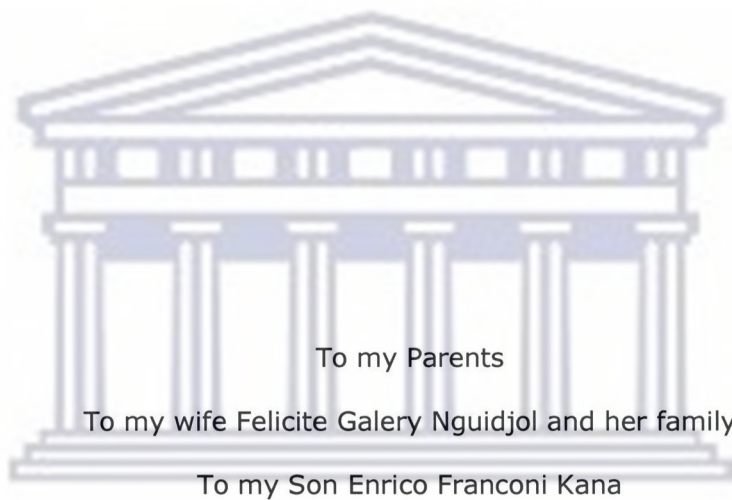
Jean Bosco Kana Kana

Signature:

Date:



UNIVERSITY *of the*
WESTERN CAPE



To my Parents

To my wife Felicite Galery Nguidjol and her family

To my Son Enrico Franconi Kana

UNIVERSITY *of the*
WESTERN CAPE

ACKNOWLEDGEMENTS

First and foremost, I thank Prof. Malek Maaza, my advisor for giving me the opportunity and resources to work at the forefront of experimental Nanoscience, and above all for teaching me how to experiment, analyze, think, write, and speak like a great physicist.

I am grateful to Prof. Dirk Knoesen my co-advisor who accepted to promote and guide this thesis.

I am much obliged to Prof. Reginaldt Madjoe for always encouraging me and also for supporting my application in May 2007, which I understand, was very late.

I am also grateful to Prof. Rob Lindsay for writing me a letter for Home Affairs for the extension of my visa during the absence of the Head of Department.

My gratitude to Dr. Rudzani Nemutudi, Head of Materials Research Department, for his help and advice in the Atomic Force Microscopy and also his continuous assistance in all my financial troubles encountered during my graduate years.

I am extremely grateful to Dr Paul Motalane for renewing my ALC bursary 2009.

I thank Prof. A.C. Beye former CEO of African Laser Centre for taking me under his wing and for sharing his knowledge through countless fruitful discussions.

I am also very grateful to Vilakazy Zebon, Managing Director of iThemba LABS for contributing to the NRF top up bursary.

I am especially indebted to Dr. Hdr. J.M. Ndjaka who provided me the opportunity to join the active research team of Prof. M. Maaza.

My gratitude is to Dr. A.Y. Fasasi and Dr. N. Manyala, Dr. O. Nemraoui, Dr B.D. Ngom who more than once, helped me with some scientific discussions. I credit also Dr. Remy Bucher who always is available for discussion in crystal structure and XRD patterns of this multiphase nanomaterial.

My recognition is to other all kind persons whose expertise was important in different stages of this project. Thanks to Prof. Alain Gibaud for his scientific expertise and

fruitful discussion in the X-ray reflectivity characterization. To Dr. Guillaume Vignaud for his help with detailed and time-consuming ellipsometry measurements at different temperatures of VO₂ sample. I also thank my collaborators Dr. Sylvain Halindintwali and Prof. Tchoula Tchokonte for his fruitful scientific discussions.

The technical support of Karl Springhorn and Jan Crafford is highly appreciated.

My acknowledgments are also to all members of Materials Research Department for their help, support and hospitality.

Special Thanks are to Dianne Smith for always booking my flight ticket and arranging my accommodation and also Mirencia Da Silva for her expertise and support for obtaining of my study permit in Home Affairs-Paarl. I am grateful to Msiza Barney for his kind support and Davids Lindsay for transport arrangement. I also thank Ms Angela Adams secretary of Physics Department at UWC for always helping me with the registration issues.

I salute all my fellow students, after all, we have shared "walls" for years now, and I will not forget our Abafundi and other activities. For many invigorating discussions, whether scientific or not, I thank all my colleagues and friends at MRD and elsewhere.

My thought also goes to my family back home in Cameroon. My mom, my dad, and my brothers and sisters, have always been very supportive, which has made me forget about the distance. In addition, I thank my wife Felicite Galery for everything, for her patience, love and her strategies to handle troubles during my graduate years. Special thank is to my son Enrico Franconi Kana who was born when I was traveling to Italy for scientific visit. I thank all my friends in USA especially G. Biyogmam, J.C. Chokomakoua and B. Fongang for their encouragement and support.

Finally, I thank Prof. Giacinto Scoles and Dr. Loredana Casalis for hosting me at SENIL-Trieste, Italy and introducing me in Nanotechnology related to biological applications.

This work was made possible by the following funding agencies: the African Laser Centre (ALC) and also Nanoscience African Network (NANOAFNET).

TABLE OF CONTENTS

	Page
ABSTRACTii
DECLARATIONiii
DEDICATIONiv
ACKNOWLEDGEMENTS.v
LIST OF FIGURES	xiii
LIST OF TABLES	xvii
PREFACE1
CHAPTER	
1. LITERATURE REVIEW OF VO₂5
Abstract5
1.1. State of the art in VO ₂5
1.1.1. Phase diagram for VO ₂8
1.1.2. Lattice and electronic structures of VO ₂9
1.1.3. Transition mechanism: Peierls or Mott Hubbard?..12
1.1.4. VO ₂ : Latest findings in Metal-insulator transition.....16
1.2. VO ₂ : Phase transition characteristics20
1.3. VO ₂ thin films: common deposition techniques20
1.4. Deposition Method chosen21
1.5. References22
2. PLASMON RESONANCES OF NANOGOLD OR SILVER PARTICLES & REVIEW OF WORLDWIDE RESEARCH IN Ag (Au)-VO₂.26
Abstract26
2.1. Physics of plasmon resonance26
2.1.1. Quasi-static approximation29
2.2. Mie theory33

2.3. Factors governing the plasmon resonance	34
2.3.1. Size and temperature dependence of the plasmon resonance.	34
2.3.2. Shape effects in plasmon resonance.	35
2.3.3. Interparticle coupling resonance effects.	35
2.3.4. Local refractive index dependence of plasmon resonance.	35
2.4. Applications of plasmonics	36
2.5. Review of worldwide research in Ag (Au)-VO ₂	37
2.6. References	40
3. EXPERIMENTAL TOOLS AND TECHNIQUES	43
Abstract	43
3.1. Sputtering.	43
3.1.1. Introduction.	43
3.1.2. Principles.	44
3.1.3. Characteristics of RF magnetron sputtering.	47
3.1.3.1. Ionic frequency.	47
3.1.3.2. Auto polarization.	49
3.1.3.3. Magnetron sputtering	49
3.1.4. The Sputter Parameters.	49
3.2. Choice of the deposition method of VO ₂ and Au-VO ₂ thin films.	50
3.3. RF- Inverted cylindrical magnetron sputtering (ICMS)	51
3.3.1. ICMS features.	51
3.3.2. Description.	51
3.4. Comparison of conventional methods and new method ICMS.	54
3.5. Characterization techniques.	55
3.5.1. Atomic force microscopy.	55
3.5.1.1. Principles.	56
3.5.1.2. AFM measurements and possible error sources.	58

3.5.2. Conductive Atomic Force Microscopy (C-AFM).	61
3.5.2.1. Background.	61
3.5.2.2. Equipments used.	63
3.5.3. Scanning Tunneling Microscopy (STM).	63
3.5.3.1. Background.	63
3.5.3.2. Applications of the STM.	64
3.5.4. Scanning Tunneling Spectroscopy.	66
3.5.4.1. Background.	66
3.5.4.2. Equipments used.	68
3.5.5. X-RAY Reflectivity.	69
3.5.5.1. Basic principles of X-ray reflectivity.	70
3.5.5.2. Equipments used.	73
3.5.6. X-RAY Diffraction.	73
3.5.6.1. Principle and pattern analysis.	73
3.5.6.2. Equipments used.	74
3.5.7. UV-Vis-NIR Spectroscopy.	75
3.5.7.1. Principles	75
3.5.7.2. Optical transmission measurements	75
3.5.7.3. Equipment used	76
3.5.8. Spectroscopic Ellipsometry.	76
3.5.8.1. Background.	76
3.5.8.2. Basic equations of ellipsometry.	77
3.5.8.3. Problems and sources errors.	79
3.5.8.4. Data Analysis for spectroscopic ellipsometry.	79
3.5.8.5. Equipement used	80
3.5.9. Rutherford Backscattering Spectroscopy.	80
3.5.9.1. Principles	80

3.5.9.2. Equipement used	83
3.6. References.	84
4. THICKNESS INDUCED DRASTIC REDUCTION OF PHASE TRANSITION TEMPERATURE IN SPUTTERED VO₂ THIN FILMS	86
Abstract	86
4.1. Introduction	87
4.2. Experimental details	88
4.2.1. Sample preparation.	88
4.2.2. Sample characterization.	88
4.3. Results and discussion	88
4.3.1. Optical transmittance.	88
4.3.2. Thermal hysteresis and phase transition temperature.	90
4.4. Conclusion	92
4.5. References	92
5. HIGH SUBSTRATE TEMPERATURE INDUCED ANOMALOUS PHASE TRANSITION TEMPERATURE SHIFT IN SPUTTERED VO₂ THIN FILMS.	94
Abstract	94
5.1. Introduction	95
5.2. Experimental details	97
5.2.1. Sample preparation.	97
5.2.2. Sample characterization.	98
5.3. Results and discussion	98
5.3.1. Structural Properties.	98
5.3.2. Surface-morphological properties.	99
5.3.3. Optical properties	101
5.3.3.1. Optical transmittance.	101

5.3.3.2. Thermal hysteresis.	101
5.3.3.3. Tunability of the phase transition temperature.	103
5.4. Conclusion	105
5.5. References	106
6. PHASES COEXISTENCE IN VO₂ REVEALED BY CONDUCTIVE	
ATOMIC FORCE MICROSCOPY	108
Abstract	108
6.1. Introduction	109
6.2. Experimental details	111
6.3. Results and discussion	111
6.3.1. Surface topography	111
6.3.2. Band-gap of VO ₂ nanograin	111
6.4. Conclusion	114
6.5. References	115
7. THERMALLY TUNABLE OPTICAL CONSTANTS OF VO₂ THIN FILMS	
MEASURED BY SPECTROSCOPIC ELLIPSOMETRY.	117
Abstract	117
7.1. Introduction	118
7.2. Experimental details	120
7.2.1. Samples preparation.	120
7.2.2. Spectroellipsometric measurements and data analysis.	121
7.3. Results and discussion	124
7.3.1. Optical constants.	124
7.3.2. Dielectric constants	128
7.3.3. Optical conductivity	131
7.4. Conclusion	133
7.5. References	134

8. THERMOCHROMIC NANOCRYSTALLINE Au-VO₂ COMPOSITE THIN FILMS PREPARED BY RADIOFREQUENCY INVERTED CYLINDRICAL MAGNETRON SPUTTERING.	137
Abstract	137
8.1. Introduction	138
8.2. Experimental details	141
8.2.1. Samples preparation.	141
8.2.2. Samples evaluation.	143
8.3. Results and discussion	144
8.3.1. Film structure.	144
8.3.2. Film surface morphology	146
8.3.3. Surface and interface analysis.	148
8.3.4. Plasmonic properties	149
8.3.4.1. Surface plasmon resonance wavelength shift and thermo- chromic behaviour	149
8.3.4.2. Surface plasmon resonance hysteresis.	153
8.4. Conclusion	155
8.5. References	156
9. CONCLUSIONS AND OUTLOOK	160

LIST OF FIGURES

Figure	Page
1.1	Crystallographic structures of vanadium dioxide (VO ₂).. 6
1.2	Variation of VO ₂ electrical resistivity with temperature. 7
1.3	Phase diagram for the vanadium-oxygen system. 8
1.4	VO ₂ unit cells above and below the phase transition. 9
1.5	Orientation and dimensions of tetragonal/rutile R. 10
1.6	Energy-level diagram of VO ₂ 12
1.7	Sketch of Peierls mechanism. 13
1.8	Images of near-field scattering amplitude over the same 4 μm x 4 μm area obtained by s-SNIM operating at IR frequency $\omega = 930 \text{ cm}^{-1}$ 18
2.1	Schematic of the simplest mode of collective oscillation of the conduction electrons relative to the nuclei of a metal NP, the dipolar particle plasmon.. . 28
2.2	Lycurgus Glass cup Byzantine empire 4 th century A.D. 29
2.3	Small particle in host medium and under the applied electric field of x- polarized plane wave. 30
3.1	Plasma color during the deposition of VO ₂ by Inverted Cylindrical Magnetron sputtering located at Materials Research Department-iThemba LABS. 45
3.2	Sputtering mechanisms: a) Simple collision; b) Collisional cascades; c) thermal porosity. 46
3.3	Ionic frequency as a function of ion mass. 48
3.4	Schematic illustration of the Inverted Cylindrical Magnetron (ICM) sputter gun. 52
3.5	Schematic illustration of the sputter deposition system showing the ICMS.. . 53
3.6	An explicative cartoon of AFM working principle.. . . . 58
3.7	Typical schematic of Conductive Atomic Force Microscopy 62

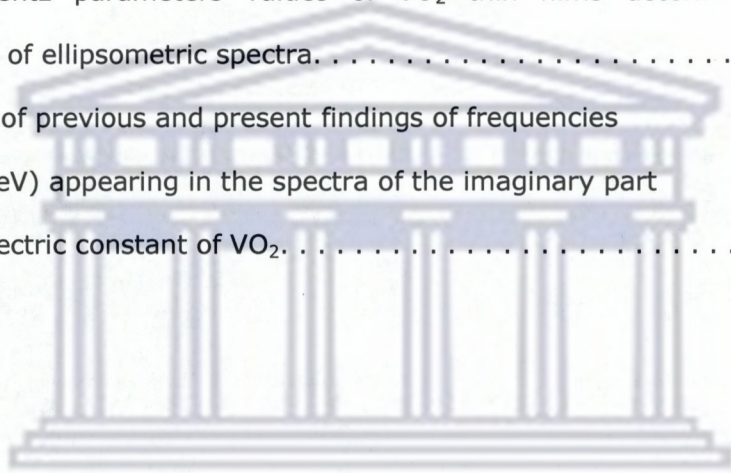
3.8	Typical schematic of Scanning Tunneling Microscopy.	67
3.9	Illustration of the setup of X-ray reflectivity.. . . .	72
3.10	Schematic of the geometry of an ellipsometry experiment.	77
3.11	The four parameters that define the ellipse of polarization in its plane are the azimuth Ψ , the ellipticity $e = a/b$, the total amplitude A and the absolute phase θ	78
3.12	The RBS spectrum of Au-VO ₂ deposited on corning glass substrate at 450 °C by ICMS.	82
3.13	The RBS spectrum of pure VO ₂ thin film deposited on Soda lime glass substrate at 450 °C by ICMS	83
4.1	Spectral transmittance for the semiconductor phase measured at 20 °C (solid line) and metal phase at 85 °C (dashed line) of VO ₂ thin films deposited at different thicknesses	89
4.2	Thermal hysteresis loops of transmittance at wavelength of 1100nm for VO ₂ thin films deposited at different thicknesses.	91
5.1	Indexed XRD spectra of VO ₂ monoclinic (JCPDS 43-1051) films deposited on normal microscope glass substrate at substrate temperatures (Ts) of 450 and 600 °C.. . . .	98
5.2	Atomic force microscopy (AFM) images of 5x5 μm^2 area of VO ₂ thin film surface prepared at 450 °C (a) and 600 °C (b).	100
5.3	Spectral transmittance for the semiconductor phase measured at 20 °C (solid line) and metal phase at 100 °C (dashed line) of VO ₂ thin films deposited at different substrate temperatures.	102
5.4	Thermal hysteresis loops of transmittance at wavelength of 1100 nm for VO ₂ thin films deposited at different substrate temperatures ranging from 450 to 600 °C.	103
5.5	Variation of the transition temperature and hysteresis width of VO ₂ film	

	as a function of substrate temperature.	104
6.1	Topography (A) and current (B & C) image of a VO ₂ thin film of 150 nm on Corning glass substrate sample at a bias of 1.5 volts, 25 pA, 1 μm scan size. (B) Current image at 65 °C and (C) at 85 °C	113
6.2	Corresponding I-V curves recorded at two specific points representing the insulating (brown color) and metallic regions (blue color) as indicated in Fig 6.1C.	114
7.1	Schematic model of the VO ₂ thin film on Corning glass substrate used to fit the ellipsometric spectra.	122
7.2	(a) Refractive index, n and (b) extinction coefficient, k of sputtered VO ₂ thin films at temperature below and above the phase transition temperature of 70 °C determined by variable angle spectroscopic ellipsometry.	126
7.3	Variation of optical constants (refractive index, n (a) and extinction coefficient, k (b)) at wavelengths 497 nm (visible region), 1033 and 1459 nm (near-infrared region) as a function of external temperature stimuli of sputtered VO ₂ thin films.	127
7.4	(a) Real and imaginary part of dielectric function of VO ₂ thin films below, at and above the phase transition temperature T _c = 70 °C. (b) Thermal hysteresis behavior of the real part of the dielectric function of sputtered VO ₂ thin films.	130
7.5	Real part of the optical conductivity of VO ₂ thin films as a function of frequency for various external temperatures stimuli. The open circle shows the isosbetic (equal conductivity) point for all spectra. The inset shows the temperature dependence of the peak position (range of 3.0-3.5 eV) and its width of the real part of the optical conductivity. The straight lines in the inset are only used to guide the eyes.	133

8.1	Schematic illustration of the inverted cylindrical magnetron (ICM) sputter gun. The target is the cylindrical ring vanadium metal in which a triangular slice of gold was stuck..	143
8.2	Indexed XRD patterns of Au-VO ₂ nanocomposites (background-subtracted; JCPDS 82-661 for VO ₂ monoclinic and JCPDS 04-0784 for gold face-centered cubic Fm3m) films sputtered at different substrate temperature ranging from 400 °C to 600 °C..	145
8.3	Relationship between the substrate temperature and the particle sizes of Au (square) and VO ₂ (dot) estimated from Scherrer's formula.	146
8.4	AFM topographic images of samples sputtered at substrate temperatures (a) 400 °C; (b) 600 °C	147
8.5	X-ray reflectivity profile of Au-VO ₂ thin film on Corning glass substrate sputtered at 550 °C. The circles correspond to the experimental data and solid line the simulation.	149
8.6	Optical transmittance (%) of Au-VO ₂ thin films sputtered onto Corning glass At different substrate temperatures for spectra taken at temperature below and above the transition temperature (T _c = 68 °C) of the host matrix VO ₂ . .	152
8.7	Transmittance at a wavelength of 1100 nm for Au-VO ₂ thin films sputtered at 400 °C and 600 °C as a function of the external temperature stimuli.. . .	153
8.8	Absorbance spectra of the Au-VO ₂ nanocomposite films sputtered at 400 °C and 600 °C. Measurements taken below and above the transition temperature T _c = 68 °C.	154
8.9	Variation of surface plasmon resonance wavelength as function of external temperature stimuli of Au-VO ₂ samples sputtered at 400 °C and 600 °C. . .	155

LIST OF TABLES

Table	Page
3.1 Comparison of conventional methods and new method by ICMS for preparing nanocomposites films.	54
3.2 Comparison and the characteristics of common microscopes	68
4.1 Values for the transition temperature and hysteresis width for each film thickness.	91
7.1 Drude-Lorentz parameters values of VO ₂ thin films determined from the simulation of ellipsometric spectra.	124
7.2: An outline of previous and present findings of frequencies of peaks (eV) appearing in the spectra of the imaginary part of the dielectric constant of VO ₂	128



UNIVERSITY *of the*
WESTERN CAPE

Preface

The last decade has brought enormous progress in the area of tunable noble metal nanoparticles (NPs) optical properties. An understanding of the optical properties of noble metal NPs holds both fundamental and practical significance. Fundamentally, it is important to systematically explore nanostructure characteristics that cause optical property variation as well as provide access to regimes of predictable behaviour. Practically, the tunable optical properties of nanostructures can be applied as materials for surface enhanced spectroscopy, optical filters, waveguides, biological labels sensors and metamaterials. In all of these cases, the optical property of interest is the localized surface plasmon resonance (LSPR). The LSPR condition is fulfilled when a specific wavelength λ of light impinges on the nanostructure, generating enhanced electromagnetic fields that are localized at the surface of the nanostructure. The λ of light that excites the collective oscillation of conduction electrons is absorbed and scattered by the NPs with tunable surface plasmon resonance. Research on nanocomposites in this era aims at developing materials with outstanding properties so called smart functionalities. The synthesis of such nanomaterials involves challenges in the quality, quantity, variety, and integrated design. The quality challenge requires developing and synthesizing promising nanomaterials with sufficiently high purity and freedom from defects that their ultimate properties can be reliably measured and

accurately known. The quantity challenge requires developing, understanding, and optimizing synthesis method for economical, large-scale production of nanomaterials. Readily scalable and low-cost methods for producing large quantities of sufficiently high-quality nanomaterials are needed. The variety challenge requires research and development of methods to efficiently explore and expand the library of “building blocks” of enhanced nanomaterial properties that are potentially available for use. The integrated design and assembly (or “nano-to-bulk”) challenge requires developing synthesis methods that are compatible with the subsequent or concurrent assembly of nanomaterials into systems or architectures that exhibit the greatly enhanced nanoscale properties at the macroscale. With these goals, basic research is clearly the central need for the synthesis of practical nanomaterials leading to fabrication / processing and system-design techniques that preserve unique nanoscale properties while coupling them to the macroscale.

Motivation and objectives

From the scientific and technological point of view, it is also interesting to study nanostructured materials, either because their properties may be modified as a function of the particle size, or because the particles interact with a surrounding matrix material, or both. Those smart materials whose mechanisms are based on phase transitions, such as metal-semiconductor transformations, are particularly intriguing, since the associated property changes when induced by external perturbations can be rapid, reversible, and may span several orders of magnitude. This is certainly true for the specific case of the vanadium dioxide, VO_2 and Au- VO_2 composite films.

The main objective of this research has been to explore physical properties of thin solid films materials and to carry out fundamental research studies for describing the relationship between growth parameters, structure / composition and physical properties of thermochromic VO_2 and smart multifunctional nanoplasmonic Au- VO_2 .

Aims of this Thesis

The fascinating optical properties of metallic nanostructures, dominated by collective oscillations of free electrons known as plasmons, open new opportunities for the development of fundamentally new metal-based sub-wavelength optical elements with broad technological potential. Albeit challenging, further control using external stimuli to direct the ordering and local environment of nanoparticles would be ideal for the design of responsive functional nanocomposites. An aim of this thesis is to develop a new strategy to fabricate functional plasmonic nanostructures Au-VO₂ which exhibit a thermal stimuli response. A further aim is to characterize the optimized nanostructures in order to carry out the structural, morphological, interfacial and optical properties of the latter and also to understand the properties of these optically active nanosystems.

Structure of this Thesis

Chapter 1 gives the state of the art in VO₂ bulk and thin films as well as some latest findings on its phase transition. Its spectacular solid-solid phase transition or thermal induced metal-insulator phase transition remains a highly researched topic over a half a century.

Chapter 2 is dedicated to exploring the physics of plasmon resonances of noble metal nanoparticles such as Au or Ag, as well as to studying the effects of different factors governing plasmon resonance. The chapter closes with a review of research works done for Ag (Au)-VO₂.

Chapter 3 is dedicated to describing the experimental procedure used to fabricate the samples and to explain the different techniques employed throughout this work to characterize their structure, morphology and optical properties.

Chapter 4 investigates the effect of thickness on the reduction of the phase transition temperature of sputtered VO₂ thin films. The drastic reduction of T_c from 70 °C to 50 °C as thickness increases from 60 nm to 200 nm was clearly observed.

Chapter 5 reports the anomalous phase transition shift induced by high substrate temperatures. A sizeable variation of ~ 10 °C towards higher temperature with increasing substrate temperature (T_s) was observed for undoped VO₂ thin films.

Chapter 6 reports a systematic investigation of the phase's coexistence in the thermochromic VO₂ material. Conductive atomic force microscopy (C-AFM) clearly revealed the nanoscale metallic puddles that appear at the metal-insulator phase transition.

Chapter 7 reports an ellipsometric spectroscopy study of VO₂ thin films. The thermal controllable reversible tunability of optical constants (refractive index and extinction coefficient) of VO₂ thin films has been investigated. The dielectric constants and optical conductivity have been reported and compared to those reported in the literature.

Chapter 8 reports the synthesis and feasibility of reliably reproduced high quality of Au-VO₂ by a novel physical vapor deposition named inverted cylindrical magnetron sputtering (Hollow cathode sputtering). Structural, morphological, interfacial analysis and optical properties of synthesized Au-VO₂ nanocomposite thin films have been carried out and our results have been compared by other conventional techniques.

Chapter 9 summarizes the aforementioned work done and highlights the outlook for their possible extension of this research project.

Chapter 1

LITERATURE REVIEW OF VO₂

Abstract

This chapter is meant to familiarize the reader with vanadium dioxide (VO₂) and its phase transition, including the latest findings related to the phase transition mechanisms of VO₂ as well as its common deposition methods. The review of the phase transition characteristics and factors influencing them are treated in details, in order to provide the basis for interpreting some of the experimental results of the current work.

1.1 State of the Art in VO₂

Vanadium dioxide (VO₂) has been perennial in theoretical and experimental condensed-matter and materials research for half a century [1]. Bulk VO₂ crystals exhibit a semiconductor to metal transition (SMT), also widely known as the metal-insulator transition (MIT), at a critical temperature of $T_c = 68\text{ }^\circ\text{C}$, accompanied by a first-order structural phase transformation from a monoclinic (M_1 -P2₁/c) for low-temperature semiconductor to a tetragonal (rutile-P4₂/mnm) structure for the high-temperature metal [2] characterized by a small lattice distortion along the c-axis. The two crystallographic structures are illustrated in Figure 1.1. In fact, it is the intricate interplay between electronic and structural degrees of freedom between carrier

localization due to electron-electron repulsion (Mott-Hubbard correlation) [3,4] and unit-cell doubling due to lattice instability (Peierls distortion) [3,4] that has been at the heart of an enduring debate [5-7, 8, 9-16] about the precise cause and effect linkage in the mechanism of the VO_2 transition.

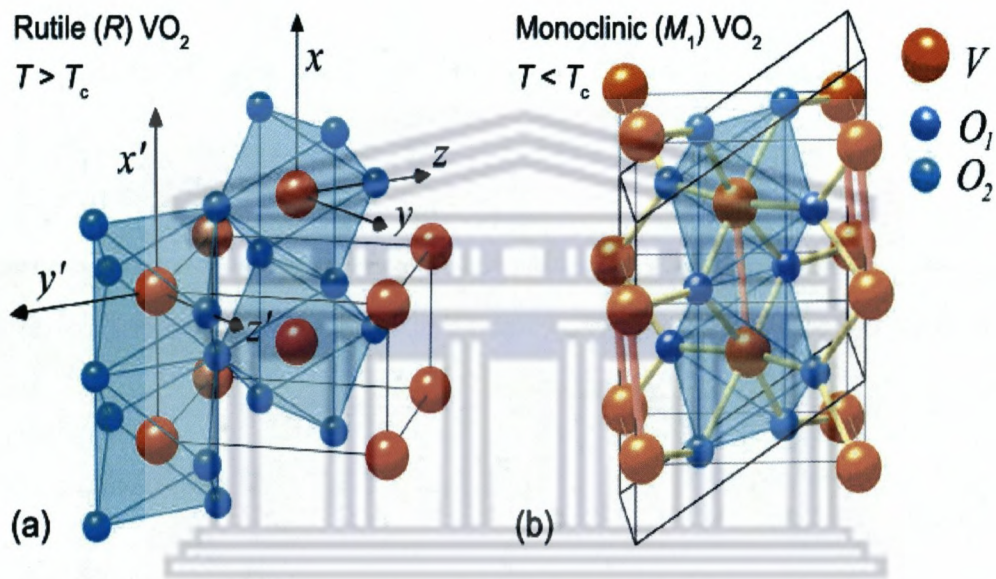


Figure 1.1: Crystallographic structures of vanadium dioxide (VO_2): (a) Tetragonal/rutile (R), above the transition temperature T_c , and (b) monoclinic M_1 below T_c . Large and small spheres denote vanadium (V) and (two different types of M_1) oxygen (O) atoms, respectively. Shaded regions outline edge- and corner-sharing oxygen octahedra; the two local coordinate systems in (a) reflect the different orientation of octahedra centered at corners and in the center of the R cell. In (b), note the V-V pairing and tilting in the M_1 phase along the vertical direction, as well as the doubling of the M_1 unit cell (darker bounding lines) with respect to the R unit cell (lighter bounding lines and (a)) [20].

As a transition-metal oxide with narrow d-electron bands, this strongly correlated electron system is extremely sensitive to small changes in extrinsic parameters such as temperature, pressure, or doping [10,17-20]. The first-order phase transition is accompanied by an abrupt change in resistivity of several orders of magnitude, as well as its sharp change electrical in the near-infrared region [21-23] as illustrated in figure 1.2. In bulk crystals, the change in resistivity is of the order of $10^3 - 10^5$ with a hysteresis width of ~ 1 °C [22]. In thin films, on the other hand, the hysteresis widths may be of the order of 10-15 °C; [24] in nanoprecipitate VO_2 , the hysteresis widths may be even larger [25].

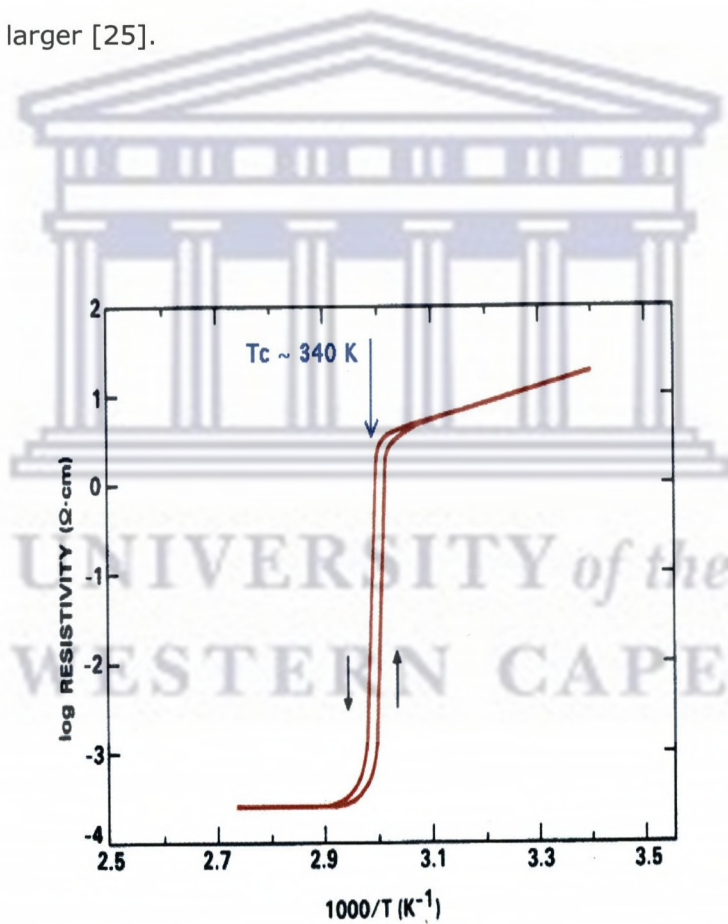


Figure 1.2: Variation of VO_2 electrical resistivity with temperature.

The change in resistivity is of the order of $10^3 - 10^5$ with a hysteresis width of ~ 1 °C [22].

1.1.1. The phase diagram for VO₂

Vanadium, a transition-metal, is known to exist in different valence states and, consequently, to have many possible oxides. The oxides where all of the vanadium atoms have the same valence are well known: VO, VO₂, V₂O₃, and V₂O₅, but there are also oxides where the vanadium atoms have different valences: between V₂O₃ and VO₂, the series of Magneli phases V_nO_{2n-1} (n > 1) and also V₄O₉, V₆O₁₃ and V₃O₇ [26]. In addition to VO₂, many of these vanadium oxides also exhibit metal-insulator transitions at critical temperatures specific to their stoichiometric phases; as depicted in Figure 1.3, do not exhibit any metal-insulator transition such as V₂O₅, V₇O₁₃, V₅O₉, V₃O₅, and V₆O₁₁. Among these numerous oxides, VO₂ is of special interest given the existence of a solid-solid phase transition at T_c = 68 °C with sharp switching properties aforementioned.

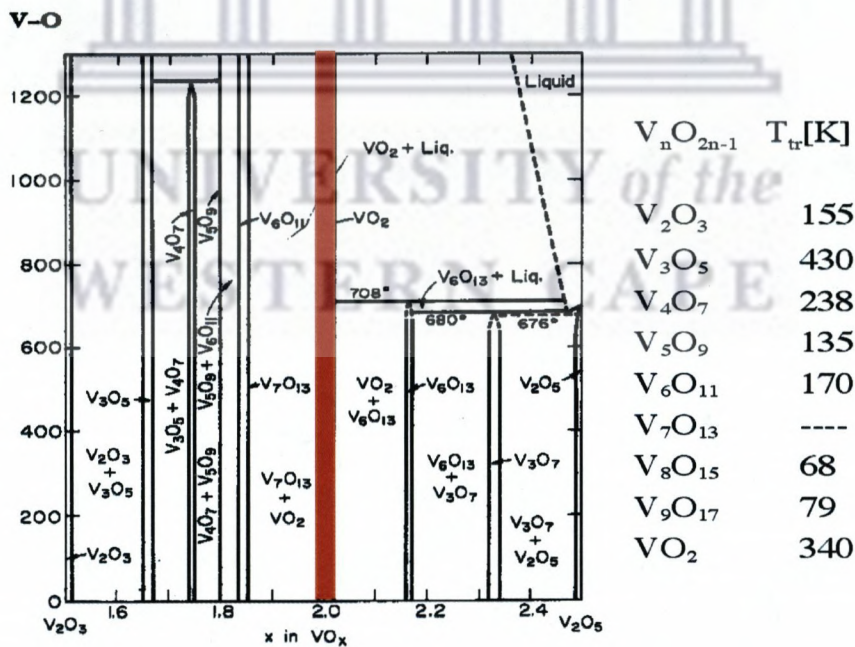


Figure 1.3: Phase diagram for the vanadium-oxygen system. It gives the corresponding phase transition temperatures of several vanadium oxides [27].

1.1.2. Lattice and electronic structures of VO₂

Above the transition temperature T_c , the R-phase of VO₂ exhibits the characteristics of a metal and has a tetragonal body-centered unit cell of vanadium (V) atoms, each surrounded by an orthorhombically distorted octahedron of six oxygen (O) atoms. The octahedra stack by sharing edges that form chains along the c-axis, which are in turn coupled to each other by sharing corner O atoms. The closest V-V distance is 2.85 Å in chains along the c-direction (Figures 1.1, 1.4, and 1.5). Below T_c , the M₁ phase of VO₂ is a monoclinic semiconductor with a ~ 0.7 -eV optical bandgap [8, 23, 28, 29-30] and a distorted structure (Figures 1.1, 1.4, and 1.5): the V atoms pair/dimerize along the chain, resulting in unit-cell doubling, and also tilt transversely in a zigzag-like fashion; the V-V pairing and tilting also cause the O-octahedra to distort and twist slightly [20].

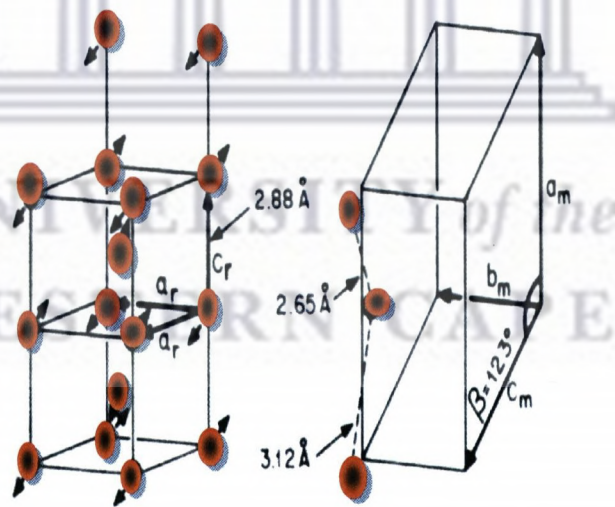


Figure 1.4: VO₂ unit cells above (left) and below (right) the phase transition [23].

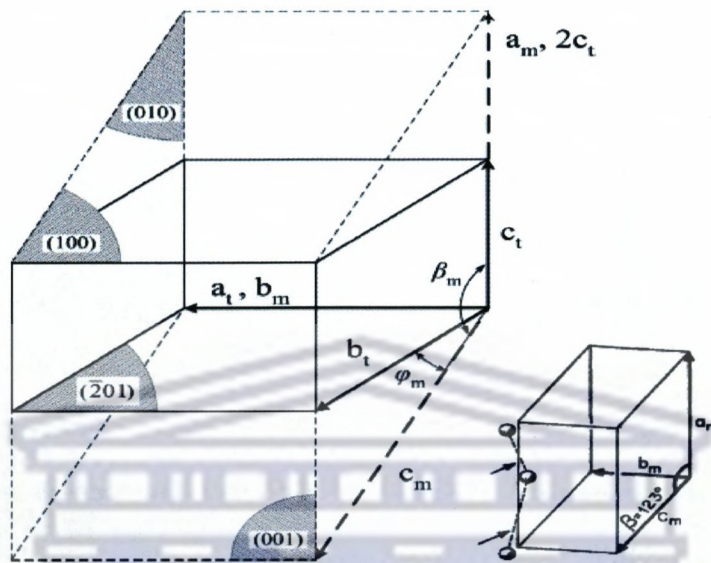


Figure 1.5: Orientation and dimensions of tetragonal/rutile R (solid lines, "t" subscripts) and monoclinic M_1 (dashed lines, "m" subscripts) unit cells of VO_2 ; several crystallographic planes for M_1 are also indicated. According to Eyert [20] (and references therein), the lattice parameters are: for the R phase, $a_t = b_t = 4.5546 \text{ \AA}$, $c_t = 2.8514 \text{ \AA}$, axial = 90° ; for the M_1 phase, $a_m = 5.7517 \text{ \AA} = 2c_t$, $b_m = 4.5378 \text{ \AA}$, $c_m = 5.3825 \text{ \AA}$, $\beta_m = 122.646^\circ$. Note again the doubling of the monoclinic cell along the rutile c-axis, i.e., $a_m = 2c_t$. (inset) Metal-metal pairing and tilting in the M_1 phase result in two different V-V distances along the monoclinic a-axis: 2.619 \AA and 3.164 \AA [31].

The essential structural and electronic details of both VO_2 phases, first proposed by Goodenough [8] are neatly summarized by Cavalleri et al. [32]. The $V([Ar]4s^23d^5)$ atoms, each bound to two $O(1s^22s^22p^4)$ atoms, cede four electrons to the O 2p shells, leaving V^{4+} cations with a single valence electron near the Fermi level. The closed-shell

2p electrons of the O atom are now tightly bound and lie well below the Fermi level, not contributing significantly to the conductivity. The remaining one electron per V^{4+} cation occupies the lowest of the 3d levels, making VO_2 a $3d^1$ compound. The bands in transition-metal compounds form under the strong influence of anisotropic crystal fields. The fivefold energy-degenerate 3d levels of the isolated V^{4+} cation are split in VO_2 by the cubic and orthorhombic components of the octahedral field of the six surrounding oxygens [9] resulting in a higher-energy two-level manifold (e_g) and a lower-energy three-level manifold (t_{2g}). The t_{2g} states, located near the Fermi energy, are split into a $3d_{//}$ state, which is directed along the rutile c-axis with good metal-metal bonding, and the remaining $3d_{\perp}$ states. Thus, a single electron resides in the lowest vanadium d band, $3d_{//}$, which is the reason for R-phase VO_2 being metallic. In the monoclinic M_1 phase, V-V pairing within the chains parallel to the rutile c-axis causes splitting of the $3d_{//}$ band into filled bonding and empty antibonding states. In addition, the $3d_{\perp}$ bands move to higher energies due to increased overlap of these states with the O 2p states, caused by the zigzag-like tilting of the V-V dimers. As a result, a bandgap of ~ 0.7 eV opens between the bonding $3d_{//}$ band and the other t_{2g} bands (Figure 1.6); the $3d_{//}$ band splitting amounts to ~ 2.5 eV, while the $3d_{\perp}$ band is raised by ~ 0.5 eV [29].

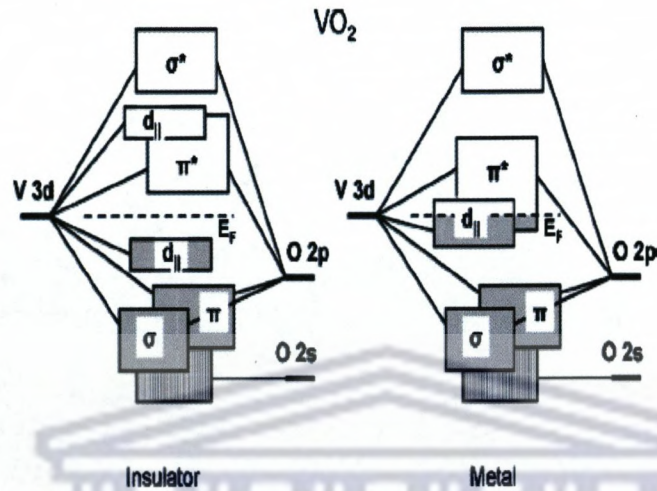


Figure 1.6: Energy-level diagram of VO₂: each V atom is left with one valence electron, while ceding four to fill the O 2p shell, which becomes tightly bound; the near-Fermi level states are those of the t_{2g}-like manifold, where the 3d_{//} levels are split in the M₁ phase by unit-cell doubling (Peierls mechanism) and /or by Coulomb repulsion (Mott-Hubbard mechanism); the higher-lying 3d_π states shift in the M₁ phase due to the structural distortion [33].

1.1.3. Transition mechanism: Peierls or Mott Hubbard?

The d¹ configuration of the V⁴⁺ cation allows a single electron to be shared by the 3d_{//} and 3d_π bands (Figure 1.6). Because of their different widths and anisotropies (3d_{//} is highly anisotropic while 3d_π is more spherical), these two bands are expected to respond in a different way either to electron-electron interactions (significant only for the narrow 3d_{//} band) or to a lattice distortion [10]. Within Goodenough's phenomenological model [8] the lattice distortion (tilting) in the VO₂ M₁ phase raises the antibonding 3d_π band above the Fermi level and leaves the 3d_{//} band half filled. The point of contention as regards the VO₂ transition mechanism is whether the

additional splitting of the $3d_{//}$ band originates from V-V pairing along the rutile c-axis and unit-cell doubling (Figures 1.1b and 1.5), as in the Peierls mechanism [8,34-35] or from the opening of a correlation gap due to carrier localization, as in the Mott-Hubbard mechanism [9, 10, 36].

The Peierls mechanism refers to instability in the normal Fermi surface of a one dimensional metal, whereby an energy gap opens up at the Fermi surface due to periodic lattice deformations that change the periodicity of the crystal [4,37]. Figure 1.7 shows a generic band structure for a one-dimensional system, illustrating the effect of such a periodic deformation on the energy-wavevector $E(k)$ dispersion.

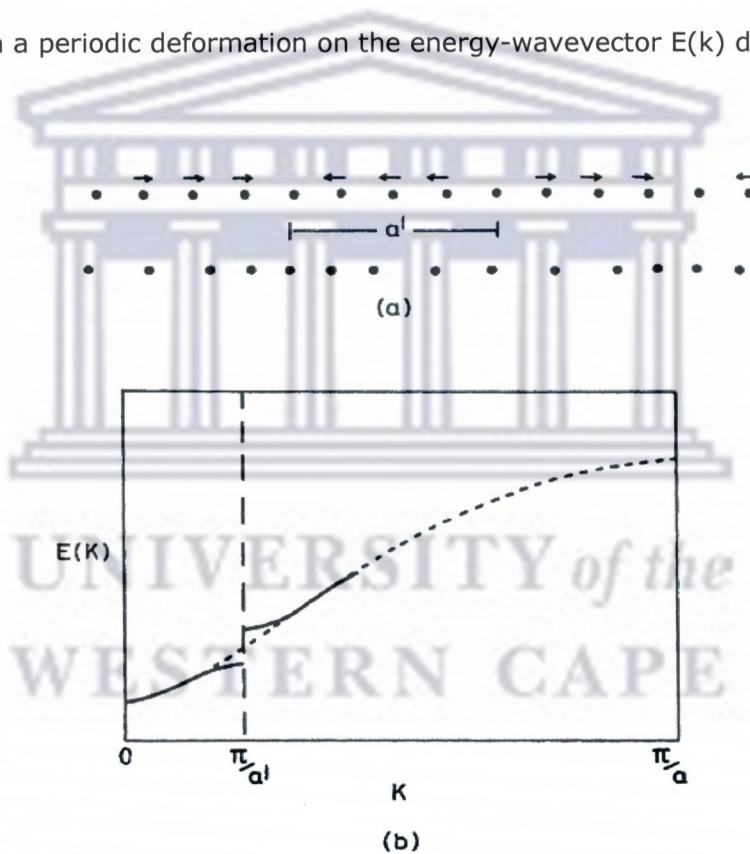


Figure 1.7: Sketch of Peierls mechanism. (a) Periodic lattice distortion of chain of atoms and (b) its effect on the band structure. New bandgaps appear in the energy-wavevector dispersion at $k = \frac{\pi}{a'}$, and at multiples of this value of k (not shown), where a' is the periodicity of the distortion [4].

New Brillouin-zone boundaries appear in response to the enlarged "superlattice" periodicity a' and lead to new energy gaps at values of k that are a multiple of $\frac{\pi}{a'}$. If the Fermi surface of the unperturbed crystal ends up at one of the new zone boundaries, the deformation-induced bandgap will destroy the metallic properties of the conduction electrons. Opening a bandgap at the Fermi level lowers the energy of electrons below the gap (Figure 1.7b), and thereby leads to some stabilization of occupied electron states. It turns out that in a one-dimensional system a Peierls perturbation of the electronic levels is always energetically favorable, so that an appropriate periodic deformation of the crystal lattice will always prevail over the opposing short-range elastic forces and destroy the metallic ground state [4].

The periodicity a' of the lattice deformation resulting from the Peierls instability is related to the Fermi-surface wavevector k_F by $a' = \frac{\pi}{k_F}$. Depending on the value of k_F , a' may or may not be commensurate with the original lattice spacing a . An example of particular relevance to VO_2 is that of a half-filled band in one dimension: $k_F = \frac{1}{2} \frac{\pi}{a}$, hence $a' = 2a$. Such periodic deformation can be described simply as "dimerization" of the original lattice, with electrons concentrating periodically in the "bonds" between the more closely spaced pairs of atoms, a situation referred to as a charge-density wave [4]. Considering the formation of metal-metal dimers, the doubling of the monoclinic unit cell, and the quasi- one-dimensional character of the $3d_{//}$ (formed by d orbitals oriented for overlap along the rutile c -axis), it seems only natural to attribute the VO_2 phase transition to a Peierls-type instability of the Fermi surface. In the metallic phase, the $3d_{//}$ band would be half-full, and the predicted Peierls deformation would indeed lead to an alternation of V-V distances, yielding a lower band filled by two electrons per vanadium pair. Support for the Peierls-like influence of the lattice degrees of freedom on the VO_2 transition was furnished by electronic structure calculations [34,20] based

on density functional theory within the local density approximation. Wentzcovitch et al. [34-35] used a variable cell-shape approach to allow for simultaneous relaxation of the atomic positions and the primitive translations. As a result, starting from different intermediate structures, these authors obtained the monoclinic M_1 structure as the most stable one. The calculated lattice parameters for both cells were in good agreement with the experimental data. However, the calculations failed to yield the opening of the M_1 -phase bandgap: the top of the bonding $3d_{//}$ band was found to overlap slightly (0.04 eV) with the bottom of the $3d_{\pi}$ band (only for a hypothetical structure with larger dimerizations would the band gap open). This result was attributed to the typical failure of the local density approximation to correctly reproduce measured optical bandgaps. Eyert et al. [20] also found semi-metallic behavior, with a band overlap of 0.1 eV rather than the observed optical bandgap. Since both types of 3d bands were found to be coupled by charge conservation rather than hybridization, the author interpreted the M_1 phase as arising from a Peierls-like instability of the $3d_{//}$ bands in an embedding reservoir of $3d_{\pi}$ electrons.

A different mechanism for the VO_2 phase transition was proposed by Zylbersztein and Mott [9], one based on the presence of strong electron-electron correlations in the $3d_{//}$ band, with the electron-lattice interaction playing an auxiliary role. In the metallic phase, the correlations appear to be efficiently screened by the $3d_{\pi}$ bands, but in the semiconducting phase the effect of screening on the $3d_{//}$ electrons is diminished, since the $3d_{\pi}$ bands experience an upshift in energy due to the zigzag displacement of the V atoms. As a consequence, the narrow $3d_{//}$ bands at the Fermi energy are susceptible to strong Coulomb correlations and undergo a Mott transition (see below), which opens the optical bandgap. In this scheme, the crystalline distortion (tilting of V atoms) serves to lift the band degeneracy, so that the correlation energy becomes comparable with the bandwidth, while the dimerization (V-V pairing) has only a minor effect on the bandgap [9].

Returning to the specific case of VO₂, Paquet and Leroux-Hugon [10] pointed out some deficiencies in the description of the transition in terms of the Mott-Hubbard model alone. One of these arises from the lattice distortion (zigzag tilting of vanadium atoms), which is required to lift the 3d_{||}-3d_⊥ degeneracy and also implies, by symmetry arguments, V-V pairing whereas a Mott-Hubbard mechanism generally cannot break any crystallographic symmetry. In addition, the vanishing magnetic susceptibility in the M₁ phase suggests some spin dimerization mechanism that also originates in V-V pairing, such as the magnetic analog of the Peierls instability known as a "spin-Peierls" transition [38]. Paquet and Leroux-Hugon thus concluded that any theory attempting to account for the major features of the transition, namely, symmetry breaking, gap opening, and magnetic properties, and to give a quantitative thermodynamical analysis must incorporate both (Peierls and Mott-Hubbard) mechanisms on an equal footing [10]. Starting from experimentally derived parameters and a tight-binding representation for the 3d_{||} and 3d_⊥ bands, but also including Mott-Hubbard-type interactions for both bands as well as a phonon contribution, the authors calculated that the VO₂ transition is primarily driven by electron-electron correlations, with the onset of lattice distortion being only a consequence of this primary mechanism though playing a crucial role in determining the first-order nature of the transition [10].

1.1.4. VO₂: latest findings in Metal-insulator transition

Outlined here in chronological order are some very recent theoretical and experimental advances regarding the nature of VO₂ and its phase transition:

- **Cavalleri et al.** [39] (2004): Evidence for a Structurally-Driven Insulator-to-Metal-Transition in VO₂: A view from the Ultrafast Timescale. The authors measured the transition time for changes in the reflectivity and transmission of thin film VO₂, using ultrafast pump-probe spectroscopy in the range 15 fs-1.5 ps; measured continuous-wave Raman spectra.

- **Biermann et al.** [40] (2005): Dynamical Singlets and Correlation-Assisted Peierls Transition in VO₂. They calculated the electronic structures of metallic (R phase) and semiconducting (M1 phase) VO₂, using: (i) a cluster extension of dynamical mean-field theory (C-DMFT) in combination with (ii) density functional theory within the local density approximation (DFT-LDA).
- **Haverkort et al.** [41] (2005): Orbital-Assisted Metal-Insulator Transition in VO₂. They measured and simulated polarization-dependent X-ray absorption spectra (XAS) in both phases of single-crystal VO₂ at the V L_{2,3} edges (2p → 3d, hν ≈ 510-530 eV) and observed "dramatic switching" of orbital occupation across the transition from almost isotropic in the metallic R phase to almost completely 3d_π-polarized in the insulating M₁ phase- "indicating the crucial role of the orbitals and lattice in the correlated motion of the electrons". The authors concluded that the VO₂ phase transition is an "orbital-assisted 'collaborative' Mott-Peierls transition".
- **Kübler et al.** [5] (2007): Coherent Structural Dynamics and Electronic Correlations during an Ultrafast Insulator-to-Metal Phase Transition in VO₂
- **Qazilbash et al.** [6] (2007): Mott Transition in VO₂ Revealed by Infrared Spectroscopy and Nano-Imaging. They authors measured the electromagnetic response of a VO₂ film on a spatial scale of 20 nm, using scattering scanning near field infrared microscopy (s-SNIM) in conjunction with far field infrared spectroscopy, imaged the appearance and temperature evolution of "nanoscale metallic puddles" in a narrow temperature range at the onset of the insulator-to-metal transition (Figure 1.8); obtained the spectral and temperature response of the optical conductivity, scattering rate, and optical effective mass of the nanoscale puddles, from a combination of near-field scattering amplitudes and far-field spectra within an effective medium theory (EMT). They also revealed that the nanoscale metallic puddles have different characteristics

from the rutile (R) metallic phase of VO_2 , namely: (i) optical pseudo-gap in the electronic density of states, likely resulting from "a complex interplay between electronic correlations and charge ordering"; (ii) enhancement of the low-frequency effective optical mass at $T = 342$ K compared to the R-phase value (e.g., at $T = 360$ K); (iii) crucially, divergent temperature-dependence of the low-frequency effective optical mass in the vicinity of the insulator-to-metal transition, arising from electronic correlations due to many-body Coulomb interactions- "an unambiguous attribute of the Mott transition".

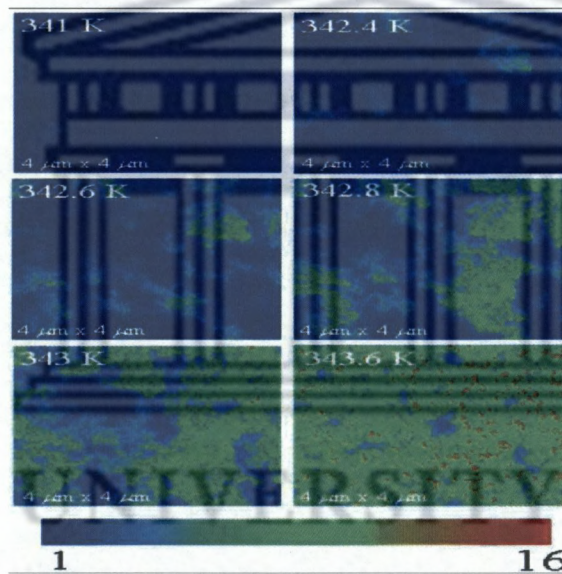


Figure 1.8: Images of near-field scattering amplitude over the same $4 \mu\text{m} \times 4 \mu\text{m}$ area obtained by s-SNOM operating at IR frequency $\omega = 930 \text{ cm}^{-1}$. The images are displayed for representative temperatures in the VO_2 insulator-to-metal transition regime, showing percolation in progress. The metallic "nanopuddles" (light blue, green, and red colors) give higher scattering near-field amplitude compared with the insulating phase (dark blue color) [6].

- **Jiang Wei et al.** [42] (2009) reported in his paper entitled "*New aspects of the metal-insulator transition in single-domain vanadium dioxide nanobeams*" the new aspects of the metal-insulator transition. They invented the nanobeam devices which can avoid all the problems related to the nature of the metal-insulator phase transition of VO₂ such as the irreproducibility between samples (properties such as resistivity are very sensitive to the arrangement of domains), broadening and hysteresis of the characteristics, and non-uniform stresses producing mechanical degradation [19]. Below 68 °C vanadium dioxide is an insulator. Above that temperature it's a metal. The nature of the transition has long remained elusive, though, because bulk VO₂ has a domain structure that complicates its behavior. Jian Wei and colleagues from the University of Washington have found an elegant way to avoid that difficulty and map the effective phase diagram. The team grew rectangular nanobeams that were thinner than the characteristic domain size of a few microns. They then suspended each beam between two electrical contacts. The metallic and insulating phases differ in lattice constant, but the constrained geometry creates a uniform stress field in a VO₂ beam such that the two phases coexist in a range of temperatures between 68 °C and 105 °C. Thanks to the dramatic change in optical properties that accompanies the transition, they could visually track the nucleation and growth of the metallic phase as a function of temperature. By measuring the electrical resistance in the coexistence regime, they found that the resistivity of the insulating phase is independent of temperature. That remarkable result, they argue, implies that the phase transition occurs at a fixed carrier density in the material and is consistent with a picture in which electron–electron interactions drive the transition.

1.2. VO₂: Phase transition characteristics

The semiconductor-metal transition (SMT) of VO₂ is characterized by four main parameters: transition temperature, abruptness or sharpness, hysteresis width and amplitude of the SMT; these parameters can be evaluated quantitatively from the resistivity or transmittance variation curves. The SMT characteristics vary strongly according to the synthesis conditions of single crystals and thin films. It was reported that the VO₂ single crystals have stronger abruptness of electrical resistance and optical transmittance, narrower hysteresis width of 1-2 °C [22,43], while thin films tend to have smaller abruptness and wider hysteresis width of 10-15 °C [24]. The variations in the VO₂ switching properties can be affected by the deposition parameters such as substrate temperature, thickness, oxygen partial pressure, substrate biased, ion bombardment, internal or external stress which can induce the mismatch between lattice constants [27,44-49]. The effect of hydrostatic pressure on the transition temperatures (T_c) of VO₂ has been examined and it was found that the T_c increases linearly with pressure at a rate of 0.082 K / bar [19]. The effect of various dopants has been investigated extensively in the literature. T_c is lowered by addition of dopants such as W, Ti, F, Mo, Nb, Cr, Li and Ta [50-54]. However, the doping of VO₂ is always followed by some alteration of the switching characteristics. Lowering T_c of VO₂ without altering its semiconductor-metal transition characteristics remains a challenge.

1.3. VO₂ thin films: common deposition techniques

The fabrication of better quality VO₂ thin films by novel methods is still an active area of research. Numerous fabrication techniques have been used successfully to produce high stoichiometric VO₂ thin films. Stoichiometric VO₂ depositions have been done using techniques as varied as reactive evaporation, metal-organic chemical vapor deposition (MOCVD), Sol-gel method, ion implantation, pulsed laser deposition (PLD) and several sputtering methods [55-63]. In this thesis, we will concentrate on the sputtering techniques most commonly used nowadays for the fabrication of VO₂ thin

films. Sputtering in various forms is one of the most common physical vapor deposition processes [64] for growing VO₂ thin films. VO₂ thin films were first grown by reactive sputtering in 1967 by Fuhs, Hensler and Ross of the Bell Telephone Laboratories [65], who made the films by reactive ion-beam sputtering of vanadium target in an argon-oxygen atmosphere. The three most common methods used to facilitate the deposition process include DC, RF, and magnetron sputtering. The comparative advantages of the sputtering process include film uniformity, scalability to larger substrates and efficiency of deposition. Following the first experiments in VO₂ deposition by reactive sputtering, and further analysis in those samples by Rozgonyi and Hensler both RF and DC reactive sputtering were studied by Duchene et al. [67]. Films with similar qualities were obtained in both cases, but since RF sputtering was more suitable for depositing high quality of VO₂ and had many advantages over DC sputtering.

1.4. Deposition Method chosen

Among the plethora of sputtering methods, we developed a novel physical vapor deposition; an uncommon sputtering named RF reactive inverted cylindrical magnetron sputtering (hollow cathode magnetron sputtering) for the synthesis of high quality of VO₂ thin films [68]. This coating technology offers advantages over others physical vapor deposition such as laser ablation and classical sputtering. It is a low-cost technique and has significant potentiality to coat wires, ribbons as well as all sides of three dimensional complex substrates. The complete description of this novel technique will be given in chapter 3.

1.5. References

- [1] F.J. Morin, Phys. Rev. Lett. 3, 34 (1959).
- [2] R. W. G. Wyckoff, Crystal structures, New York: Wiley (1965).
- [3] M. Imada, A. Fujimori, and Y. Tokura, Reviews of Modern Physics 70, 1039 (1998).
- [4] P. A. Cox, Transition metal oxides: An introduction to their electronic structure and properties, The International Series of Monographs on Chemistry, Clarendon Press; Oxford University Press, Oxford New York, (1992).
- [5] C. Kübler, H. Ehrke, R. Huber, R. Lopez, A. Halabica, R. F. Haglund, and A. Leitenstorfer, Phys.Rev. Lett. 99, 116401 (2007).
- [6] M. M. Qazilbash, M. Brehm, B. G. Chae, P. C. Ho, G. O. Andreev, B. J. Kim, S. J. Yun, A. V. Balatsky, M. B. Maple, F. Keilmann, H. T. Kim, and D. N. Basov, Science 318, 1750 (2007).
- [7] P. Baum, D. S. Yang, and A. H. Zewail, Science 318, 788 (2007).
- [8] J. B. Goodenough, J. Solid State Chem. 3, 490 (1971).
- [9] A. Zylbersztein and N. F. Mott, Physical Review B 11, 4383 (1975).
- [10] D. Paquet and P. L. Hugon, Physical Review B 22, 5284 (1980).
- [11] R. M. Wentzcovitch, W. W. Schulz, and P. B. Allen, Phys. Rev. Lett. 73, 3043 (1994).
- [12] T. M. Rice, H. Launois, and J. P. Pouget, Phys. Rev. Lett. 73, 3042 (1994).
- [13] R. M. Wentzcovitch, W. W. Schulz, and P. B. Allen, Phys. Rev. Lett. 72,3389 (1994).
- [14] S. Biermann, A. Poteryaev, A. I. Lichtenstein, and A. Georges, Phys. Rev. Lett. 94, 026404 (2005).
- [15] A. Cavalleri, T. Dekorsy, H. H. W. Chong, J. C. Kieffer, and R. W. Schoenlein, Phys. Rev. B 70, 161102 (2004).

- [16] H. T. Kim, Y. W. Lee, B. J. Kim, B. G. Chae, S. J. Yun, K. Y. Kang, K. J. Han, K. J. Yee, and Y. S. Lim, *Phys. Rev. Lett.* 97, 266401 (2006).
- [17] G. Kotliar and D. Vollhardt, *Phys. Today* 57, 53 (2004).
- [18] D. Adler, *Rev. Mod. Phys.* 40, 714 (1968).
- [19] C.N. Berglund and H.J. Guggenheim, *Phys. Rev.* 1, 1022 (1969).
- [20] V. Eyert, *Ann. Phys. Lpz* 11, 650 (2002).
- [21] A.S. Barker, H.W. Verleur and H.J. Guggenheim, *Phys. Rev. Lett.* 17,1286 (1966).
- [22] J.F. DeNatale, P.J. Hood and A.B. Harker, *J. Appl. Phys.* 66, 5844 (1989).
- [23] H.W. Verleur, A.S. Barker and C.N. Berglund, *Phys. Rev.* 172, 788 (1968).
- [24] D. Brassard, S. Fourmaux, M. Jean-Jacques, J. C. Kieffer, and M. A. El Khakani, *Appl. Phys. Lett.* 87, 051910 (2005).
- [25] R. Lopez, L. A. Boatner, T. E. Haynes, R. F. Haglund, and L. C. Feldman, *Appl. Phys. Lett.* 79, 3161 (2001).
- [26] G. Nihoul, C. Leroux, V. Madigou, and J. Durak, *Solid State Ionics* 117, 105 (1999).
- [27] C.H. Griffith and H.K. Eastwood, *J. Appl. Phys.* 45, 2201 (1974).
- [28] A. Cavalleri, M. Rini, and R. W. Schoenlein, *Jpn. J. Phys. Soc.* 75, 011004 (2006).
- [29] S. Shin, S. Suga, M. Taniguchi, M. Fujisawa, H. Kanzaki, A. Fujimori, H. Daimon, Y. Ueda, K. Kosuge, and S. Kachi, *Phys. Rev. B* 41, 4993 (1990).
- [30] M.M. Qazilbash, A.A. Schafgans, K.S. Burch, S. J. Yun, B.G. Chae, B.J. Kim, H.T. Kim, and D.N. Basov, *Phys. Rev. B* 77, 115121 (2008).
- [31] S. Lysenko, V. Vikhnin, F. Fernandez, A. Rua, and H. Liu, *Phys. Rev.* B75, 075109 (2007).
- [32] A. Cavalleri, M. Rini, and R.W. Schoenlein, *J. Phys. Society of Japan* 75, 011004 (2006).

- [33] J.B. Goodenough, *Prog. Solid State Chem.* 5,145 (1975).
- [34] R. M. Wentzcovitch, W. W. Schulz, and P. B. Allen, *Phys. Rev. Lett.* 73, 3043 (1994).
- [35] R. M. Wentzcovitch, W. W. Schulz, and P. B. Allen, *Phys. Rev. Lett.* 72, 3389 (1994).
- [36] T.M. Rice, H. Launois, and J.P. Pouget, *Phys. Rev. Lett.* 73, 3042 (1994).
- [37] C. Kittel, *Introduction to solid state physics*, Wiley, New York, 7th edition, 1996.
- [38] A.I. Buzdin and L.N. Bulayevskii, *Uspekhi Fizicheskikh Nauk* 131, 495 (1980).
- [39] A. Cavalleri, T. Dekorsy, H. H. W. Chong, J. C. Kieffer, and R. W.Schoenlein, *Phys. Rev. B* 70, 161102 (2004).
- [40] S. Biermann, A. Poteryaev, A. I. Lichtenstein, and A. Georges, *Phys. Rev. Lett.* 94, 026404 (2005).
- [41] M. W. Haverkort, Z. Hu, A. Tanaka, W. Reichelt, S. V. Streltsov, M. A. Korotin, V. I. Anisimov, H. H. Hsieh, H. J. Lin, C. T. Chen, D. I. Khomskii, and L. H. Tjeng, *Phys. Rev. Lett.* 95, 196404 (2005).
- [42] J.Wei, Z.Wang, W.Chen and D.H.Cobden, *Nature Nanotech. Lett.*4, 420 (2009).
- [43] L.A. Ladd and W. Paul, *Solid State Commun.* 7, 425 (1969).
- [44] E.E. Chain *J. Vac. Sci. Technol. A* 4, 432 (1986).
- [45] G. Xu, P. Jin, M. Tazawa and K. Yoshimura *Appl. Surf. Sci.* 244, 449 (2005).
- [46] K. Nagashima, T. Yanagida, H. Tanaka and T. Kawai, *J. Appl. Phys.* 100, 063714 (2006).
- [47] H. Miyazaki and I. Yasui *J. Phys. D: Appl. Phys.* 39, 2220 (2006).
- [48] F.C. Case, *J. Vac. Sci. Technol. A* 2, 1509 (1984).
- [49] Y. Muraoka and Z. Hiroi, *Appl. Phys. Lett.* 80, 583 (2002).
- [50] C.B. Greenberg, *Thin Solid Films*, 251, 81 (1994).
- [51] C.G. Granqvist, *Crit. Rev. Solid State Mater. Sci.* 16, 291 (1990).

- [52] W. Burkhardt, T. Christmann, S. Franke, W. Kriegseis, D. Meister, B.K. Meyer, W. Niessner, D. Schalch and A. Scharmann, *Thin Solid Films* 402, 226 (2002).
- [53] M. Soltani, M. Chaker, E. Haddad, R.V. Kruzelecky and D. Nikanpour, *J. Vac. Sci. Technol. A* 22, 859 (2004).
- [54] H. Futaki and M. Aoki, *Jpn. J. Appl. Phys.* 8 1008 (1969).
- [55] T.D. Manning and I.P. Parkin, *J. Mater. Chem.* 14, 2554 (2004).
- [56] T.D. Manning, I.P. Parkin, C. Blackman and U. Qureshi, *J. Mater. Chem.* 15, 4560 (2005).
- [57] G. Guzman, F. Beteille, R. Morineau and J. Livage, *Mater. Res. Bull.* 29, 509 (1994).
- [58] D.P. Partlow, S.R. Gurkovitch, K.C. Radford and L.J. Denes, *J. Appl. Phys.* 70, 443 (1991).
- [59] F. Beteille, and J. Livage, *J. Sol-Gel Sci. Technol.* 13, 915 (1998).
- [60] D.H Kim and H.S. Kwok, *Appl. Phys. Lett.* 65, 3188 (1994).
- [61] M. Maaza, K. Bouziane, J. Maritz, D.S. McLachlan, R. Swanepoel, J.M. Frigerio and M. Every, *Opt. Mater.* 15, 41 (2000).
- [62] E.E. Chain, *J. Vac. Sci. Technol. A* 5, 1836 (1987).
- [63] K. Okimura and N. Kubo, *Thin Solid Films* 515 4992 (2007).
- [64] J.A. Thornton, *Thin Solid Films* 107, 3 (1983).
- [65] E.N. Fuhs, D.H. Hensler and A.R. Ross, *Appl. Phys. Lett.* 10, 199 (1967).
- [66] G.A. Rozgonyi, and D.H. Hensler *J. Vac. Sci. Technol.* 5, 194 (1968).
- [67] J. Duchene, M. Terrail and M. Pailly, *Thin Solid Films* 12, 231 (1972)
- [68] J.B. Kana Kana, J.M. Ndjaka, P. Owono Ateba, B.D. Ngom, N. Manyala, O. Nemraoui, A.C. Beye and M. Maaza, *Appl. Surf. Sci.* 254, 3959 (2008).

Chapter 2

PLASMON RESONANCES OF NANOGOLD OR NANOSILVER PARTICLES & REVIEW OF WORLDWIDE RESEARCH IN Ag (Au)-VO₂

Abstract

This chapter is dedicated to exploring the physics of plasmon resonances of noble metal nanoparticles such as Au or Ag, as well as to studying the effects of different factors governing plasmon resonance. The chapter closes with a review of worldwide research works done in Ag (Au)-VO₂.

2.1. Physics of plasmon resonance

The field of plasmonics lies at the forefront of current revolutionary developments in optics at nanoscale dimensions, with broad applications in the fields of biology, chemistry, and engineering. Advancing these applications will require an enhanced focus on the fundamental science of plasmonics in new and exotic regimes. Plasmonics forms a major part of the fascinating field of nanophotonics, which explores how electromagnetic fields can be confined over dimensions on the order of or smaller than the wavelength. It is based on interaction processes between electromagnetic radiation and conduction electrons at metallic interfaces or in a small metallic nanostructures, leading to an enhanced optical near field of sub-wavelength dimension. Plasmonics,

one of the promising areas of nanophotonics is defined as the manipulation of light at the nanoscale based on the properties of surface plasmons arising from free-electron response (negative permeability); while nanophotonics can be defined as “the science and engineering of light-matter interaction that take place on wavelength and sub wavelength scales where the physical, chemical or structural nature or artificial nanostructured matter controls the interactions [1]. Localized surface plasmons are non propagating excitations of the conduction electrons of metallic nanostructures coupled to the electromagnetic field. These modes arise naturally from the scattering problem of a small, sub-wavelength conductive nanoparticle in an oscillating electromagnetic field. The resonant electromagnetic behaviour of noble metal nanoparticles is due to the confinement of the conduction electrons to the small particle volume. For particles with a diameter $d \ll \lambda$, the conduction electrons inside the particle move all in phase upon plane wave excitation with radiation of wavelength λ , leading to the buildup of polarization charges on the particle surface. These charges act as an effective restoring force, allowing for a resonance to occur at a specific frequency; the particle plasmon resonance frequency where the response of the electrons shows a $\frac{\pi}{2}$ phase lag with respect of the driving field. Thus, a resonantly enhanced field builds up inside the particle, which in the small particle limit is homogenous throughout its volume, producing a dipolar field outside the particle [2]. (see figure 2.1 NPs in an oscillating field).

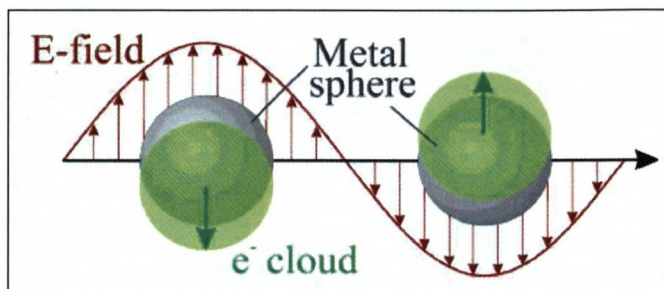


Figure 2.1: Schematic of the simplest mode of collective oscillation of the conduction electrons relative to the nuclei of a metal NP, the dipolar particle-plasmon [3].

Another consequence of the curved surface is that plasmon resonances can be excited by direct light illumination. This resonance is called the localized plasmon resonance. For gold and silver nanoparticles, the resonance falls into the visible region of the electromagnetic spectrum. Striking consequences of this are the bright colors exhibited by particles in transmitted and reflected light, due to resonantly enhanced absorption and scattering. This effect has found applications for many hundreds of years, for example in the staining of glass for windows or ornamental cups or ceramic pottery; (see figure 2.2). This Lycurgus Cup represents one of the outstanding achievements of the ancient glass industry. This late Roman cut glass vessel is extraordinary in several respects, firstly in the method of fabrication and the exceptional workmanship involved and secondly in terms of the unusual optical effects displayed by the glass.

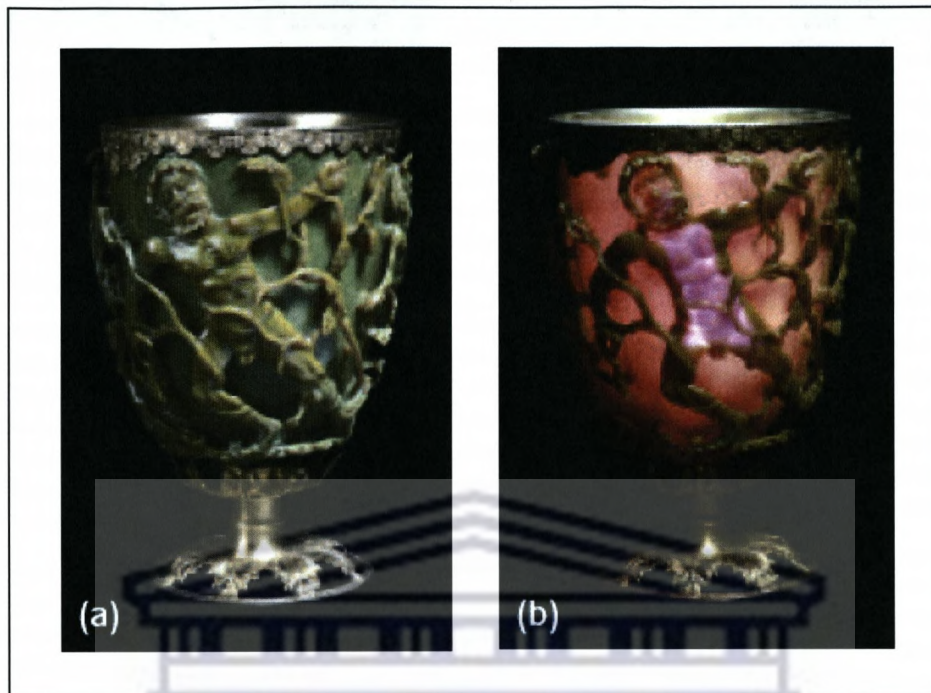


Figure 2.2: Lycurgus Glass cup Byzantine empire 4th century A.D. The glass cup, on display in the British Museum, shows a striking red color when viewed in transmitted light (b), while appearing green in reflection (a). This peculiar behaviour is due to small Au nanoparticles embedded in the glass [4].

2.1.1. Quasi-static approximation

The interaction of a particle of size d with the electromagnetic field can be analyzed using the simple quasi-static approximation provided that $d \ll \lambda$, i.e. the particle is much smaller than the wavelength of light in the surrounding medium. In this case, the phase of the harmonically oscillating electromagnetic field is practically constant over the particle volume, so that one can calculate the spatial field distribution by assuming the simplified problem of a particle in an electric field. The harmonic time dependence can then be added to the solution once the field distributions are known. As we will show below, this lowest-order approximation of the full scattering problem

describes the optical properties of nanoparticles of dimensions below 100 nm adequately for many purposes. Let start with the most convenient geometry for an analytical treatment: a homogeneous, isotropic sphere of a radius a located at the origin in a uniform, static electric field $\vec{E} = E_0 \vec{z}$ (Figure 2.3).

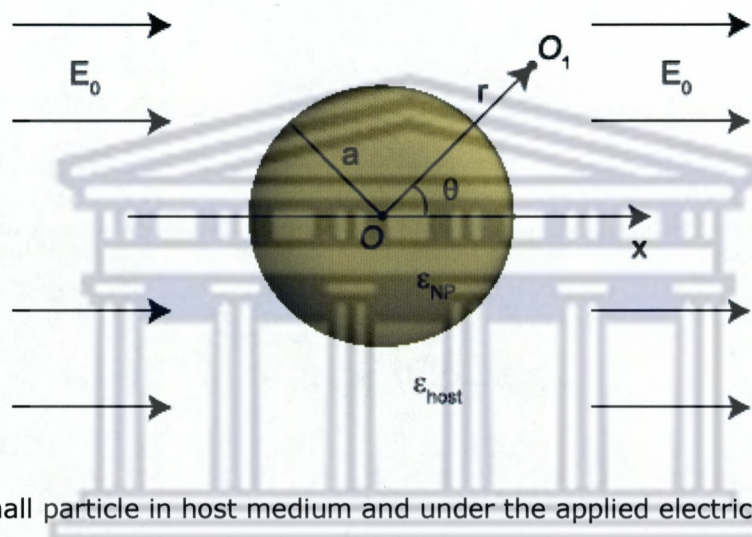


Figure 2.3: Small particle in host medium and under the applied electric field of x-polarized plane wave.

The surrounding medium is isotropic and non-absorbing with dielectric constant ϵ_{host} , and the field lines are parallel to the z-direction at sufficient distance from the sphere. The dielectric response of the sphere is further described by the dielectric function $\epsilon_{\text{NP}}(\omega)$, which we take for the moment as a simple complex number ϵ . In the electrostatic approach, we are interested in a solution of the Laplace's equation for the potential, $\nabla^2 \Phi = 0$, from which we will be able to calculate the electric field $E = -\nabla \Phi$. Due to the azimuthal symmetry of the problem, the general solution is of the form [5]

$$\Phi(r, \theta) = \sum_{l=0}^{\infty} [A_l r^l P^l + B_l r^{-(l+1)}] P_l(\cos \theta) \quad \text{Eq. 2.1}$$

where $P_l(\cos\theta)$ are the Legendre Polynomials of order l , and θ the angle between the position vector \mathbf{r} at point O_1 and the z -axis (Figure 2.3). Due to the requirement that the potentials remain finite at the origin, the solution for the potentials Φ_{in} inside and Φ_{out} outside the sphere can be written as

$$\Phi_{in}(r, \theta) = \sum_{l=0}^{\infty} A_l r^l P_l(\cos\theta) \quad \text{Eq. 2.2}$$

$$\Phi_{out}(r, \theta) = \sum_{l=0}^{\infty} [B_l r^l + C_l r^{-(l+1)}] P_l(\cos\theta) \quad \text{Eq. 2.3}$$

The coefficients A_l , B_l and C_l can now be determined from the boundary conditions at $r \rightarrow \infty$ and at the sphere surface $r = a$. The requirement that $\Phi_{out} \rightarrow -E_0 z = -E_0 r \cos\theta$ as $r \rightarrow \infty$ demands that $B_1 = -E_0$ and $B_l = 0$ for $l \neq 1$. The remaining coefficients A_l and C_l are defined by the boundary conditions at $r = a$. Equality of the tangential components of the electric field demands that:

$$-\frac{1}{a} \frac{\partial \Phi_{in}}{\partial \theta} \Big|_{r=a} = -\frac{1}{a} \frac{\partial \Phi_{out}}{\partial \theta} \Big|_{r=a} \quad \text{Eq. 2.4}$$

$$-\varepsilon_0 \varepsilon_{NP} \frac{\partial \Phi_{in}}{\partial \theta} \Big|_{r=a} = -\varepsilon_0 \varepsilon_{host} \frac{\partial \Phi_{out}}{\partial \theta} \Big|_{r=a} \quad \text{Eq. 2.5}$$

Application of these boundary conditions leads to $A_l = C_l = 0$ for $l \neq 1$, and via the calculation of the remaining coefficients A_1 and C_1 the potentials evaluate to [5]

$$\Phi_{in} = -\left(\frac{3\varepsilon_{host}}{\varepsilon_{NP} + 2\varepsilon_{host}}\right) E_0 r \cos\theta \quad \text{Eq. 2.6}$$

$$\Phi_{out} = -E_0 r \cos\theta + \frac{(\varepsilon_{NP} - \varepsilon_{host})}{(\varepsilon_{NP} + 2\varepsilon_{host})} E_0 a^3 \frac{\cos\theta}{r^2} \quad \text{Eq. 2.7}$$

Φ_{out} describes the superposition of the applied field and that of a dipole located at the particle center. We can rewrite Φ_{out} by introducing the dipole moment \vec{P} as

$$\Phi_{out} = -E_0 r \cos\theta + \frac{\vec{P} \cdot \vec{r}}{4\pi \varepsilon_0 \varepsilon_{host} r^3} \quad \text{Eq. 2.8}$$

$$\vec{P} = 4\pi \epsilon_0 \epsilon_{host} a^3 \frac{(\epsilon_{NP} - \epsilon_{host})}{(\epsilon_{NP} + 2\epsilon_{host})} \vec{E}_0 \quad \text{Eq. 2.9}$$

We therefore see that the applied field induces a dipole moment inside the sphere of magnitude proportional to $|\vec{E}_0|$. If we introduce the polarizability α , defined via,

$$\vec{P} = \epsilon_0 \epsilon_{host} \alpha \vec{E}_0 \quad \text{Eq. 2.10}$$

we arrive at:

$$\alpha = 4\pi a^3 \frac{(\epsilon_{NP}(\omega) - \epsilon_{host})}{(\epsilon_{NP}(\omega) + 2\epsilon_{host})} \quad \text{Eq. 2.11}$$

This equation represents the complex polarizability of a small sphere of sub-wavelength diameter in the electrostatic approximation. It is apparent that the polarizability experiences a resonant enhancement under the condition that $|\epsilon_{NP} + 2\epsilon_{host}|$ is minimum, which for the case of small or slowly-varying $\text{Im}[\epsilon_{NP}]$ around the resonance simplifies to

$$\text{Re}\left[\frac{\epsilon_{NP}(\omega_{res})}{\epsilon_{host}}\right] = -2 \quad \text{Eq. 2.12}$$

This relationship is called the Fröhlich condition and the associated mode (in an oscillating field) the dipole surface plasmon of the metal nanoparticle. For a sphere consisting of a Drude metal with a dielectric function located in air, the Fröhlich criterion is met at the frequency $\omega_0 = \frac{\omega_p}{\sqrt{3}}$. The Fröhlich condition expresses the strong dependence of the resonance frequency on the dielectric environment: The resonance red-shifts as ϵ_{host} is increased. Metal nanoparticles are ideal platforms for optical sensing of changes in refractive index. From the viewpoint of optics, it is much more interesting to note that another consequence of the resonantly enhanced polarization

α is a concomitant enhancement in the efficiency with which a metal nanoparticle scatters and absorbs light. The corresponding cross sections for scattering and absorption C_{sca} and C_{abs} can be calculated via the Pointing-vector [6]

$$C_{sca} = \frac{k^4}{6\pi} |\alpha|^2 = \frac{8\pi}{3} k^4 a^6 \left| \frac{(\epsilon_{NP} - \epsilon_{host})}{(\epsilon_{NP} + 2\epsilon_{host})} \right|^2 \quad \text{Eq. 2.13}$$

$$C_{abs} = k \text{Im}[\alpha] = 4\pi k a^3 \text{Im} \left[\frac{\epsilon_{NP} - \epsilon_{host}}{\epsilon_{NP} + 2\epsilon_{host}} \right] \quad \text{Eq. 2.14}$$

The equations above show that indeed for metal nanoparticles both absorption and scattering (and thus extinction) are resonantly enhanced at the dipole particle plasmon resonance, i.e. when the Fröhlich condition is met [7]. For a sphere of volume V and dielectric function $\epsilon = \epsilon_1 + i\epsilon_2$ in the quasi-static limit, the explicit expression for the extinction cross section $C_{ext} = C_{abs} + C_{sca}$

$$C_{ext} = 9 \frac{\omega}{c} \epsilon_{host}^{3/2} V \frac{\epsilon_2}{[\epsilon_1 + 2\epsilon_{host}]^2 + \epsilon_2^2} \quad \text{Eq. 2.15}$$

2.2. Mie theory

We have seen that the theory of scattering and absorption of radiation by a small sphere predicts a resonant field enhancement due to a resonance of the polarizability α if the Fröhlich condition is satisfied. Under these circumstances, the nanoparticle acts as an electric dipole, resonantly absorbing and scattering electromagnetic fields. This theory of the dipole particle plasmon resonance is strictly valid only for vanishingly small particles; however, in practice the calculations outlined above provide a reasonably good approximation for spherical particles with dimensions below 100 nm illuminated with visible or near-infrared radiation. However, for particles of larger dimensions, where the quasi-static approximation is not justified due to significant phase-changes of the driving field over the particle volume, a rigorous electrodynamic approach is required. In a seminal paper, Mie in 1908 developed a

complete theory of the scattering and absorption of electromagnetic radiation by a sphere, in order to understand the colors of colloid gold particles in solution [8]. The approach of what is now known as Mie theory is to expand the internal and scattered fields into a set of normal modes described by vector harmonics. The quasi-static results valid for sub-wavelength spheres are then recovered by a power series expansion of the absorption and scattering coefficients and retaining only the first term. For more information about Mie theory expansion read the book written by Kreibig and Vollmer [9].

2.3. Factors governing the plasmon resonance

Noble metal nanoparticles Ag or Au are well known for their strong interactions with visible light through the resonant excitations of the collective oscillations of the conduction electrons within particles. In general, the spectral position, damping, and strength of the plasmon resonances of a metal nanoparticle are known to be dependent on the particle material, size, shape, distance between interparticles, volume fraction and dielectric function of the surrounding host [10].

2.3.1. Size and temperature dependence of the plasmon resonance

A strong size dependence of the plasmon bandwidth proved experimentally by Kreibig et al. [11-12] showed that the position of the absorption maximum of colloidal gold nanoparticles ranging from 9 to 99 nm is affected although both a blue-shift and a red-shift occur with decreasing particle size. Furthermore, the temperature dependence of the plasmon absorption was examined. Only a small temperature effect of 22 nm gold particles is observed, which is consistent with the fact that the dephasing of the surface plasmon electron motion is a result of electron-electron repulsion rather than electron-phonon interaction. No temperature dependence of the plasmon bandwidth was found for the other sizes.

2.3.2. Shape effects in plasmon resonance

The shape and size of a metallic nanoparticle dictate the spectral signature of its plasmon resonance, the ability to change these two parameters and study the effect on the localized surface plasmon resonance is an important experimental challenge. The shape effects on the optical properties of silver colloids observed by Jin et al. and Mock et al. [13-14] showed that the spectral plasmon resonance peak of triangular silver NPs is centred at 625 nm, while those of triangle corners rounded and further rounded are centred at 585 nm and 555 nm respectively. Furthermore, Jin et al. reported intentionally inducing shape transformation on a colloidal suspension of silver nanospheres to nanoprisms, and observed a spectral shift from blue to red. In conclusion, the plasmon resonance of noble metal NPs is strongly affected by the shape of the NPs.

2.3.3. Interparticle coupling resonance effects on the plasmon resonances

The interparticle coupling resonance between pairs of elliptical metal particles by simulations and experiments was investigated by Su et al. and Prashant et al. [15-16]. In their work, the authors demonstrated that the resonant wavelength peak of two interacting particles is red-shifted from that of a single particle because of near-field coupling. They also reported that, the shift decays approximately exponentially with increasing particle spacing and become negligible when the gap between the two particles exceeds about 2.5 times the particle short-axis length.

2.3.4. Local refractive index dependence of plasmon resonance

The plasmon resonance is very sensitive to changes in the local dielectric environment [17,3]. Typically researcher's sense changes in the local environment through a localized surface plasmon resonance wavelength-shift measurement, dark field microscope [18] although a variant of angle resolved sensing for the LSPR is also possible [19]. The peak position of plasmon resonance was found affected by slight changes in the local index. The active modulation of the plasmon resonance wavelength of noble metal nanoparticles remains a challenge by considering one host

matrix and changing its refractive index by applying external temperature stimuli as developed by Maaza et al. [20] or by applying external electric field as developed by Hsieh et al. [21].

2.4. Applications of plasmonics

One of the most promising applications of the plasmonics is optical sensing. However, gold has emerged as the metal of choice for almost all practical optical sensing applications, including those based on surface plasmons. An important consequence is due to the permittivity of gold, sensing is usually limited to the visible and near-infrared part of the spectrum [22]. Another spectacular application of plasmonics to date is surface enhanced Raman scattering (SERS), which exploits the generation of highly localized light fields in the near-field of metallic nanostructures for enhancing spontaneous Raman scattering of suitable molecules. Using chemically roughened silver surfaces, Raman scattering events of single molecules has been recorded [23-24] with estimated enhancements of the scattering cross section by factors up to 10^{14} . The majority of this enhancement is believed to arise from the highly enhanced fields in metal nanoparticle junctions due to localized surface plasmon resonances. Label-free plasmonic biosensors using plasmonic nanorod metamaterials is the most recent application of plasmonics in biology today hence it can detect some molecular binding events [25]. Creating a versatile set of highly stable fluorophores capable of high emission rate is crucial to studies of the individual function of biomolecules. Plasmonic controlled single molecule fluorescence near defined metallic nanostructures was proposed by Fu et al. [26] in order to enhance fluorescence intensity, reduce blinking and increase photostability. Recently, Peng et al. [27] provided a novel platform for testing concepts of plasmonics in label-free DNA detection on nanostructured Ag surfaces. Plasmonics using gold nanoparticles was revealed to be a great promise for photothermal therapy for cancer treatment [28].

2.5 Review of worldwide research in Ag (Au)-VO₂

Outlined here in chronological order are some very recent numerical simulation and experimental advances regarding the fabrication of Ag-VO₂ or Au-VO₂ by different techniques and its plasmonic properties:

- **Cavanna et al.** [29] (1999), have successfully prepared pure Au and Au_xVO₂ thin films from vanadium alkoxide precursors via the sol-gel spin-coating process. They proved that, for the optical switching behaviour of the Au_xVO₂ thin films showing in the composition range $0 \leq x \leq 0.0125$, a small quantity of Au (0.25 atom %) leads to an important decrease in the transition temperature. In addition, they proposed Au_xVO₂ as a potential candidate of optical power limiting applications against laser aggression, since gold metallic particles are good heat absorbers. In their work, no plasmonic properties were investigated.
- **Maaza et al.** [30] (2005) synthesized the films of Au-VO₂ by pulsed laser ablation. A XeCl pulsed excimer laser was used to ablate a circular pressed black powder of pure VO₂ incorporated with a triangular slice of high purity gold. They reported for the first time to the best of their knowledge, a reversible tunability of the surface plasmon resonance of Au-VO₂ nanophotonics induced by the external temperature stimuli.
- **Suh et al.** [31] (2006) fabricated a periodic array of sub-wavelength apertures in Ag-VO₂ and Au-VO₂ double layer films by pulsed laser ablation and thermal evaporator. They demonstrated the modulation of the transmission of near-infrared light through the resulting fabricated films. They proposed Vanadium-dioxide-gold (VO₂-Au) composite material as a practical candidate for enabling the modulation of plasmonic behavior, as shown in the case of extraordinary optical transmission through sub-wavelength hole arrays.
- **Xu et al.** [32] (2006) investigated the surface plasmon resonance of Ag nanoparticles on VO₂. Silver nanoparticles were prepared on top of VO₂ film by the radiofrequency (rf) magnetron sputter method. They also showed that, the

peak extinction wavelength reversibly shifts with temperature and proved that, this shift is Ag mass thickness dependent.

- **Cortie et al.**[33] (2007) examined using a computational method, how the optical properties of various forms of composite nanoparticles of Au and VO₂ would be affected by the phase transition in VO₂ and pointed out that an important current issue in plasmonics is the possibility of a "self-regulating" localized surface plasmon resonance (LSPR) of composite metallic NPs; for instance, under a sufficiently intense light irradiation, the dynamic functionality of such NPs could be used as a probe in photothermal therapy or optical sensing applications [34-35].
- **Suh et al.** [36] (2008), systematically explored the modulation of the LSPR in lithographically fabricated arrays of Au NPs by means of the reversible metal-semiconductor transition of VO₂. In particular, they demonstrated the dependence of this modulation on nanoparticle size, shape, and light polarization. The Au LSPR peaks blue-shift in the metallic state of VO₂ ($T > T_c$) with respect to the semiconducting state ($T < T_c$) by as much as 80 nm for symmetric and 200 nm for asymmetric Au NPs (including polarization effects for the latter). For the asymmetric Au NPs, they observed a strong dependence of the plasmon resonance on polarization of the incident light with respect to the major (long) and minor (short) NP axes, complemented by subtler peak shifts with varying aspect ratios at a fixed polarization.
- **Binions et al.** [37] (2008) reported for the first time a hybrid method named hybrid aerosol-assisted (AA) and atmospheric pressure (AP) CVD to produce a thin film of gold nanoparticles doped vanadium dioxide. The subsequent technique showed great promise as the film characteristics were similar to those produce by APCVD.

- **Xu et al.** [38] (2008) again, in their work titled: "electron injection assisted phase transition in a nano- Au-VO₂ junction" revealed that Au nanoparticles have a marked effect on the reduction in the phase transition temperature of VO₂. They believed that a process of electron injection in which electrons flow from Au to VO₂ due to the lower work function of the metal is the responsible mechanism for the lowering of T_c.
- **Xu et al.** [39] (2009) recently, investigated the tunable optical properties of nano-Au on VO₂ and showed the strong dependence of the plasmon resonance wavelength on Au mass thickness as well as the red-shift of the plasmon resonance wavelength as Au thickness increases.
- **In the present work** (2009), (chapter 8) [40], a novel deposition method named inverted cylindrical magnetron sputtering also known as hollow cathode sputtering was revealed as promising vacuum technology for the preparation of high-quality VO₂ and Au-VO₂ thin films. We compared the plasmonic properties of our films with those already reported in the literature. As it is well known that the fabrication of the thin films by novel methods is still an active and open area of research, the use of ICMS for the growth of VO₂ and Au-VO₂ composite thin films adds knowledge to the subject and ranks this technique among the existing one well-known in the literature.

2.6 References

- [1] <http://www.phoremot.org/about.cfm>
- [2] S.A. Maier and HA Atwater, J. Appl. Phys. 98, (2005) 011101 .
- [3] K.L. Kelly, E. Coronado, L. Zhao, G.C. Schatz, J. Phys. Chem. B 107,(2003) 668.
- [4] <http://www.britishmuseum.org>.
- [5] J. Jackson and D. John, Classical electrodynamics. John Wiley & Sons, Inc., New York, NY, 3rd edition (1999).
- [6] C.F. Bohren and D.R. Huffman, Absorption and scattering of light by small particles. John Wiley & Sons, Inc., New York, NY 1st edition (1998).
- [7] U. Kreibig and M. Vollmer, Optical Properties of Metal Clusters, Springer Series in Materials Science (1995).
- [8] Mie 1908.
- [9] A. L. González, J. A. Reyes-Esqueda, and C. Noguez, J. Phys. Chem.C 112 (19), (2008) 7356.
- [10] U. Kriebig and M. Vollmer, optical properties of metal clusters, Springer, Berlin, (1988).
- [11] U. Kriebig, U. Genzel, Surf. Sci., 156, (1985) 678.
- [12] S.Link and M. A. El-Sayed, J. Phys. Chem. B 103, (1999) 4212.
- [13] R. Jin, YW Cao, C.A. Mirkin, K.L. Kelly, G.C. Schatz and J.G. Zheng, Science 294, (2001) 1901.
- [14] J.J. Mock, M. Barbic, DR Smith, DA Schultz and S Schultz, J. Chem. Phys., 116, (2002) 6755.
- [15] K.H. Su, Q.H. Wei, X. Zhang, J.J. Mock, D.R. Smith and S. Schultz, Nanolett. 3, (2003)1087.
- [16] K.J. Prashant and M.A. El-Sayed, Nanolett. 8, (2008) 4347.

- [17] M.M. Miller, A.A. Lazarides *J. Phys. Chem. B* 109, (2005) 21556.
- [18] J.J. Mock, D.R. Smith, and S. Schultz, *Nanolett.* 3, (2003) 485.
- [19] K. Hamamoto, R. Micheletto, R. Oyama, R.R.Umar, S.Kawai, Y.Kawakami, J. Opt. A: Pure Appl. Opt. 8, (2006) 268.
- [20] M. Maaza, O. Nemraoui, C. Sella, A.C. Beye, *Gold Bull.* 38, (2005)100.
- [21] K.C. Hsieh, HL Chen, D.H. Wan and J. Shieh, *J. Phys. Chem. C* 112, (2008) 11673.
- [22] S.A. Maier, *Plasmonics fundamentals and applications*, Springer (2007).
- [23] K. Kneipp, Y. Wang, H. Kneipp, L.T. Perelman, I. Itzkan, R.R. Dasari, and M.S. Feld, *Phys. Rev. Lett.* 78 (9), (1997) 1667.
- [24] S.M. Nie, and S.R. Emery, *Science* 275, (1997)5303.
- [25] A.V. Kabashin, P. Evans, S. Pstkovsky, W. Hendren, G.A. Wurtz, R. Atkinson, R. Pollard, V.A. Podolski and A.V. Zayats, *Nature Materials. Lett.* 8, (2009)867.
- [26] Y. Fu. J. Zhang and J.R. Lakowicz, *Journal of Fluorescence* 17, (2007)811.
- [27] H. Peng, M. Strohsahl, K.E. Leach, T.D. Krauss and B.L. Miller, *ACS NANO* 3, (2009) 2265.
- [28] P.C. Chen, S.C. Mwakwari and A.K. Oyelere, *Nanotechnology, Science and Applications* 1, (2008)45.
- [29] E. Cavanna, J.P. Segaud, and J. Livage, *Mater. Res. Bull.* 34, (1999)167.
- [30] M. Maaza, O. Nemraoui, C. Sella, A.C. Beye, B. Baruch-Barack, *Opt. Commun.* 254, (2005)188.
- [31] J.Y. Suh, E.U. Donev, R. Lopez, L.C. Feldman and R.F. Haglund Jr., *Appl. Phys. Lett.* 88, (2006)133115.
- [32] G. Xu, Y. Chon, M. Tazawa and P. Jin, *J. Phys. Chem. B* 110, (2006) 2051.
- [33] M.B. Cortie, A. Dowd, N. Harris and M.J. Ford, *Phys. Rev B* 75, (2007)113405.

- [34] J.M. Brockman, B.P. Nelson, and R.M. Corn, *Ann. Rev. Phys. Chem.* 51, (2000)41.
- [35] L.R. Hirsch, R.J. Stafford, J.A. Bankson, S.R. Sershen, B. Rivera, R.E. Price, J.D. Hazle, N.J. Halas, and J.L. West, *Proceedings of the National Academy of Sciences of the United States of America* 100, (2003) 13549.
- [36] J.Y. Suh, E.U. Donev, D.W. Ferrara, K.A. Tetz, L.C. Feldman and R.F. Haglund Jr, *J. Opt. A: Pure Appl. Opt.* 10, (2008)055202.
- [37] R. Binions, C. Piccirillo, R.G. Palgrave and I.P. Parkin, *Chem Vap. Deposition* 14, (2008) 33.
- [38] G. Xu, C.M. Huang, M. Tazawa, P. Jin, D.M. Chen and L. Miao, *Appl. Phys. Lett.* 93, (2008) 061911.
- [39] G. Xu, C.M. Huang, M. Tazawa, P. Jin and L.H. Chen, *Opt. Com.* 282, (2009) 896.
- [40] J.B. Kana Kana, J.M. Ndjaka, B.D. Ngom, N. Manyala, O. Nemraoui, A.Y. Fasasi, R. Nmutudi, A.Gibaud, D. Knoesen, M. Maaza, *Thin Solid Films* 518, (2010)1641.



UNIVERSITY *of the*
WESTERN CAPE

Chapter 3

EXPERIMENTAL TOOLS AND TECHNIQUES

Abstract

This chapter is dedicated to giving a brief overview of the sputtering process and general description of the inverted cylindrical magnetron sputtering used to fabricate the VO₂ and Au-VO₂ thin films, as well as to explaining the different techniques employed throughout the different stages of this work in order to characterize the surface and optical properties of the films.

3.1 Sputtering

3.1.1 Introduction

Sputtering provides a very useful method for preparing a wide range of thin films with the good control over film properties. It is widely used in industry from microelectronics to decorative coating of automobiles. When a solid surface is bombarded with energetic particles such as accelerated ions, surface atoms of the solid are partly scattered backward due to collisions between the surface atoms and the energetic particles. This phenomenon is called sputtering, which is widely used for thin film deposition, surface cleaning and etching, etc. The basic sputter deposition system is composed of a pair of electrodes. One of the electrodes is the cold cathode and the other is anode. The front surface of the cathode is covered with the target material to be sputtered. The substrate is placed on the anode. The sputter chamber is filled with

the sputter gas, typically Argon. The glow discharge is maintained under the application of the voltage between the electrodes. The Ar^+ ions generated in the glow discharge are accelerated towards the cathode (target). The bombardment of the target by these energetic positive ions causes the removal of target atoms. These target atoms deposit on the substrate so the thin film is formed. In this process, no chemical reaction happens between the gas and the target atoms. However, if at least one reactive gas (e.g. Oxygen or Nitrogen) is added in the chamber besides Ar, the reactive gas will react with target atoms forming a compound layer on the substrate. This technique is known as reactive sputtering. If the applied potential between the cathode and anode is constant with time, the process is called DC sputtering, by which the highly electrically conductive materials like metallic targets can be sputtered. For the insulating targets, however, the glow discharge in this DC sputtering system, can not be sustained because of the surface of target will charge up so that the fluxes of positive ions and electrons to the surface become equal, regardless of the potential applied to the electrode backing the insulating target, and then these ions and electrons recombine on the surface. In this case, a radio frequency (RF) voltage is applied to the target, which avoids the charge build up on the targets. This is called RF sputtering.

3.1.2 Principles

A sputtering system consists of an evacuated chamber, a target (cathode) and a substrate table (anode). The electric field inside a sputtering chamber accelerates electrons which collide with Ar atoms producing Ar^+ ions and more electrons and a characteristic purple/blue plasma. (See figure 3.1 Color of plasma of ICMS during the deposition of VO_2). The sputtering of the material requires the plasma. The features of plasmas are extremely complex and it is composed of numerous chemical species. They are constituted by an ionized gas under the influence of an electric field. The system that is out of thermodynamic equilibrium can be considered as the fourth state

of matter. It is composed of neutral particles, electrons, ions, free radicals and photons.

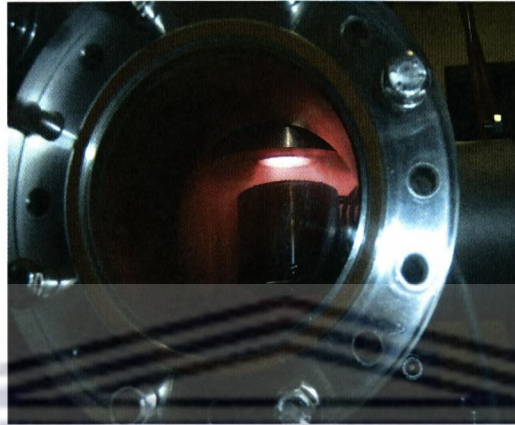


Figure 3.1: Plasma color during the deposition of VO_2 by Inverted cylindrical magnetron sputtering located at Materials Research Department-iThemba LABS.

These charged particles are then accelerated by the electric field: the electrons towards the anode and the Ar^+ ions towards the cathode (target). When an ion approaches the target, one of the following may occur:

- i. It may undergo elastic collision and be reflected.
- ii. It may undergo inelastic collision and be buried into the target.
- iii. It may produce structural rearrangement in the target material.
- iv. The impact may set up a series of collisions between atoms of the target leading to the ejection of one of these targets; this process is known as sputtering.

Different mechanisms of sputtering according to the incidental ion energy are illustrated in figure 3.2 [1]. When the energy of the ions is lower than 100 eV the transferred energy is sufficient to eject the atoms of the target but too weak to provoke some collisions in cascade. This mechanism is called simple collision regime.

For ions possessing energy between 100 eV and 1 keV, the atoms of the target acquire enough energy to enter in collision with its neighbors: the regime of collisional cascades. If the energy is superior to 1 keV, there occurs an important motion of the atoms situated in the zone of interaction of the incidental ion which can provoke a strong local temperature elevation (10^3 to 10^4 K); it is the thermal porosity regime.

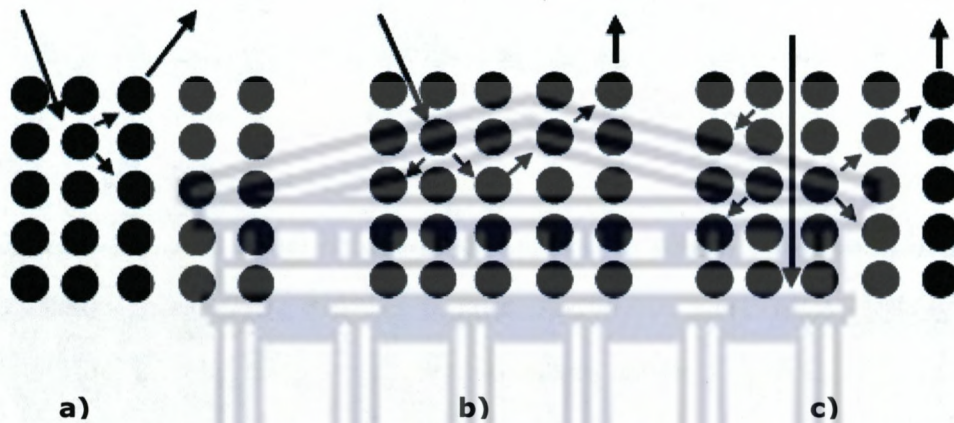


Figure 3.2: Sputtering mechanisms: a) Simple collision; b) Collisional cascades; c) thermal porosity [1].

Thus the sputtering process can be likened to a break in a game of "atomic" billiards. The excited ion, representing the cue ball, strikes the atomic array of the target - the neatly arranged pack - scattering them in all directions. Some of these will be ejected in the direction of the original approaching ion i.e. normal the target surface. It is this ejected particle which is useful for deposition on the surface of the wafer. Hence the sputter process essentially involves knocking an atom or molecule out of the surface of a target. Under the right conditions, the sputtered species will travel through space until it strikes and condenses on the surface of the substrate. For further detail see reference [2].

3.1.3 Characteristics of RF magnetron sputtering

3.1.3.1. Ionic frequency

When one applies a difference of high potential between two electrodes situated in a gas with reduced pressure, an electric discharge occurs that generates plasma. The target is located in the cathode and the substrate in the anode. The different transfers of energy electron-atom necessary for the production of different species contributing in the sputtering will be outlined below.

The electric excitation is produced by a radiofrequency potential that permits to maintain the discharge contrary to a continuous potential when one has an insulating target. However all frequencies do not permit the discharge to be effective, in this case it will be necessary to introduce a physical parameter named ionic frequency or cut frequency capable to generate or maintain the discharge. This frequency is the response of the ions to an alternative electric field. It is expressed by a formula:

$$f_{pi} = \frac{1}{2\pi} \left(\frac{n_i e}{m_i \epsilon_0} \right)^{\frac{1}{2}}$$

Where n_i is the number of ions per volume unit or density of ions, m_i ions mass, e electric charge and ϵ_0 vacuum permittivity.

For applied frequencies lower than to f_{pi} , the ions follow the variations of the electric field, the discharges are then similar to the phenomenon continuous current, but with a polarity that reverses itself at every half period. For frequencies superior than f_{pi} , the ions response uniquely to the temporal average of the electric field. In similar way the electronic frequency of plasma is defined as:

$$f_{pe} = \frac{1}{2\pi} \left(\frac{n_e e}{m_e \epsilon_0} \right)^{\frac{1}{2}}$$

where n_e is the number of electrons per volume unit or density of electrons, m_e electrons mass, e electric charge and ϵ_0 vacuum permittivity.

The condition is so that the electrons follow the variations of the electric field and that the motion of ions be only induced by the electric field, the applied frequency should then be ranged between f_{pi} and f_{pe} . Figure 3.3 clearly indicates the ionic frequency as a function of ion mass of different ions such as H^+ , He^+ , Ne^+ , Ar^+ and Xe^+ .

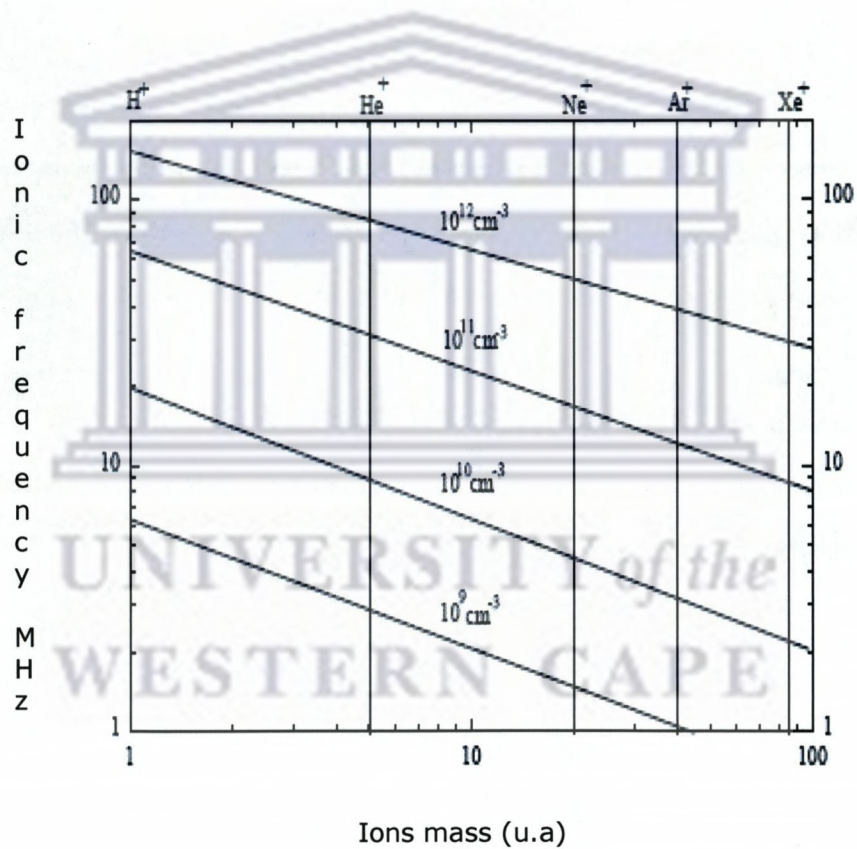


Figure 3.3: Ionic frequency as a function of ion mass [3].

3.1.3.2. Auto polarization

In the case of an electric radiofrequency, a capacitive coupling between the generator and the electrodes is established where plasma occurs by placing a capacitor of blockage in series with the cathode, the other electrode carrying the substrate (anode) being at the potential zero.

3.1.3.3 Magnetron sputtering

The permanent magnets placed behind the cathode produce magnetic fields. The field lines bend to give a component parallel to the target surface. Electrons from the plasma are more confined in this region due to this magnetic field component and are subjected to crossed electric and magnetic fields. As a result, they are forced to move in a cycloidal path. In the region where the confinement of electrons is more effective, the ion population also increases due to the high ionization rate. The ions hit the target gaining high energy and thereby produced sputtered atoms. This region of the target where heavy erosion takes place is known as the racetrack.

3.1.4 The Sputter Parameters

The resulting film properties can be controlled by adjusting the following sputter parameters:

The *sputter current* I_{SP} determines mainly the rate of the deposition process and hence the time which remains for the arriving particles during the growth process for either surface diffusion and agglomeration on existing growth centers or nucleation with other adatoms.

The *applied voltage or rf power* determines the maximum energy, with which sputtered particles can escape from the target (reduced by the binding energy). Energies of the sputtered particles show a broad distribution with a maximum of the distribution between 1 eV and 10 eV. The applied voltage determines also the sputter yield, which is the number of sputtered particles per incoming ion.

The *pressure* (P) in the sputter chamber determines the mean free path (λ) for the sputtered material, which is proportional to $\frac{1}{P}$. Together with the target substrate distance (T-S), the pressure controls how many collisions occur for the particles on their way from the target to the substrate. This can influence the porosity of the films. But also the crystallinity and texture can be affected [4]. Via the gas mixture, one can control the stoichiometry of the films, which are sputtered from a metallic target. The *oxygen flow* $P(\text{O}_2)$ is the parameter varied, whereas the desired total pressure is kept constant by regulation of the Ar-flow $P(\text{Ar})$.

The *substrate temperature* can have a strong impact on the growth behavior with respect to crystallinity or density of the samples. But even during sputtering without external heating the substrate temperature may rise considerably, especially during long sputtering times for the deposition of thick films.

In principle a *bias-voltage* can be applied to the substrate which has the effect of accelerating electrons or ions towards the substrate or keeping them away. Both may have an influence on the layer growth as reported in the literature [5]. Usually substrate and target surface are parallel to each other. A variation of the deposition angle (also: sputtering under oblique incidence) can be achieved by tilting the substrate. Thereby a new preferential direction for the film growth and potentially anisotropic films can be produced.

3.2 Choice of the deposition method of VO₂ and Au-VO₂ thin films

The realization of thin films of VO₂ and Au-VO₂ requires the mastery and control of their synthesis. The choice of the deposition method demands several criteria:

- the nature of the materials to deposit
- the rate of the deposition
- the nature of the substrate to be used
- the stoichiometry desired

- the adhesion of the films on the substrate
- the reproducibility and scalability of the technique
- the cost effective of the technique

In this work, we chose radiofrequency inverted cylindrical magnetron sputtering (ICMS) technique known as hollow cathode sputtering for the synthesis of our thin films of VO_2 and Au- VO_2 nanocomposite. This novel deposition technique presents great promises over others vapour deposition techniques. Its complete description and comparison with others vapour deposition techniques are presented in the section of ICMS.

3.3 Radiofrequency Inverted cylindrical magnetron sputtering (ICMS)

3.3.1 ICMS features

Cylindrical magnetron sputtering described in a series of patents by Penfold and Thornton issued in the mid-1970s were among the first magnetrons developed [6-7], and has long been used to coat materials at high rates onto complex shapes, such as those used in the biomedical, aerospace, and machine tool industries.

3.3.2 Description

The ICM gun as illustrated in figure 3.4 is mounted in a double cross-piece vacuum chamber on a standard DN 100 CF flange with a mounting depth of 120 mm. The rings magnets and cylindrical target assembly are attached to a water cooled backing plate that limits heat buildup in the target and magnets. The substrate holder is situated 2cm from the sputtering head. The temperature of the substrate heater is controlled by a thermocouple k-type thermocouple with an Omega CN 370 temperature controller capable to reach 700 °C. Thermal contact between the heater and the substrates was achieved by painting the back of the substrate with silver paint and curing these at 100

°C for 10 min. The substrates were then attached to the substrate holder with an additional film of silver paint.

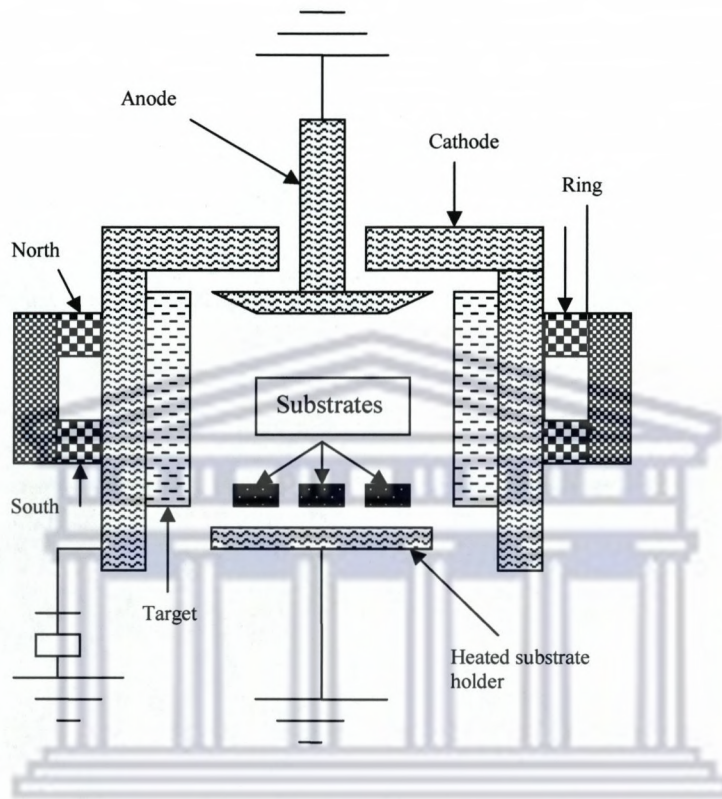


Figure 3.4 Schematic illustration of the Inverted Cylindrical Magnetron (ICM) sputter gun [8].

The vacuum chamber is evacuated by a diffusion pump backed by a rotary pump. The vacuum system is separated from the deposition section by a pneumatic gate valve which is bypassed by a constricted diameter bellows tube with an adjustable flow control valve. This allows for differential pumping on the upper and lower chambers thus enabling the use of high gas pressures needed during the sputtering without causing damage to the diffusion pump. The gate valve is opened during the pump-down stage for fast evacuation of the chamber and kept semi-closed during the deposition. High purity Argon and mixture Oxygen (10%) and Argon gases are fed into the gun positioning and the vacuum components.

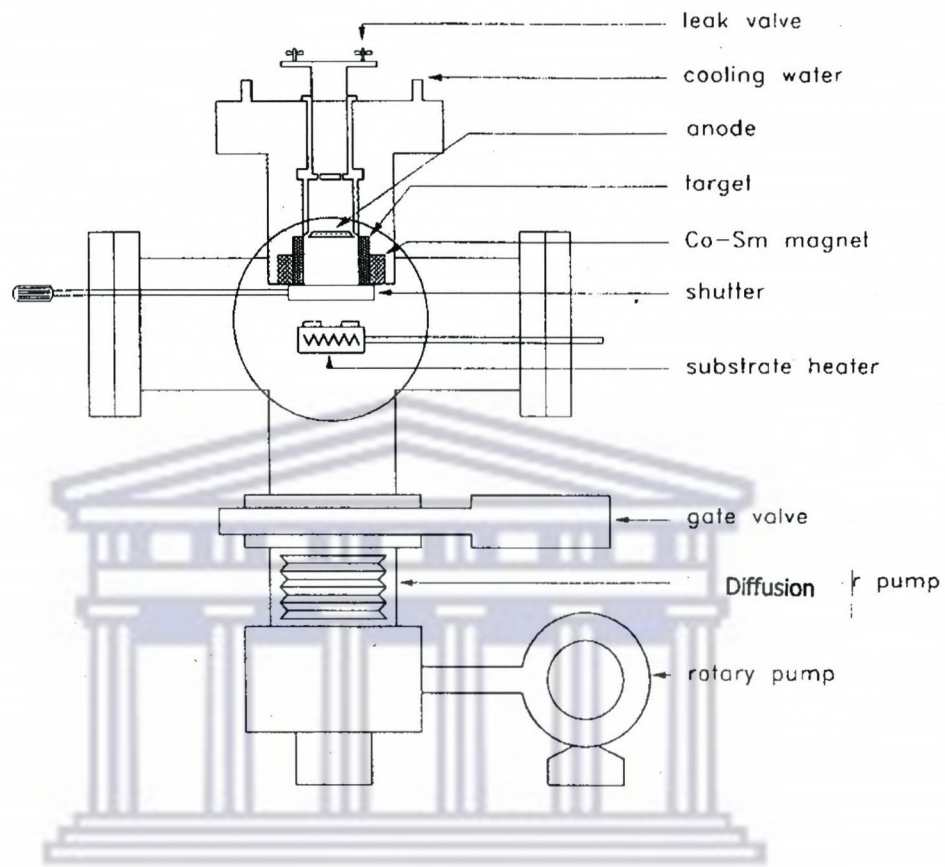


Figure 3.5: Schematic illustration of the sputter deposition system showing the ICMS

A Cesar Dressler, high-frequency generator is used as the power supply for the ICM gun, generating electromagnetic power in the MHz-region (typical: 13.56 MHz). The output voltage and current capabilities of these generators are limited. The plasma impedance is normally different from this, so a matching network is connected to the cathode to transform the cathode impedance to power needed by the generator. When the alternating signal is applied to the cathode, generating plasma, then the plasma acts as a rectifier that generates an average negative voltage at the smaller of both electrodes, which is in general the target. This negative voltage is called the self-bias or V_{DC} voltage of an radiofrequency cathode.

3.4 Comparison of conventional methods and new method ICMS

The main limitations of conventional methods are illustrated in table 3.1. These properties illustrated in table 3.1 strongly indicate that ICMS has sufficient possibilities to prepare new nanocomposite systems with a wide range of practical applications. ICMS is a promising candidate to prepare new nanocomposite films with uniform coating on complex shapes which are required for a variety of applications, ranging from X-ray telescope mirrors to biomedical implants.

Table 3.1: Comparison of conventional methods and new method by ICMS for preparing nanocomposites films.

	Conventional PVD methods	New method
Coating method	Co-sputtering, RF or AC planar magnetron sputtering, Pulsed laser ablation, and other methods	Rf-inverted cylindrical magnetron sputtering (ICMS)
Coating complex shapes	Difficult	Easy
Geometry and high sputtering pressure	Do not eliminate the adverse effects of negative ion bombardment of the growing film (back sputtering)	Eliminate back sputtering
Target cost	High	Lower
Target utilization	Good	Very good

Coating efficiency	Low	Quite high
Coating flux	Anisotropic	Isotropic
Average deposition rate	High	Very high
Range of distribution of metal nanoparticles	Good	Very good
Reproducibility and scalability	Good	Very good
Thickness of nanocomposites films	Thin film	Thin and thick film

3.5 Characterization techniques

3.5.1. Atomic force microscopy

Atomic Force Microscopy (AFM) modes enable speciality measurements of surface properties and tip-sample interactions. Surface charge density, potential, conductivity, and capacitance are some important electrical surface properties measured by AFM modes. Additional modes are also possible for the analysis of magnetic and thermal properties of the sample although specific probes may be required. Measurements of surface properties and tip-sample interactions are extremely important for the investigation of, for instance, surface electronic states, corrosion processes and surface chemistry in general. AFM modes can also be used as a tool for lithographic applications.

3.5.1.1 Principles

During the last twenty years, the atomic force microscopy (AFM) has become one of the most widely used methods for characterizing the surface structure of solid materials. First, the atomic force microscope was only used as an imaging tool, similarly to the optical and scanning electron microscopes as it allows us to construct a three-dimensional image of the sample surface. The main advantages compared to the other microscopic techniques are the larger resolution (going down to the atomic resolution), almost no sample preparation, large area of materials that can be measured and non destructivity of the method. Some others methods detecting more than the interatomic forces appeared such as the magnetic force microscopy (MFM), electric force microscopy (EFM), scanning thermal microscopy (SThM), near-field scanning optical microscopy (NSOM). However, all these methods are basically only extensions of the basic AFM scheme. Information about the surface of a sample can be gained by employing atomic force microscopy (AFM). The information about the surface roughness can be used to extrapolate information on the growth mode of a given sample. A typical setup for an AFM is shown in figure 3.6. The sample surface (F) is placed under the (ideally) atomically sharp tip of a cantilever (B). The tip is brought into close proximity of the sample surface. The forces between the tip and the sample lead to a deflection of the cantilever according to Hooke's law, where the spring constant of the cantilever is known. Typically, the deflection is measured using a laser spot (A) reflected from the top of the cantilever into an array of photodiodes (D). If the tip were kept at constant height, there would be a risk that the tip would collide with the surface, causing damage. Therefore, in most cases a feedback mechanism is employed to adjust the tip-to-sample distance. This way it is possible to keep the force between the tip and the sample constant. Generally, the sample is mounted on a piezoelectric tube. With this tube the sample can be moved in the z direction, thus maintaining a constant force. The x and y directions can be moved for scanning the

sample. The image recorded in this way resembles the surface topography of the sample.

Many different modes of operation have been developed over the years for the AFM. The most commonly used ones are contact mode, non-contact mode, and dynamic contact mode. In contact mode operation, the force between tip and the surface is kept constant during scanning by maintaining a constant deflection. For the non-contact mode it is possible to have the cantilever oscillating at or close to its resonance frequency by means of an external force. The tip-sample interaction force modifies the oscillation. Information on the sample characteristic can be gained through monitoring the changes in the oscillation with respect to the external reference. The problem with this mode is that most samples develop a liquid meniscus layer. Keeping the tip close to the surface while at the same time preventing it from getting stuck in the meniscus layer is a big problem in ambient conditions. To circumvent this problem, the dynamic contact mode was developed by Zhong et al. [9].

In this mode, the cantilever is oscillated with so much force, that even though it gets into direct contact with the surface on each oscillation, it gets detached from it again. The non-contact and dynamic contact mode operation can be used for example either under frequency modulation or the more common amplitude modulation. When measuring with frequency modulation, information about a sample's characteristics is provided by monitoring changes in the oscillation frequency. Amplitude modulation, which is better known as intermittent contact or tapping mode, provides information on the sample surface topography by monitoring changes in the oscillation amplitude. It is also possible to discern between different kinds of materials on the surface by analyzing the phase of the oscillations in tapping mode.

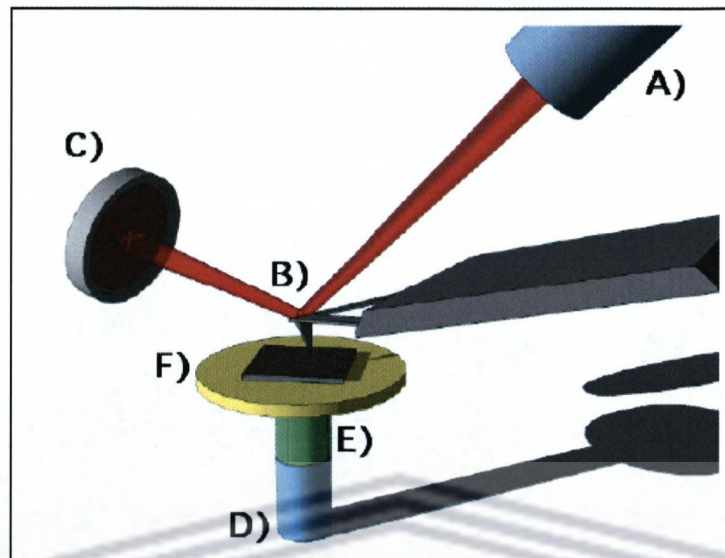


Figure 3.6: An explicative cartoon of AFM working principle. It is possible to recognize the laser (A) focusing a laser beam at the top end of a cantilever (B) from where it is reflected at the center of a 4 quadrants photodiode (C). Every cantilever deformation (bending or torsion) will be easily detected as spot movements on the photodiode. At the end of cantilever there is a very sharp tip in close proximity with the sample surface (F). The sample surface is moved below the tip using an x and y piezoscanner (E). During the rastering process the tip bends (or changes its resonant frequency) as a function of surface morphology. A z piezoscanner (D) approaches or moves away the surface (F) from the tip in order to maintain constant bending or resonant frequency. Voltages needed to do these corrections are used to reconstruct surface topography [10].

3.5.1.2 AFM measurements and possible error sources

AFM measurements can suffer from various error sources originating in the measurement system and its principles. Between the most problematic error sources we can cite these:

Piezoceramics errors: Piezoceramic scanners are one of the critical parts of the atomic force microscope. They are used to move the tip or sample in all three directions with a subatomic precision. This is in principal a problematic task and therefore most of the errors are caused by or related with these scanners. Unfortunately, the piezoceramics is a very bad material for a precise instrument construction. It exhibits nonlinearity, hysteresis and many other error sources. Nevertheless, currently it is the only way how to move the tip/sample with a subnanometric precision. Basically, we can observe these error sources for the piezoceramics:

creep is related to the effect of the applied voltage on the remanent polarization of piezoceramics. When applied voltage, only approximately 95% of the expected piezoceramics movement follows immediately. After this, with the same voltage applied, the scanner still moves slightly with a logarithmically decreasing speed. After hours, this can lead to a few percent changes in the scanner position (the rest of the expected movement). For the open loop instruments, the creep can be eliminated electronically, applying first larger voltage than it would be necessary for a short time and than decreasing it slowly after the scanner had moved the expected distance.

hysteresis is based on the crystalline polarization effects of the material used for piezo scanner. The detection of the piezoceramics depends on whether it was previously operated at higher or lower voltage - e. g. it depends on the direction of movement. Hysteresis is typically within 10 % of the motion. This effect can be reduced by applying different voltages in both the directions,e.g. by an electronic or software corrections of the applied voltages.

intrinsic nonlinearity is an effect present for all the piezoceramics. The same voltage change does not produce the same detection change in all the scanner ranges. Even the change in length of the piezoceramics should be linear with

the linearly changed voltage for most of the materials (however, also piezoceramics with the quadratic dependence are sometimes used), some amount on nonlinearity is always present. Therefore, the non-linear voltage change must be applied to the scanner to ensure the linear movement.

aging is connected with changing the properties of the piezoceramics slightly with time. It can lead to big errors if we do not take this into account. Therefore the calibration must be performed very often to ensure that the scanner is well calibrated.

System geometry effects: The configuration of the scanners directly affects the precision of the system. Even for the three-scanner configuration shown in Fig. 3.6 the system does not follow a plane in the XY direction. Instead of it, it follows a spherical surface having a center at the mounting point. The curvature can be easily further enlarged by enlarging the distance between the mounting point of the scanner and the tip. Even better from this point can be systems where the scanner exhibits only the Z-motion and the sample is moved in the X-Y plane. However, this configuration implies limitations on the sample size and mass. For the one-scanner configuration (detecting tube scanner for high resolution) the situation is even worse than for the three scanner one. The resolution of AFM in X,Y is in the range of 2-10 nm and 0.05 nm in the Z direction.

Thermal effects: As the thermal expansion coefficient of the materials used for the scanning head construction can be in order of 10^{-6} (stainless steel), even a very small change in the temperature can introduce a thermal movement between the tip and sample while working in the high resolution mode. This is often observed while starting scanning or after changing the scanner or the tip. This effect can be reduced by a highly symmetrical system configuration, by means of using construction materials having low thermal expansion coefficients or by waiting until thermal equilibrium is reached.

Noise and vibrations: Noise and vibrations can dramatically reduce the system resolution, namely for the atomic-scale experiments. Therefore, two step damping systems are usually used to eliminate these effects. First, there is a large and heavy system (i. e. a pneumatic table) having very low resonance frequency that limits the high-frequency noise and vibrations (and transmits the low-frequency components). Second, the AFM head is manufactured to have high resonance frequency and therefore not to be affected by the low frequency noise transmitted by the table. However, even that system must be in a quiet and noise-free place to ensure the good performance.

Tip convolution: All the images produced by means of the scanning probe microscopy method are the product of the tip-sample convolution. Only an ideal tip (i. e. a tip having a delta-function like shape) would produce the real topography; all the other tips will leave some information about their shape in the image which leads to systematic errors. The magnitude of these errors depends on the geometry of both the tip and sample and also on the sampling of the image measured.

The piezoceramics properties are usually compensated for by using a closed loop instrument that uses independent devices for measuring scanner position (e. g. interferometers or strain gauges). The noise and thermal drift effects can be minimized by a proper instrument setup and measurement. The only effect that is principal and cannot be reduced in a simple way is the tip convolution. For more details please read [11].

3.5.2. Conductive Atomic Force Microscopy (C-AFM)

3.5.2.1 Background

Conductive Atomic Force Microscopy (C-AFM) is a secondary imaging mode derived from contact AFM that characterizes conductivity variations across medium- to low-conducting and semiconducting materials. C-AFM performs general-purpose measurements, and has a current range of 2 pA to 1 μ A. C-AFM is used for recording

simultaneous topography imaging and current imaging. Specifically, standard conductive AFM operates in contact AFM mode. Current measurement from the sample (presumably a large conductive surface) can be significantly noisier due to capacitive phenomena over the large surfaces. Variations in surface conductivity can be distinguished using this mode. C-AFM operates in contact AFM mode by using a conductive AFM tip. The contact tip is scanned in contact with the sample surface. Just like contact AFM, the Z feedback loop uses the DC cantilever deflection signal to maintain a constant force between the tip and the sample to generate the topography image. At the same time, a DC bias is applied to the tip while the sample is held at ground potential. It is a useful technique in a wide variety of materials characterization applications including dielectric films, conductive polymers and biomaterials [10]. A typical schematic of C-AFM is illustrated in Figure 3.7.

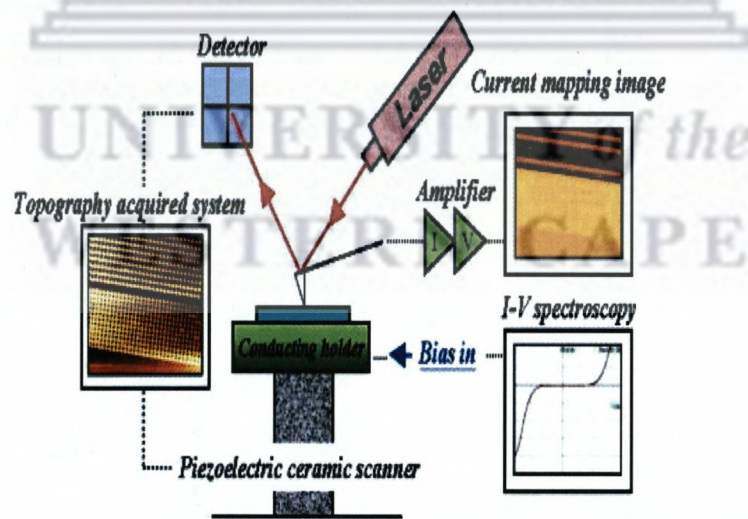


Figure 3.7: Typical schematic of Conductive Atomic Force Microscopy [12].

3.5.2.2 Equipments used

Knowing all error sources, many precautions have been taken during the measurement in order to have better quality of images. AFM measurements for this work were performed in tapping mode on a Digital Instruments Nanoscope IIIa of the Materials Research Department-Ithemba LABS. Nanoscope III 5.12 r3 and Paint Photoshop Pro software were used to treat AFM images and extract some surface roughness parameters such as root mean square roughness (Rms) , difference between the highest and lowest points in the scan range (Z-range) and so on. C-AFM was done at Nanostructure laboratory at Elettra-Italy using NMDT technology.

3.5.3 Scanning Tunneling Microscopy

3.5.3.1 Background

The first practical demonstration of the STM was described by Binnig, Rohrer, Gerber and Weibel, 1982 [13] and led to the award of the Nobel Prize for Physics in 1986 to Binnig and Rohrer. The Scanning Tunneling Microscopy (STM) is intended for the investigation of the surfaces properties of conductive materials with resolution down to atomic scale. The tunnel current recorded during scanning is small enough (0.5 pA -50 nA) to allow investigating samples with low conductance, biological samples in particular. The resolution of the STM, as a near-field scanning microscope, is not limited by Abbe's criterion as in any microscope using lenses to form the image (a far-field microscope), but simply by the smallest tip diameter and tip-sample spacing that can be achieved. The lateral resolution (X,Y) is about 1\AA (0.1 nm) whereas a vertical resolution (Z) up to 0.01\AA can be achieved. The STM can be used in ultra high vacuum, air or other environments [14].

STMs use a sharpened, conducting tip with a bias voltage applied between the tip and the sample. When the tip is brought within about 10\AA of the sample, electrons from the sample begin to "tunnel" through the 10\AA gap into the tip or vice versa, depending

upon the sign of the bias voltage. The resulting tunneling current varies with tip-to-sample spacing, and it is the signal used to create an STM image. For tunneling to take place, both the sample and the tip must be conductors or semiconductors. Unlike AFMs, STMs cannot image insulating materials.

Each mode has advantages and disadvantages. Constant-height mode is faster because the system doesn't have to move the scanner up and down, but it provides useful information only for relatively smooth surfaces. Constant-current mode can measure irregular surfaces with high precision, but the measurement takes more time. Application of special modes allows investigating the surface distribution of various electrical characteristics, such as work function, local density of electron states, etc. As a first approximation, an image of the tunneling current maps the topography of the sample. More accurately, the tunneling current corresponds to the electronic density of states at the surface. STMs actually sense the number of filled or unfilled electron states near the Fermi surface, within an energy range determined by the bias voltage. Rather than measuring physical topography, it measures a surface of constant tunneling probability. One of the STM limitations is the complexity of interpretation of the obtained results, since the STM image is determined not only by the topography, but also by the local electrical characteristics.

3.5.3.2 Applications of the STM

The scanning tunneling microscope (STM) is widely used in both industrial and fundamental research to obtain atomic-scale images of metal surfaces. It provides a three-dimensional profile of the surface which is very useful for characterizing surface roughness, observing surface defects, and determining the size and conformation of molecules and aggregates on the surface. It is also tempting to use a selection of images of surfaces with atomic resolution. The tip of an STM always exerts a finite force on an adsorbate atom, made up from both van der Waals and electrostatic

contributions. Changes to the position and bias voltage of the tip allow one to alter the magnitude and direction of this force. Since it is generally easier to move an atom along a surface rather than to detach it from the surface, it is possible, in principle, to set the tip parameters so that an individual atom is pulled across the surface yet remains bound to it. For more details please read references [15-17].

a) Modes of operation

STM has different modes of operation such as Constant Current Mode, Constant Height Mode, Barrier Height Imaging and Scanning Tunneling Spectroscopy. In this work, we used the scanning tunnelling spectroscopy mode and we recorded a current-voltage (I-V) of a single nanograin of sputtered VO₂.

b) Technical aspects

Demands

- Controlling the tip-sample distance from a few mm down to 0.01Å
- Exact lateral positioning
- Stabilized tip-sample distance
- Sharp tip
- Measuring a current in the range of 0.01nA-50nA

c) Positioning

The large distance range the tip has to be controlled on makes it necessary to use two positioners: a coarse and a fine positioner. The fine positioner is also used as a scanner. Every fine positioner/scanner is made out of a piezocrystal or piezoceramic material.

d) Electronic Circuit

In case of measuring in the constant current mode a feedback circuit has to be build up to control the z-piezo.

e) Vibration Isolation

The tip-sample distance must be kept constant within 0.01\AA to get good atomic resolution. Therefore it is absolutely necessary to reduce inner vibrations and to isolate the system from external vibrations.

Environmental vibrations are caused by:

- Vibration of the building 15-20 Hz
- Running people 2-4Hz
- Vacuum pumps
- Sound

f) Tip

The tip is the trickiest part in the STM experiment. It needs a small curvature to resolve coarse structures. For atomic resolution, a minitip with a one atomic end is necessary.

3.5.4. Scanning tunneling spectroscopy (STS)

3.5.4.1 Background

Scanning tunneling spectroscopy (STS) is a powerful experimental technique in STM that uses a scanning tunneling microscope (STM) to probe the local density of electronic states (LDOS) and band gap of surfaces and materials on surfaces at the atomic scale [1]. Generally, STS involves observation of changes in constant-current topographs with tip-sample bias, local measurement of the tunneling current versus tip-sample bias (I-V) curve, measurement of the tunneling conductance, dI / dV , or

more than one of these. Since the tunneling current in a scanning tunneling microscope only flows in a region with diameter $\sim 5 \text{ \AA}$, STS is unique in comparison with other surface spectroscopy techniques, which average over a larger surface region. From the obtained I-V curves, the band gap of the sample at the location of the I-V measurement can be determined. By plotting the magnitude of I on a log scale versus the tip-sample bias, the band gap can clearly be determined. Although determination of the band gap is possible from a linear plot of the I-V curve, the log scale increases the sensitivity. Alternatively, a plot of the conductance dI / dV versus the tip-sample bias V allows one to locate the band edges that determine the band gap. The structure in the dI / dV , as a function of the tip-sample bias, is associated with the density of states of the surface when the tip-sample bias is less than the work functions of the tip and the sample. A typical schematic of STM is illustrated in Figure 3.8.

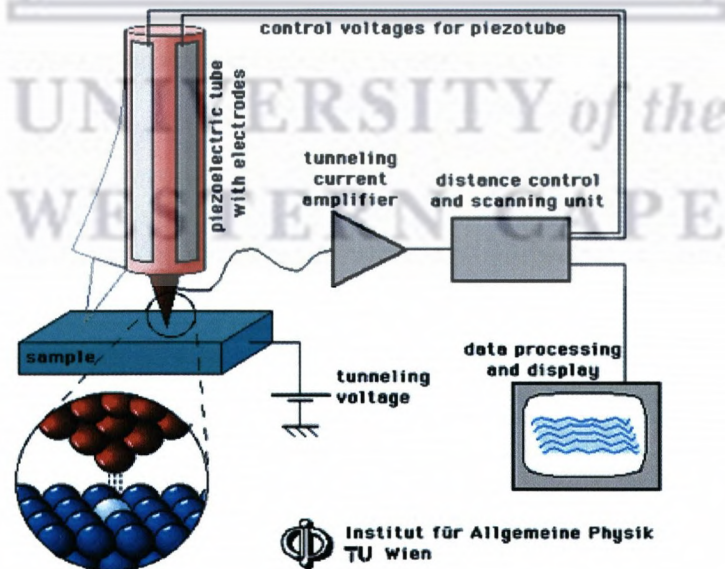


Figure 3.8: Typical schematic of Scanning Tunneling Microscopy [18].

3.5.4.2 Equipment used

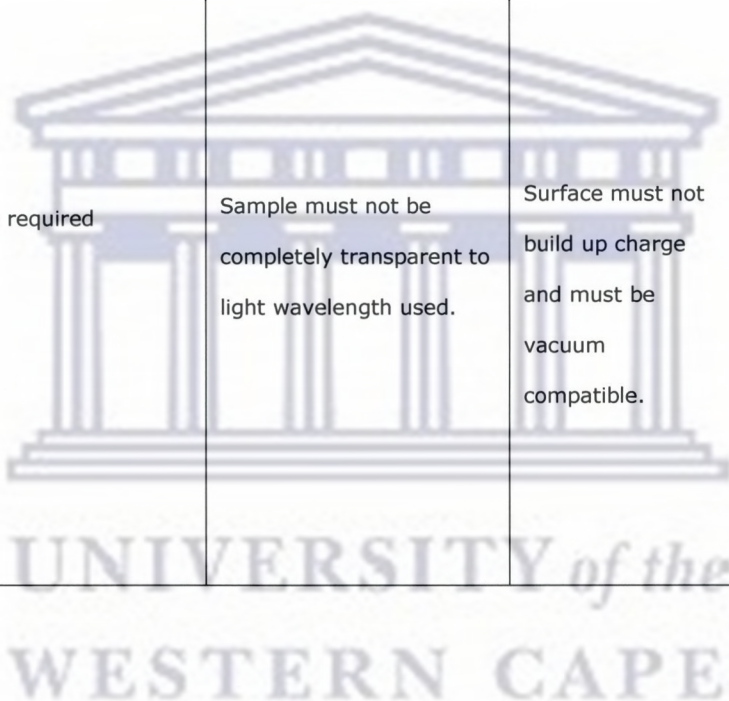
The STM measurements presented in this work have been performed at the University of Oman-Saudi Arabia and nanostructure laboratory-Elettra at Italy for the reproducibility purpose. STM imaging measurements were carried out at different temperatures in order to follow the phase transition of VO₂ thin film and I-V curve was recorded for a single nanograin as selected area.

View a complete description of Scanning probe Microscope (SPM), the comparison and the characteristics of common microscopic techniques such Optical microscope, Scanning Electron Microscope (SEM) and SPM are given below in table 3.2.

Table 3.2: Comparison and the characteristics of common microscopes

Characteristics of Common Microscopic Techniques for Imaging and Measuring Surface Morphology			
	Optical Microscope	SEM	SPM
Sample operating environment	Ambient air, liquid, or vacuum	Vacuum	Ambient, air, liquid, or vacuum
Depth of field	Small	Large	Medium
Depth of focus	Medium	Large	Small
Resolution: X, Y	1.0µm	5nm	2-10nm for AFM 0.1nm for STM

Resolution: Z	N/A	N/A	0.05nm
Effective magnification	1X - 2x10 ³ X	10X - 10 ⁶ X	5x10 ² X - 10 ⁸ X
Sample preparation requirement	Little	Little to substantial	Little or none
Characteristics required for sample	Sample must not be completely transparent to light wavelength used.	Surface must not build up charge and must be vacuum compatible.	Sample must not have local variations in surface height >10µm.



3.5.5. X-RAY REFLECTIVITY

X-ray reflectivity (XRR) has become an invaluable tool to study the structure and the organization of materials which are grown as thin films at the submicron and atomic scales [19-22]. In thin film material research, the trend is to design solid films of increasing complexity having specific properties for technical applications.

Using a simulation or the least-squared fit of the reflectivity pattern, one can obtain accurate information of thickness, interface roughness and layer density for either

crystalline or amorphous thin films or multilayers. The roughness of the interfaces is a crucial importance for many technological applications and it is a parameter which must be determined to appreciate the quality of the interfaces.

3.5.5.1. Basic principles of X-ray reflectivity

a) The index of refraction

X-rays are part of the broad spectrum of electromagnetic waves. X-rays can be produced by the acceleration or deceleration of electrons either in vacuum (synchrotrons) or in metallic targets (tubes). The most widely used X-rays in materials science have a typical wavelength, λ , of the order of 0.1 nm. This wavelength is associated with a very high frequency of the order of 10^{19} Hz which is at least four orders of magnitude greater than the eigen frequency of an electron bound to a nucleus. A consequence, the interaction of the X-rays with matter can be well described (in a classical way for a first approach) by an index of refraction which characterizes the change of direction of the X-ray beam when passing from air to a material. A very classical model in which an electron of the material is considered to be accelerated by the X-ray field shows that the index of refraction for X-rays can be written as $n=1-\delta-i\beta$ where δ and β account for the scattering and absorption of the material, respectively. The sign preceding β depends on the convention of signs used to define the propagation of the electric field. The values of δ and β (which are positive) depend on the electron density ρ and linear absorption coefficient μ of the material through the following relations:

$$\delta = \frac{r_e \lambda^2 \rho}{2\pi} \quad \text{and} \quad \beta = \frac{\lambda \mu}{4\pi}$$

Where $r_e = 2.813 \times 10^{-6}$ nm is the classical radius of the electron.

b) The critical angle of reflection

For X-rays, the refractive index of a material is slightly less than unity [8]. Passing from air ($n=1$) to the reflecting material ($n<1$), it is possible to totally reflect the beam if the incident angle θ (which is the angle between the surface of the sample and the incident beam) is small enough. This is known as the total external reflection of X-rays. For this to occur, the incident angle must be smaller than the critical angle θ_c defined as

$$\cos\theta_c = n = 1 - \delta.$$

Since n is very close to unity, this angle is very small and the Taylor approximation in θ_c yields

$$\theta_c^2 = 2\delta = \frac{r_e \lambda^2 \rho}{\pi}$$

The domain of validity of X-ray reflectivity is limited to small angles of incidence where it is possible to consider the electron density as continuous. The wave vector transfer module is defined as

$$q_z = \frac{4\pi \sin \theta}{\lambda}$$

when θ is very small, we obtained a critical wave vector transfer module

$$q_c = \frac{4\pi \theta_c}{\lambda}$$

Sometimes at small grazing angles ($\theta < \theta_c$), the incoming beam is totally reflected giving rise to the plateau of total reflection. Over this region ($\theta > \theta_c$), usual interference fringes so called "Kiessig fringes", due to the finite film thickness, are observed. The simulation of total reflection plateau and Kiessig fringes allow to deduce mean electron density, total thickness and interfacial roughness of each film. The thickness of the film d is related to the maxima positions θ_m by:

$$\frac{1}{2}(2m+1)\lambda = 2d\sqrt{\theta_m^2 - \theta_c^2}$$

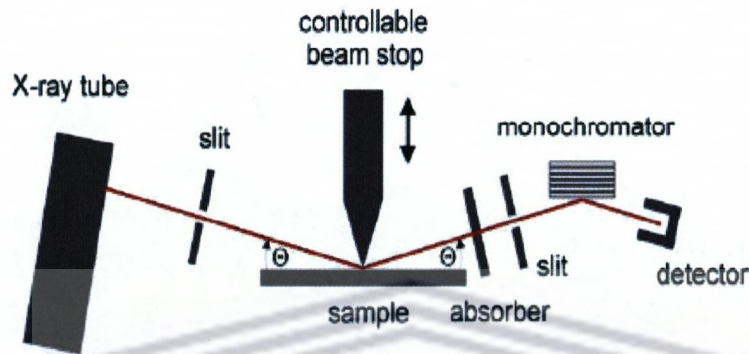


Figure 3.9: Illustration of the setup of X-ray reflectivity.

For composite materials by example Au-VO₂, by knowing the mean electron density in the electron density profile determined by simulation, it is possible to determine the volume fraction of gold.

Example:

$$\rho = \frac{M}{V} = \left(\frac{M_{Au} + M_{VO_2}}{V_{Au} + V_{VO_2}} \right)$$

$$\text{Hence } M_{Au} = \rho_{Au} V_{Au} \text{ and } M_{VO_2} = \rho_{VO_2} V_{VO_2}$$

$$\rho = \frac{\rho_{Au} V_{Au}}{(V_{Au} + V_{VO_2})} + \frac{\rho_{VO_2} V_{VO_2}}{(V_{Au} + V_{VO_2})}$$

$$\rho = \rho_{Au} \phi_{Au} + \rho_{VO_2} (1 - \phi_{Au})$$

From the literature $\rho_{Au} = 4.4247$ and $\rho_{VO_2} = 1.30$. $\rho = \rho_{Au-VO_2} = 1.5$ value obtained by simulation in the electron density profile. By simple calculation, one can easily determined $\phi_{Au} = 6.3\%$ in volume.

3.5.5.2. Equipment used in this work

X-ray reflectivity at wavelength of 1.54 Å on a Panalytical X-pert reflectometer of the Laboratoire de Physique de l'Etat Condensé - Université du Maine France was used for the analysis of the surface and interface of the VO₂ and Au-VO₂ thin films. This experiment has been carried out with the collaboration of Prof. Alain Gibaud.

3.5.6. X-Ray Diffraction (XRD)

3.5.6.1. Principle and pattern analysis

X-rays are highly energy electromagnetic radiation. They have energies ranging from about 200 eV to 1 MeV, which puts them between gamma-rays and ultraviolet (UV) radiation in the electromagnetic spectrum.

Diffraction is a general characteristic of all waves and can be defined as the modification of the behaviour of light or other waves by its interaction with an object.

XRD is based on constructive interference of monochromatic X-rays and a crystalline sample. These X-rays are generated by a cathode tube, filtered to produce monochromatic radiation, collimated to concentrate and directed towards the sample.

The interaction of the incident rays with the sample produces constructive interference when conditions satisfy Bragg's law:

$$n\lambda = 2 d \sin\theta$$

This law relates the wavelength of electromagnetic radiation to the diffraction angle and the lattice spacing in a crystalline sample. By scanning a powder sample through a range of 2θ angles, all possible diffraction directions of the lattice should be attained due to the random orientation of the powdered material. Conversion of the diffraction peaks to d-spacings or 2θ angles allows identification of the materials because each material has a set of unique d-spacing or 2θ angles. Typically, this is achieved by comparison of d-spacing or 2θ angles with standard reference patterns called Joint Committee on Powder Diffraction Standards (JCPDS).

Different categories of nanomaterials are synthesized depending on the deposition conditions. We can classify them in three general categories:

1. single crystal
2. polycrystalline
3. amorphous

Polycrystalline material consists of many single-crystal regions called grains, separated by grain boundaries. The grains in polycrystalline materials can have different sizes and shapes. The grains are generally in many different orientations. The boundary between the grains – the grain boundary–depends on the misorientation of the two grains and the rotation axis about which the misorientation has occurred. There are two special types of grain boundary; tilt and twist grain boundary.

In amorphous materials such as glass and many polymers, the atoms are not arranged in a regular periodic manner while in single crystal, the atoms are well arranged in regular ordered pattern in three dimensions.

Practically, using XRD patterns, the grain size of the materials can be estimated using Scherrer's formula [23]:

$$b = \frac{0.9\lambda}{\Delta(2\theta)\cos\theta}$$

where $\Delta(2\theta)$ (in radians) is the full width at half maximum (FWHM) the peak, λ (m) is a wavelength of the radiation and θ the peak position.

3.5.6.2. Equipment used

The XRD measurements presented in this work have been performed at iThemba LABS-Materials Research Department using an advanced diffraction system AXS Bruker diffractometer (CuK α).

3.5.7. UV-Vis-NIR Spectroscopy

Optical properties are among the most fascinating and useful properties of nanomaterials and have been extensively studied using a variety of optical spectroscopic techniques. A basic understanding of the optical properties and related spectroscopic techniques is essential for anyone who is interested in learning about nanomaterials of semiconductors, insulators or metal. This is partly because optical properties are intimately related to other properties and functionalities (e.g. electronic, magnetic, and thermal) that are of fundamental importance to many technological applications, such as energy conversion, chemical analysis, biomedicine, optoelectronics, communication, and radiation detection.

3.5.7.1. Principles

The UV spectroscopy (ultraviolet spectroscopy) is a physical technique of the optical spectroscopy that uses light in the visible (VIS), ultraviolet and near infrared ranges. UV-Vis-NIR spectroscopy is useful to characterize the absorption, transmission, and reflectivity of a variety of technologically important materials, such as thin films pigments, coatings, windows, and filters. This more qualitative application usually requires recording at least a portion of the UV-Vis-NIR spectrum for characterization of the optical or electronic properties of materials.

3.5.7.2. Optical transmission measurements

Since an important signature of the semiconductor-metal phase transition in VO_2 is the change in the optical properties, temperature-controlled optical transmission measurements were found to be the best way to follow the transition and understand the optical properties of the two phases. For that purpose, a single beam of CECIL 2000 Series, Aquarius in the wavelength of 200-1100 nm was used. The sample was mounted on a Peltier thermopump, which had a central small hole to allow the passage of the light. It was electronically controlled to extract or input heat on the sample at

desired rates. The sample was attached using silver paint with the non-coated side facing the Peltier surface. The temperature was measured with a precision thermocouple, whose signal was transferred to a computer to be recorded simultaneously with the optical signal. The optical transmittance measurements, reported and analyzed in Chapter IV and V were intended to characterize the optical properties of the VO₂ thin films and Au-VO₂ plasmonic materials. Therefore, these measurements were taken from room temperature to 100 °C in order to follow the signature of VO₂ as well as the reversible tunability of the plasmon resonance of Au-VO₂.

3.5.7.3. Equipment used

The UV-Vis-NIR of CECIL 2000 instruments- Aquarius, single beam, located at iThemba LABS -Materials Research Department, in the wavelength range of 200 - 1100 nm, attached with a heating and cooling stage was intensively used in this work.

3.5.8. Spectroscopic Ellipsometry

3.5.8.1. Background

Ellipsometry is a versatile and powerful technique for measuring the optical constants and thickness of thin solid films. It has applications in many different fields, from semiconductor physics to microelectronics and biology, from basic research to industrial applications. Ellipsometry is a very sensitive measurement technique and provides unequalled capabilities for thin film metrology. As an optical technique, spectroscopic ellipsometry is non-destructive, contactless, not requires a vacuum, or no reference sample is needed. Ellipsometry measures the change of polarization upon reflection or transmission. The incident and the reflected beam span the *plane of incidence*. Light, which is parallel polarized, is named p-polarized (p-polarised). A polarization direction perpendicular is called s-polarized (s-polarised), accordingly. The "s" is contributed from the German "*senkrecht*" (perpendicular). There are three types

of data typically acquired with the ellipsometer, transmission and reflection intensity and ellipsometry itself.

3.5.8.2. Basic equations of ellipsometry

Reflection ellipsometry is based on measurement of the change in the polarization state of beam light when it is reflected from a surface as shown in Figure 3.10.

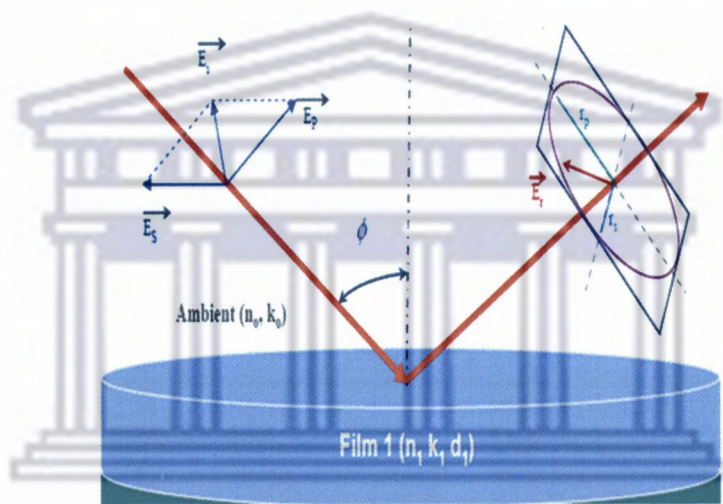


Figure 3.10: Schematic of the geometry of an ellipsometry experiment.

The change in the polarization state measured by comparing the p-component and s-component of the reflection coefficients and is expressed

$$\rho = \frac{R_p}{R_s}$$

ρ is in general a complex number and is defined by two parameters, Ψ and Δ :

$$\rho \equiv \frac{R_p}{R_s} \equiv \tan \Psi \cdot e^{i\Delta}$$

In order words, $\tan \Psi$ is the relation between change in amplitude of the p-and the s-components and Δ is the difference in their phases as shown in Figure 3.11.

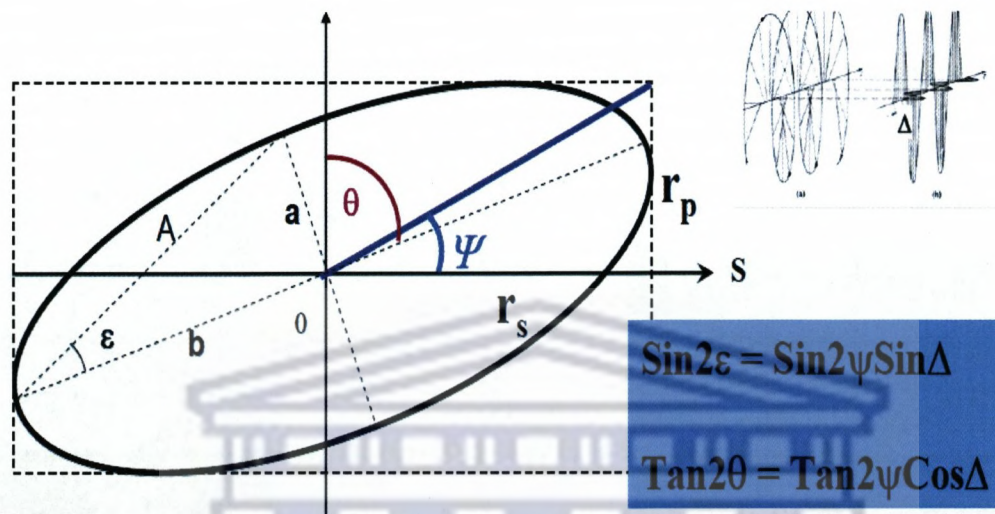


Figure 3.11: The four parameters that define the ellipse of polarization in its plane are the azimuth Ψ , the ellipticity $e = a/b$, the total amplitude A and the absolute phase θ

The complex ratio of Fresnel reflection coefficients ρ can also be expressed in terms of the complex pseudo index of refraction, as given by

$$\langle N \rangle = \langle n \rangle + i \langle k \rangle = N_0 \sin \phi_0 \sqrt{1 + (\tan \phi_0)^2 \left(\frac{1 - \rho}{1 + \rho} \right)^2}$$

Where ϕ_0 the angle of incidence and N_0 is the complex index of refraction of the ambient. The pseudo index of refraction treats a sample as a single material with no overlayer and only for surfaces without overlayers $\langle N \rangle$ is the actual index of refraction.

3.5.8.3. Problems and sources errors

In the theory of ellipsometry, it always assumed that the samples under consideration are ideal, i.e. perfectly smooth interfaces, isotropic materials characterized by its

complex index of refraction, perfectly monochromatic light which is totally polarized. From an experimentalist point view this is not the case. Some of the non-idealities occurring have small influences on the measured data. Ellipsometry is a very sensitive technique and a good knowledge of the saillant problems and error sources is a great advantage. Some of the most common problems that occur when ellipsometry data are acquired are surface roughness which influences the angle of incidence, discontinuous layers, sub-monomolecular layers for biological samples, anisotropy of the films and inhomogeneous layers. Other factors such as bandwidth of the light, mechanical errors, multiple reflections between optical components, depolarization and incorrect model can strongly affect the ellipsometry results. For more details about spectroscopic ellipsometry please read reference [24].

3.5.8.4. Data Analysis for spectroscopic ellipsometry

Spectroscopy ellipsometry like other optical metrology techniques requires:

- Acquiring data (Ψ and Δ). Data is typically acquired versus wavelength and angle of incidence.
- Building an optical model that describes the sample structure using as much information about the substrate and the films as possible.
- Generating theoretical data from the optical model that corresponds to the experimental data.
- Comparing generated data to experimental data. Unknown parameters in the optical model, such as thin film thickness, optical constants or both are varied to try and produce a "best fit" to experimental data. Regression algorithms are used to vary unknown parameters and minimize the difference between the generated and experimental data.
- Physical parameters of the sample such as film thickness, optical constants, surface roughness, composition, etc. are obtained once a good fit to experimental data is achieved.

3.5.8.5. Equipment used

The optical constants n and k at wavelengths ranging from 400 to 1600 nm were determined by analyzing the ellipsometers parameters measured with a Jobin Yvon UVISEL spectroscopic ellipsometer at various temperatures between 25 and 85 °C in heating and cooling process. These measurements were carried out at the University of Bretagne Sud-Research Center, France in collaboration with Professor Guillaume Vignaud.

3.5.9. Rutherford Backscattering Spectroscopy

3.5.9.1. Principles

Ion beams are not only useful to synthesize or modify materials; they can be very helpful in analyzing them. An important analysis of our samples was performed using Rutherford Backscattering Spectroscopy [25] (RBS). RBS was important since it provides an accurate measurement of elemental areal densities as well as depth concentration profiles of the elements.

In RBS, low-atomic mass incident particles (4He^+ , in all our measurements), accelerated to a high energy E_0 (2 MeV in our experiments), impact the sample. As a result, the incident particles scatter from the atomic species in the sample in all directions. The scattering process is mainly elastic. A solid-state detector, located at a convenient angle ($\Theta = 160^\circ$ in our case), measures the energy E_1 and quantifies the yield of backscattered ions. The identification of the elements present in the sample comes simply from the relationship:

$$K = \frac{E_1}{E_0}$$

K is the kinematic factor which is given by:

$$K = \left[\frac{(M_2^2 - M_1^2 \sin^2 \theta)^{\frac{1}{2}} + M_1 \cos \theta}{M_2 + M_1} \right]^2$$

where the masses of the incident ion and target atoms are given by M_1 and M_2 , respectively. The area density (Nt), in atoms per unit area, may be determined for a given element from a knowledge of the detector solid angle Ω , the integrated peak count A for Q incident ions, and the calculated cross section $\sigma(E, \theta)$.

For the energies used in our measurements, the scattering is purely coulomb repulsion; then σ may be obtain from:

$$\sigma(E, \theta) = \left(\frac{Z_1 Z_2 e^2}{4E} \right)^2 \times 4 \frac{\left[(M_2^2 - M_1^2 \sin^2 \theta)^{\frac{1}{2}} + M_2 \cos \theta \right]}{M_2 \sin^4 \theta (M_2^2 - M_1^2 \sin^2 \theta)^{\frac{1}{2}}}$$

In order to utilize the depth profiling capabilities of backscattering, it is necessary to relate the energy of the scattered particle to the depth in the sample where the scattering event occurred. This, as in ion implantation, depends on the energy loss of the ion traversing the sample, the kinematic factor for the scattering, and the sample orientation. The difference in energy at the detector for a particle scattered at the surface and a particle scattered at a depth x , measured perpendicular to the sample is given by:

$$\Delta E = [\varepsilon] N x$$

where N is the atomic density of the substrate. $[\varepsilon]$ is called the stopping cross section factor and it is defined by:

$$[\varepsilon] = \left[K \varepsilon_{in} \frac{1}{\cos \theta_1} + \varepsilon_{out} \frac{1}{\cos \theta_2} \right]$$

where the ϵ_i are the stopping cross sections, defined as the energy loss/atom/cm² of material traversed. Since these parameters are energy dependent, a surface energy approximation was used to evaluate them. ϵ_{in} was evaluated at the incident energy and ϵ_{out} was evaluated at KE₀. RBS, in general, allowed us to verify the stoichiometry, purity and evaluate the thickness of the sputtered films using RUMP software [26].

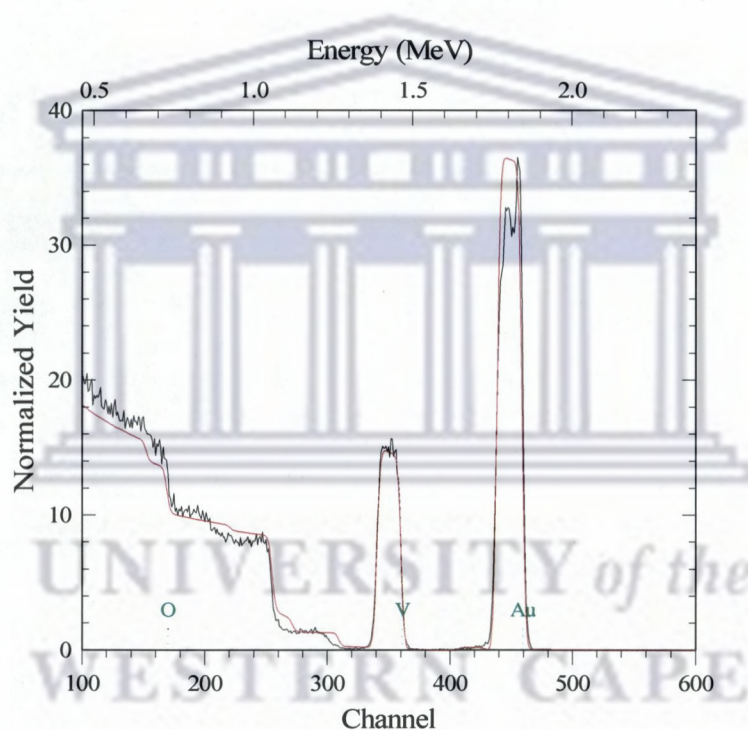


Figure 3.12: The RBS spectrum of Au-VO₂ deposited on corning glass substrate at 450 °C by ICMS. The solid line through the data is the fit to the spectrum using RUMP software.

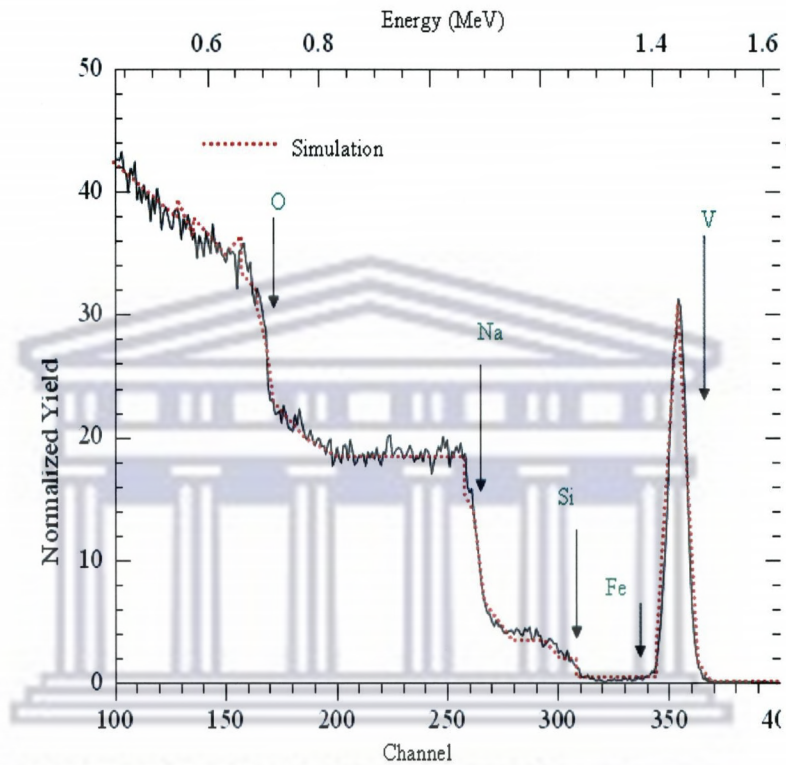


Figure 3.13: The RBS spectrum of pure VO₂ thin film deposited on Soda lime glass substrate at 450 °C by ICMS. The solid line through the data is the fit to the spectrum using RUMP software.

3.5.9.2 Equipment used

A 6 MV Van de Graaf ion accelerator located at ithemba LABS-South Africa was used to carry out the Rutherford Backscattering Spectrometry.

3.6. References

- [1] O. Durand-Drouhin, Ph.D. Thesis University of Amiens, France 2001.
- [2] P. Sigmound, sputtering by particle bombardment, Springer-Verlag, New-York, 1981.
- [3] B. Mebarki, Ph.D. Thesis University of Toulouse, France 1997.
- [4] D.L.Smith, Thin film Deposition: Principles and Practice, McGraw-Hill, Inc. 1995.
- [5] R. Wendt and K. Ellmer. Surf. Coating Technol; 93 (1997) 27.
- [6] A.S. Penfold, J.A.Thornton, U.S. Patents #3,884, (1975)793.
- [7] J.A.Thornton, A.S.Penfold,in:J.L.Vossen, W.Kern(Eds),Thin Films Processes, Academic Press, New York, 1978, p.76
- [8] J.B. Kana Kana, J.M. Ndjaka, P. Owono Ateba, B.D. Ngom, N. Manyala, O. Nemraoui, A.C. Beye and M. Maaza, Appl. Surf. Sci. 254, (2008) 3959.
- [9] Q. Zhong, D. Innis, K. Kjoller, and V. Elings, Surf. Sci. Lett. 290 (1993) L688.
- [10] D. Scaini, Ph.D. Thesis University of Trieste-Italy (2008).
- [11] P. Klapetek, Ph.D. Thesis, MASARYK UNIVERSITY BRNO, (2003).
- [12] Kun Lin, Hang Zhang, Shey-shi Lu Proceedings of the 32nd International Symposium for Testing and Failure Analysis November 12-16, 2006, Renaissance Austin Hotel, Austin, Texas, USA.
- [13] G. Binnig, H. Rohrer, Ch. Gerber, E. Weibel, Phys. Rev. Lett. 49 (1982) 57.
- [14] R. Sonnenfeld and P.K. Hansma, Science 232 (1986) 211.
- [15] D.P. Woodruff and T.A. Delchar, Modern techniques of surface science, 2nd ed. Cambridge university press, 1994.
- [16] C.J. Chen, Introduction to Scanning Tunneling Microscopy, Oxford University Press, New York, (1993).
- [17] C. Bai, Scanning Tunneling Microscopy and its Application, Springer Verlag, Berlin, (1992).

- [18] <http://www.scienceofspectroscopy.info>.
- [19] W. Van den Hoogendorf and D.K.G. de Boer, *Surf. Interface Anal.*, 22 (1994) 169.
- [20] D. Bowen and M. Wormington, *Adv. X-Ray Anal.*, 36 (1993) 171.
- [21] M. Deutsch and B.M. Ocko, *Encycl. Appl. Phys.* 23 (1998) 479.
- [22] A. Gibaud and S. Hazra, *Current Science* 78 (2000) 1467.
- [23] B.D. Cullity, *Elements of X-ray diffraction*, 2eme Ed., Addison-Wesley, Reading, Mass. (1978) p102.
- [24] *Handbook of ellipsometry*, Edited by Harland G. Tompkins and Eugene A. Irene, ISBN:9780815514992 (2009).
- [25] J.A. Leavitt, J.L.C. McIntre, and M.R. Weller, in *Handbook of Modern Ion Beam Material Analysis*, MRS, Pittsburgh (1995).
- [26] L. Doolittle, *Nucl. Instrum. Meth. B* 9, 334 (1985).



UNIVERSITY *of the*
WESTERN CAPE

Chapter 4

THICKNESS INDUCED DRASTIC REDUCTION OF PHASE TRANSITION TEMPERATURE IN SPUTTERED VO₂ THIN FILMS

Abstract

VO₂ thin films were deposited on Corning glass substrates by reactive radiofrequency inverted cylindrical magnetron sputtering. The effect of thickness on the switching properties of VO₂ thin films was investigated. Thickness significantly alters sharpness of semiconductor-metal phase transition and drastically reduces the transition temperature (T_c). The T_c considerably decreases from 70 °C to 50 °C as thickness increases from 60 nm to 200 nm. Implications of these results on the possible reasons responsible for the T_c reduction are discussed.

4.1. Introduction

Vanadium dioxide (VO_2), as a well-known transition metal oxide material, has attracted considerable attention in recent years because of its excellent ultrafast switching properties [1,2], electrochromic and thermochromic properties [3], photocatalytic properties for hydrogen production [4] and its possibility to tune reversibly the plasmon resonance of noble metal nanoparticles [5-7], etc. This material exhibits a reversible first-order phase transition from monoclinic ($P2_1/c$) to a tetragonal (rutile $P4_2/mnm$) crystalline structure at a transition temperature (T_c) of 68 °C [8], accompanied by large changes in its electrical conductivity and infrared transmission characteristics [9-11].

The existence of many competing vanadium oxides such as VO , V_6O_{13} , V_7O_{13} , V_2O_5 , V_2O_3 etc offers a particular challenge to the growth of high-purity VO_2 thin films. Several film physical vapour deposition methods have been employed to grow VO_2 thin films, such as pulsed laser ablation [12-13], reactive radiofrequency and direct current magnetron sputtering [14-15], radiofrequency inverted cylindrical magnetron sputtering [16] and so on. However, numerous growth conditions, such as O_2 partial pressure [17], ambient atmosphere [18], low thickness [19], substrate temperature [20], and substrate's nature [21] were found to highly influence the T_c of the VO_2 growing film.

This chapter deals with the effect of thickness (d) on the phase transition temperature of VO_2 thin films grown by radiofrequency inverted cylindrical magnetron sputtering. It was found that the semiconductor-metal phase transition temperature considerably decreases from 70 °C to 50 °C as thickness increases from 60 nm to 200 nm. The most probably mechanisms responsible for the T_c reduction are discussed. In addition, we report the blue shift of absorption edges (at around 500 nm) as thickness decreases.

4.2. Experimental details

4.2.1. Sample preparation

VO₂ thin films were deposited with a radiofrequency inverted cylindrical magnetron sputtering that has been described previously [16] from a hollow cylindrical vanadium metal 99.98 % purity target. The chamber was initially evacuated to about 10⁻⁴ Pa by a diffusion pump backed by a rotary pump. During the sputtering experiment, the pressure of 0.8 Pa of the mixture of 10 % of oxygen in argon followed by 1 Pa of high purity (99.99 %) argon was carefully introduced into the chamber. The gas pressure aforementioned was found to be an optimal pressure for the synthesis of high quality of VO₂ in our previous work [16]. A pre-sputtering time of 15 min was used to remove surface contamination and oxides on the target and to ensure stabilized sputtering conditions. The film deposition was carried out at a fixed substrate temperature of 450 °C. Corning glass ultrasonically cleaned was used as substrates. By varying the radiofrequency power, the thicknesses of the prepared films were 60, 90, 130, 200 nm.

4.2.2. Sample characterization

The simulation of X-ray reflectivity profiles was used to measure the thickness of the films. The optical properties of the VO₂ films were measured in the wavelength range 350–1100 nm using a CECIL 2000 Spectrophotometer incorporated with Peltier thermoelectric heating and cooling stage.

4.3. Results and discussion

4.3.1. Optical transmittance

Fig. 4.1 shows the transmittance spectra of VO₂ films sputtered at different d . These measurements were carried out both at room temperature (semiconductor state) and at a temperature of 85 °C (metal state). As expected, all the films in the semiconductor phase exhibit much higher Visible-Infrared (Vis-IR) transmittance than those in the metal phase. In addition, the spectral transmittances of the semiconducting phase and

metal phase are sharply contrasting in the infrared region, proving good thermochromism. From Fig. 4.1, it can be clearly seen that the transmittance of both phases in the Vis-IR region significantly reduced as d increases. Thicknesses seem to influence the visible transmittances of these films effectively without deterioration of the infrared regulation ability. The films with thickness of 200 nm exhibit lower transmittance (semiconducting phase) of about 10% at $\lambda = 650$ nm compared with the transmittance (semiconducting phase) of 38% for those having a thickness of 60 nm. Furthermore, an interesting phenomenon has been observed. As thickness decreases, the blue shift of absorption edges (at around 500 nm) is well observed. Similar phenomenon has been observed by Kang et al.[23].

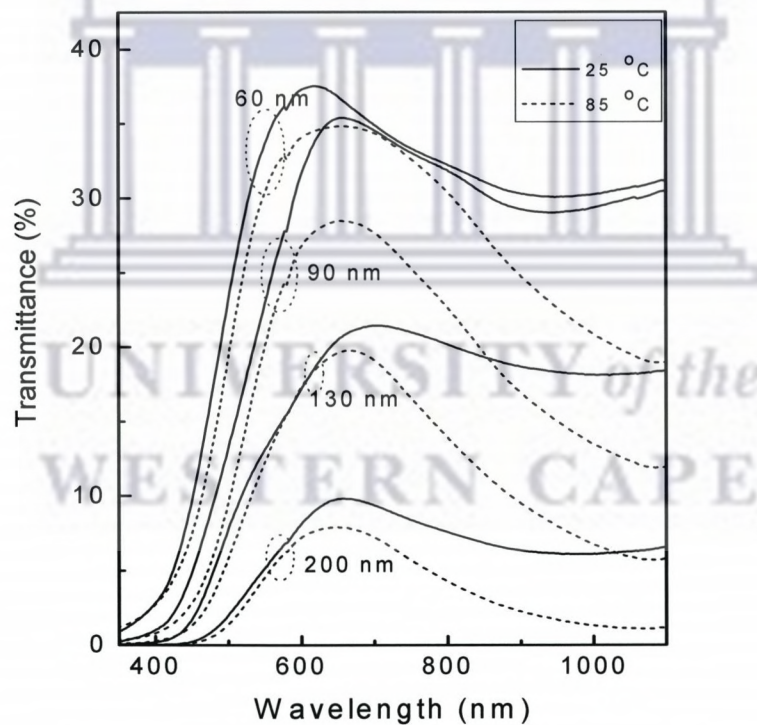


Figure 4.1: Spectral transmittance for the semiconductor phase measured at 20 °C (solid line) and metal phase at 85 °C (dashed line) of VO₂ thin films deposited at different thicknesses.

4.3.2 Thermal hysteresis and phase transition temperature

To probe the effects of d on the switching characteristics of the VO_2 films, the optical transmittance measurements were carried out as a function of external temperature stimuli. Fig. 4.2 shows the thermal hysteresis loops of the optical transmittance at a fixed wavelength of 1100 nm for VO_2 thin films sputtered at different thicknesses and serves to distinguish the shift in transition temperature. Fig. 4.2 clearly illustrates the drastic change in transmittance as the film is cycled through the transition region. The solid curves correspond to the heating run, whereas the dashed curves correspond to the cooling run. To evaluate the semiconductor-metal phase transition (SMT) characteristics of the films, the derivative of the transmittance hysteresis of the heating curve has been calculated. The transition temperature (T_c) is defined as the maximum of the derivative curve, while the hysteresis width is defined as the difference between the T_c of the heating and cooling curves. The sharpness of the SMT is characterized by the full width at half-maximum of the derivative curve as suggested by Brassard et al. [24]. It is evident from Fig. 4.2 that d has a significant influence on the sharpness, shapes of the hysteresis and hysteresis width. It can be seen that the magnitude of the hysteresis loop is significantly depressed as d increases, and the higher d , the more depressed the loops. The hysteresis width decreases from 10 to 5 °C when the thickness increases from 60 to 200 nm. The T_c decreases from 70 °C to 50 °C when d varies from 60 nm to 200 nm. Even if the variation of the T_c of VO_2 is not dramatic "variation from 70 °C to 50 °C" with increasing d is substantial for undoped VO_2 thin films. This sizeable variation of ~ 20 °C confirms the significant influence of thickness on the T_c of VO_2 thin films. The corresponding values of T_c and hysteresis width for each film thickness are tabulated in Table 4.1. We suggest at least the followings most probably responsible for the T_c reduction. First, a slight deviation from stoichiometry, either under- or overstoichiometry, is known to reduce T_c [17]. Second, the crystallinity of the films hence an increased crystal imperfection, e.g., an increased

number of atoms distributed randomly at grain boundaries due to small crystallite size and / or a large surface / interface ratio for thin VO₂ films, may damage the zigzag chains of the V-V pairs characteristic of the low temperature phase, resulting in the destabilization of the low temperature phase and therefore the decrease of T_c [22].

d(nm)	T _c (°C)	Hysteresis width (°C)
60	70	10
90	65	12
130	55	8
200	50	5

Table 4.1: Values for the transition temperature and hysteresis width for each film thickness.

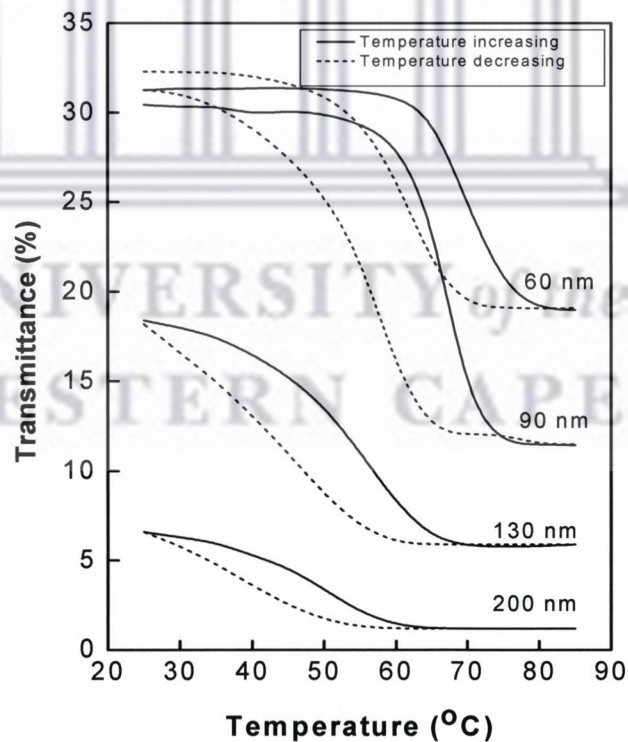



Figure 4.2: Thermal hysteresis loops of transmittance at wavelength of 1100 nm for VO₂ thin films deposited at different thicknesses.

4.4. Conclusion

We have fabricated VO₂ thin films on Corning glass substrates by radiofrequency inverted cylindrical magnetron sputtering. The effects of film thickness on switching properties were investigated in a large range of film thickness. The transition temperature was found to be reduced with increasing film thickness. By adjusting the film thickness, it is possible to control and tailor the semiconductor-metal phase transition temperature of VO₂ films.

4.5. References

- 
- [1] A. Cavalleri, Cs. Toth, CW. Siders, JA Squier, F. Raksi, P. Forget, and JC Kieffer Phys. Rev. Lett. 87, (2001) 237401.
- [2] A. Cavalleri, T. Dekorsy, HHW Chong, JC Kieffer and RW Schoenlein Phys. Rev. B 70, (2004) 161102.
- [3] MSR Khan, KA Khan, W. Estrada and C.G.Granqvist J. Appl. Phys. 69(5), (1991) 3231.
- [4] Y. Wang, Z. Zhang, Y. Zhu, Z. Li, R. Vajtai, L. Ci and P.M. Ajayan ACS NANO 2, (2008)1492.
- [5] M. Maaza, O. Nemraoui, C. Sella, AC Beye and B. Baruch-Barack Opt. Commun. 254, (2005) 188.
- [6] G. Xu, Y. Chen, M. Tazawa and P. Jin, J. Phys. Chem. B 110, (2006) 2051
- [7] J.B. Kana Kana, JM Ndjaka, M. Manyala, O. Nemraoui, AC Beye and M. Maaza AIP Conference Proceedings 1047, (2008) 119.
- [8] F.J. Morin Phys. Rev. Lett. 3, (1959) 34.
- [9] J.F. De Natale, P.J. Hood and A.B. Harker, J.Appl.Phys. 66, (1989) 5844.

- [10] H.W. Verleur, A.S. Barker Jr. and C.N. Berglund, *Phys. Rev.* 172, (1978) 788.
- [11] A.S. Barker, H.W. Verleur and H.J. Guggenheim, *Phys. Rev. Lett.* 17, (1966) 1286.
- [12] D.H. Kim and H.S. Kwok, *Appl. Phys. Lett.* 65, (1994) 3188.
- [13] M. Maaza, K. Bouziane, J. Maritz, D.S. McLachlan, R. Swanepool and J.M. Frigerio, M. Every, *Opt. Mater.* 15, (2000) 41.
- [14] J. Duchene, M. Terrail and M. Pailly, *Thin Solid Films* 12, (1972) 231.
- [15] F. Guinneton, J.C. Valmalette and J.R. Gavarri, *Opt. Mater.* 15,(2000)111.
- [16] J.B. Kana Kana, J.M. Ndjaka, P. Owono Ateba, B.D.Ngom, N. Manyala, O. Nemraoui, A.C. Beye and M. Maaza, *Appl. Surf. Sci.* 254, (2008)3959.
- [17] C.H. Griffiths and H.K. Eastwood, *J. Appl. Phys.* 45, (1974) 2201.
- [18] K. Nagashima, T. Yanagida, H. Tanaka and T. Kawai, *J. Appl. Phys.* 100, (2006) 063714.
- [19] G. Xu, P. Jin, M. Tazawa and K. Yoshimura, *Appl. Surf. Sci.* 244, (2005) 449.
- [20] E.E. Chain, *J. Vac. Sci. Technol. A* 4, (1986) 432.
- [21] F.C. Case, *J. Vac. Sci. Technol. A* 2, (1984) 1509.
- [22] A. Begishev, G. Gliiev, Ignat'ev, V. Mokerov and V. Poshin, *Sov. Phys. Solid State* 20, (1978) 951.
- [23] L. Kang, Y. Gao, Z. Zhang, J. Du, C. Cao, Z. Chen and H. Luo, *J. Phys. Chem. C* 114 (4), (2010) 1901.
- [24] D. Brassard, S. Fourmaux, M. Jean Jacques, J.C. Kieffer, and M. A. El Khakani, *Appl. Phys. Lett.* 87, (2005) 051910.

Chapter 5

HIGH SUBSTRATE TEMPERATURE INDUCED ANOMALOUS PHASE TRANSITION TEMPERATURE SHIFT IN SPUTTERED VO₂

Abstract

Vanadium dioxide (VO₂) thin films were deposited onto Corning glass substrates by radiofrequency inverted cylindrical magnetron sputtering at different substrate temperatures (T_s) ranging from 450 °C to 600 °C. The influence of substrate temperature on the morphological, structural and optical properties was systematically investigated. It revealed that the surface morphology as well as the crystallinity of the VO₂ films changed significantly with T_s . The substrate temperature to obtain films with transition temperature ($T_c \sim 70$ °C) similar to VO₂ bulk single crystal was 450-500 °C, while high substrate temperatures from 550 to 600 °C tend to shift T_c towards higher temperatures from 75 to 80 °C keeping the sharpness of the transition unaltered. Even if the variation of the T_c of VO₂ is not dramatic "variation from 70 °C to 80 °C" with increasing T_s is substantial for undoped VO₂ thin films. This sizeable variation of ~ 10 °C confirms the tunability of the T_c of VO₂ through T_s .

The content of this chapter has been published in Optical Materials 32 (2010) 739-742.

5.1. Introduction

Vanadium dioxide (VO_2) is well known to exhibit a reversible first-order phase transition from monoclinic ($P2_1/c$) to a tetragonal (rutile $P4_2/mnm$) crystalline structure at a transition temperature (T_c) of 68 °C [1]. This phase transition is accompanied by a significant change in the electrical resistivity and optical properties in the infrared region [2,3]. These features make VO_2 films suitable for many technological applications such as thermal sensing and switching devices [4], optical and electrical devices [5], thermochromic smart windows [6,7] and reversible tunable surface plasmon resonance for applied plasmonics [8-10].

The semiconductor-metal phase transition (SMT) characteristics vary strongly according to the synthesis conditions of single crystals and thin films. It was reported that the VO_2 single crystals have stronger abruptness of electrical resistance and optical transmittance, narrower hysteresis width of 1-2 °C [2] and a transition temperature of 66-68 °C [11], while polycrystalline VO_2 thin films tend to have smaller abruptness of optical transmittance, wider hysteresis width of 10-15 °C [12]; in nanoparticulate VO_2 , the hysteresis widths may be even larger [13].

Various chemical and physical methods have been employed for the deposition of VO_2 thin films with specific optical and /or electrical properties in an effort to monitor the transition temperature. The fact that the transition characteristics of the VO_2 such as transition temperature, hysteresis width, and sharpness of the semiconductor-metal transition are very sensitive to the deposition parameters pose a challenge to the monitoring of these characteristics. The controllability of the transition temperature, hysteresis width and sharpness of the transition which are indicators of the VO_2 films quality by adjusting the deposition parameters, is highly desirable for the expansion of VO_2 based devices and sensors. To date, there are a number of studies dealing with the modification of the transition temperature of VO_2 thin films. For example, Muraoka et al. [14] reported the effect of uniaxial stress along the c-axis on the metal-insulator

transition implying a large reduction of the T_c from 68 °C to 27 °C. Soltani et al. [4] reported the doping effect and found that the T_c was about 22.85 °C per 1 at. % of W added. In the same trend, Takahashi et al. [15] demonstrated a thermochromic switching performance of double doped films in the $V_{1-x-y}W_xMo_yO_2$ and $V_{1-x-z}W_xTi_zO_2$ systems and established a clear relationship between transition temperature, width of hysteresis loop and doping level of these systems. Moreover, Xu et al. [16] investigated the effects of thickness ranging from 3 to 150 nm on optical properties and showed that the T_c is suppressed with decreasing film thickness. Furthermore, Miyazaki et al. [17] investigated the substrate bias and buffer layer effects on the growth of VO_2 thin films and showed that the T_c is strongly dependent on these parameters. The ion bombardment effect during the VO_2 films deposition, investigated by Li et al. [18], was found to decrease drastically the T_c to 33 °C. The substrate temperature ranging from 224 to 477 °C effects on the metal-insulator characteristics of strained VO_2 were investigated by Nagashima et al. [19]. They demonstrated that it is possible to reduce T_c without altering the abruptness of the transition.

To our knowledge, the influence of substrate temperature on the structural, electrical and optical properties has been sparsely explored by some reports. Razavi et al. [20] reported the temperature effects on structure and optical properties of sputter VO_2 deposited on random sapphire substrates at temperatures ranging from 300 to 500 °C. Mlyuka and Kivaisi [21] established a correlation between structural and optical properties of VO_2 thin films deposited on glass substrates at temperatures ranging from 250 to 400 °C. West et al. [22] reported the influence of substrate temperature ranging from 250 to 550 °C on the growth of VO_2 on Al_2O_3 (0001) by a novel technique called reactive bias target ion beam and proved that the metal-insulator transition temperature can be tuned to higher temperatures by mixing VO_2 and other vanadium oxides phases.

Although different effects of deposition parameters on the semiconductor-metal phase transition temperature of VO₂ thin films have been reported extensively, to our knowledge, a tunability of the transition temperature of undoped VO₂ towards higher temperatures with substrate temperature has not been reported yet.

In this chapter, we report the anomalous shift of phase transition temperature induced by high substrate temperatures of sputtered VO₂ thin films. We find that the phase transition temperature increases with increasing substrate temperature. A sizeable variation of ~ 10 °C with increasing substrate temperature (T_s) was observed. The influence of T_s on surface-morphology and structural properties of the synthesized films is also reported.

5.2. Experimental Details

5.2.1. Sample Preparation

Single stoichiometric phase polycrystalline VO₂ thin films were deposited by radiofrequency inverted cylindrical magnetron sputtering (ICMS) that has been described previously [23] from a hollow cylindrical vanadium metal 99.98% purity target. The chamber was initially evacuated to about 5×10^{-4} Pa by a diffusion pump backed by a rotary pump. During each sputtering experiment, the pressure of 0.8 Pa of the mixture of 10% of oxygen in argon followed by 1 Pa of high purity (99.99%) argon was carefully introduced into the chamber. The gas pressure in the chamber was monitored by both Penning and Pirani vacuum gauges mounted into the chamber wall. The gas pressure aforementioned was found to be an optimal pressure for the synthesis of high quality VO₂ in our previous work [23]. A pre-sputtering time of 15 min was used to remove surface contamination and oxides on the target and to ensure stabilized sputtering conditions. Sputtering was carried out at an rf power of 70 W and an optimal working gas pressure mentioned above. To study the effect of substrate temperatures (T_s) on the physical properties of the films, T_s was varied from 450 to 600 °C. Corning glass substrates ultrasonically cleaned were used as substrates. The

prepared films have almost the same thickness of 50 ± 2 nm at the central spot of the substrate, which was achieved by adjusting the appropriate deposition time.

5.2.2. Sample Characterization

The simulation of X-ray reflectivity profiles was used to measure the thickness of the films. The crystal structure was characterized by X-ray diffraction (XRD) using $\text{CuK}\alpha$ radiation (model Bruker AXS D8 Advance). The surface roughness was characterized by Atomic Force Microscopy (AFM) using Nanoscope III, a Digital instrument operated in tapping mode. The optical properties of the films were measured in the wavelength range of 350–1100 nm using a CECIL 2000 Spectrophotometer incorporated with Peltier thermoelectric heating and cooling stage.

5.3. Results and discussion

5.3.1. Structural Properties

Figure 5.1 shows the XRD pattern of the VO_2 thin films deposited at low and high substrate temperatures of 450 and 600 °C respectively. The sputter-deposited films exhibit a polycrystalline structure that matches that of single phase monoclinic VO_2 (JCPDS43-1051) without showing an indication of any other vanadium oxides phases.

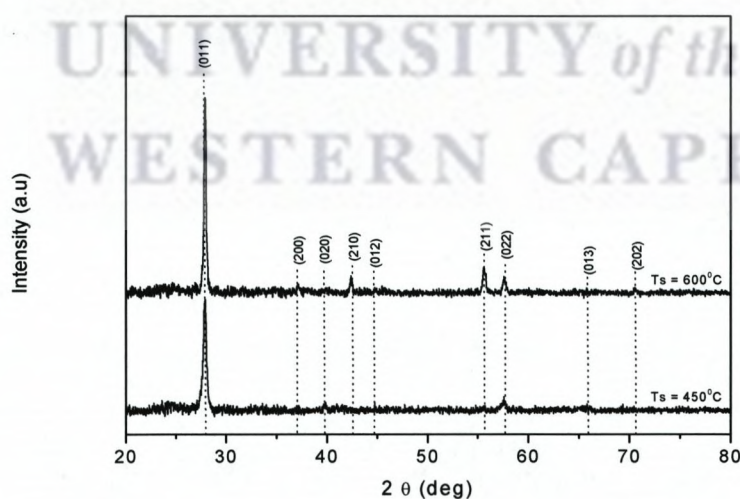


Figure 5.1: Indexed XRD spectra of VO_2 monoclinic (JCPDS 43-1051) films deposited on normal microscope glass substrate at substrate temperatures (T_s) of 450 and 600 °C.

The XRD pattern of the 600 °C deposited films clearly shows an increase in peak intensity of the (011) peak. The increase in intensity and the decrease in the full width at half maximum (FWHM) of the (011) peak may be attributed to improvement of crystallinity with substrate temperature. Using Scherrer's formula [24], the grain size of the films was calculated using the strongest (011) peak because (001) peak is the strongest peak of monoclinic VO₂. The results of the calculation gave 20, 25, 30 and 32 nm for substrate temperature of 450, 500, 550 and 600 °C respectively. It can be seen that, the grain size of VO₂ films increases with increase in T_s. This increase in grain size at higher substrate temperatures is consistent with Chain's work on ion beam deposited Vanadium oxide [25].

5.3.2. Surface-morphological properties

AFM images of VO₂ thin films were taken to evaluate the dependence of surface roughness on substrate temperature. Figure 5.2a-b shows AFM images of VO₂ thin films sputtered at substrate temperatures of 450 and 600 °C. From the 2-D images, it can be seen that surface morphologies of the VO₂ thin films sputtered on glass substrates is significantly temperature dependent. From the AFM images, it is clearly seen that the films sputtered at 450 °C are composed of small crystallites while those sputtered at 600 °C show large crystallites. There is therefore a significant evolution of crystallites with increasing substrate temperature, leading to rougher surface. The root mean square (Rms) roughness was evaluated from AFM measurement using Nanoscope software. It was found that the RMS roughness of the 450 and 600 °C deposited films were 5.61 nm and 8.36 nm respectively. The roughness of films sputtered at 500 and 550 °C was 6.25 and 7.30 nm respectively (corresponding AFM images not shown). This is quite a high roughness as compared to the total thickness of the films which is 50 nm. Since this roughness impacts about 20 % of the film, the roughness might contribute to the overall optical properties. It is well reported that

inhomogeneities in thin films have a large influence on the optical transmission spectrum [29].

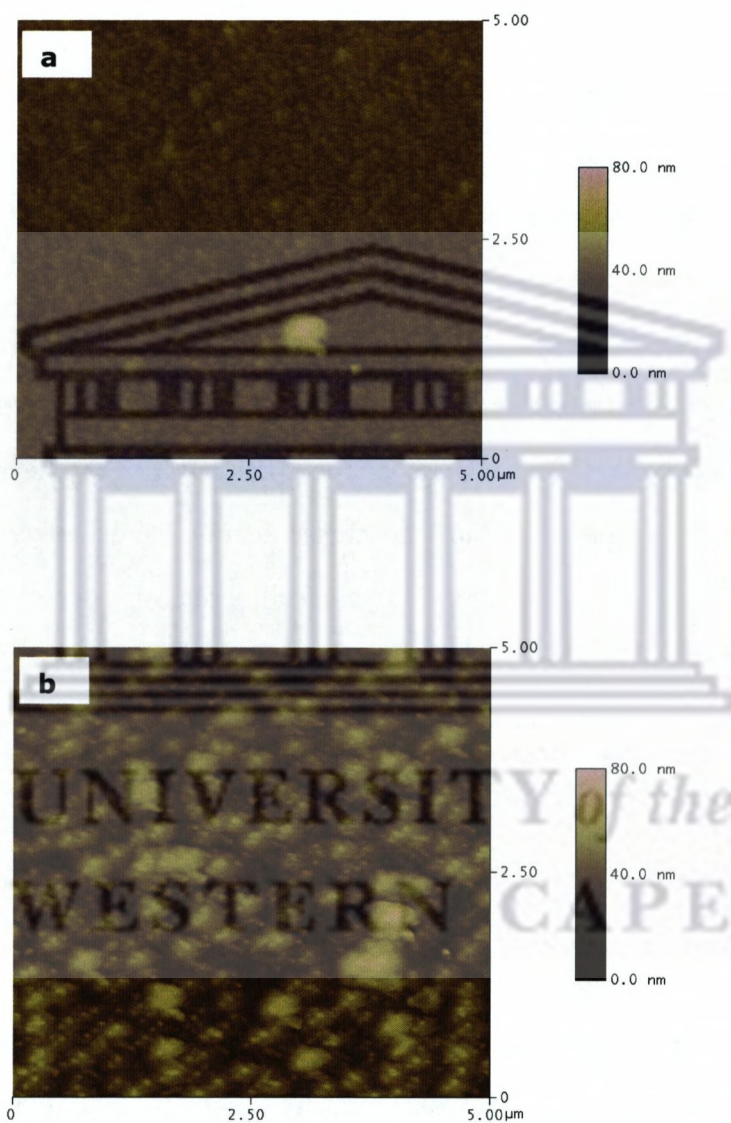


Figure 5.2: Atomic force microscopy (AFM) images of 5x5 μm² area of VO₂ thin film surface prepared at 450 °C (a) and 600 °C (b).

5.3.3. Optical properties

5.3.3.1. Optical transmittance

Figure 5.3 shows the spectral transmittance of VO₂ thin films sputtered at different substrate temperatures ranging from 450 to 600 °C. The measurements were carried out both at room temperature (semiconductor state) and at a temperature of 100 °C (metal state). The observed results show an extremely interesting behaviour in the visible region. The transmittance of the semiconductor phase is lower than that of the metal phase. This transmittance difference between the two phases is thickness dependent as suggested Xu et al. [16]. It was shown that for VO₂ films with thicknesses less or equal than 50 nm, the semiconductor phase exhibits lower visible transmittance than its metallic phase. It can be seen that the higher the substrate temperature, the smaller the change of the transmittance in the visible light region between the two phases. The films sputtered at 600 °C exhibit lower transmittance (metal phase) of about 35% at $\lambda=700$ nm compared with the transmittance (metal phase) of 45% for those sputtered at 450, 500 and 550 °C. This change in transmittance at substrate temperature of 600 °C can be explained by the fact that high temperature influences the sticking factor of the sputtered particles to the substrate surface, implying a slight increase of the deposition rate. Apart from this surprising behaviour observed in the visible range, the two states are sharply contrasting in the near infrared region.

5.3.3.2. Thermal hysteresis

To probe the effects of deposition temperature on the switching characteristics of the films, the transmittance measurements were carried out as a function of external temperature stimuli. Figure 5.4 shows the thermal hysteresis loops of the optical transmittance at a fixed wavelength of 1100 nm for VO₂ thin films sputtered at different temperatures. The figure clearly illustrates the drastic change in transmittance as the film is cycled through the transition region. The solid curves

correspond to the heating run, whereas the dashed curves correspond to the cooling run. To evaluate the semiconductor-metal phase transition characteristics of the films, the derivative of the transmittance hysteresis of the heating curve has been calculated. The transition temperature (T_c) is defined as the maximum of the derivative curve, while the hysteresis width is defined as the difference between the T_c of the heating and cooling curves. The sharpness of the SMT is characterized by the full width at half-maximum of the derivative curve as suggested by Brassard et al. [12]. Regardless of the substrate temperature, all the sputtered films show the same hysteresis loops and sharp transition.

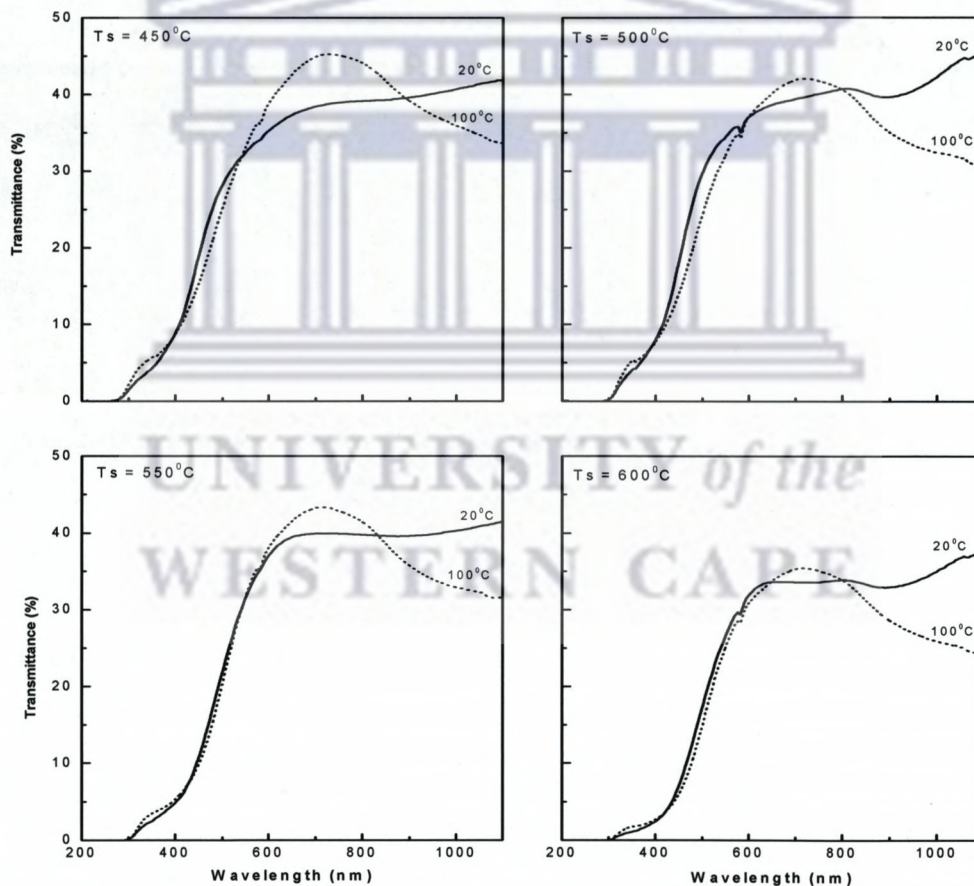


Figure 5.3: Spectral transmittance for the semiconductor phase measured at 20 °C (solid line) and metal phase at 100 °C (dashed line) of VO₂ thin films deposited at different substrate temperatures.

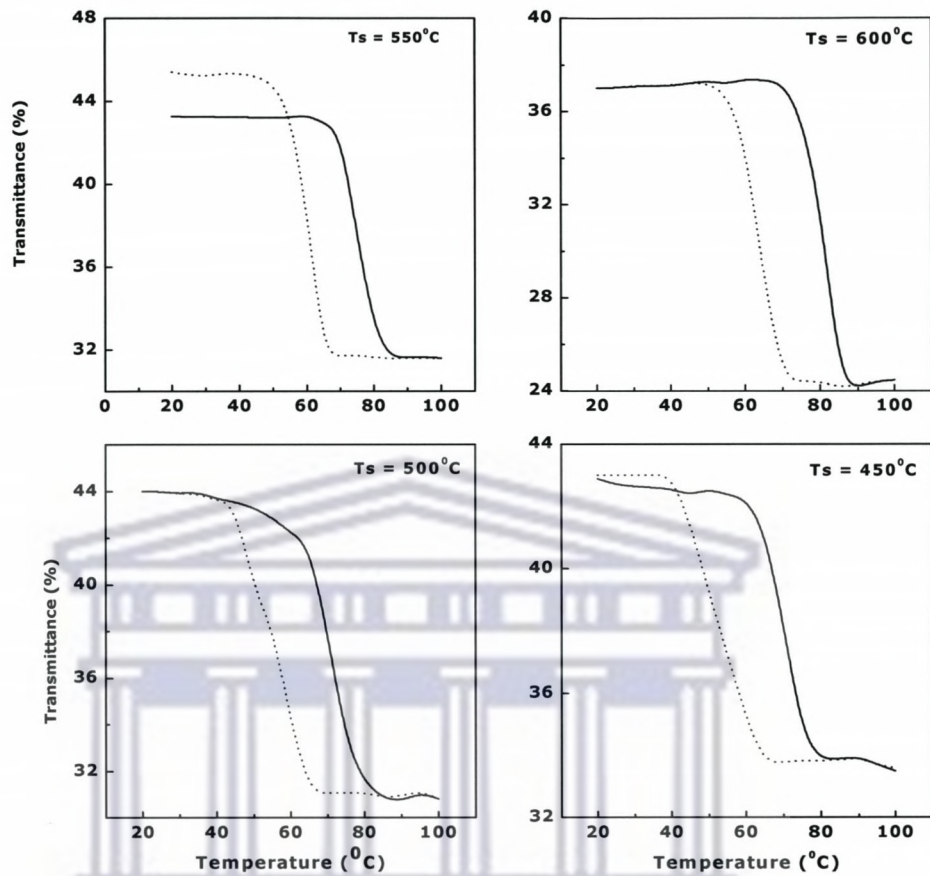


Figure 5.4: Thermal hysteresis loops of transmittance at wavelength of 1100 nm for VO₂ thin films deposited at different substrate temperatures ranging from 450 to 600 °C. The solid line represents the heating run while the dashed line represents the cooling.

5.3.3.3. Tunability of the phase transition temperature

Figure 5.5 shows the dependence of T_c and hysteresis width on substrate temperature. From the figure, it can be seen that T_c increases from 70 °C to 80 °C when T_s varies from 450 °C to 600 °C. The substrate temperature range of 450-500 °C led to T_c = 70 °C similar to bulk single crystal while high substrate temperatures from 550 - 600 °C led to T_c of 75 and 80 °C respectively. This result can be explained by the fact that, the

superheating of VO₂ films sputtered at substrate temperature of 600 °C induces the semiconductor-metal (S-M or M-S) transition to occur first in preferable nucleation sites, and then these nuclei propagate through grain boundaries, as observed by Frenzel et al.[30]. The propagation of the S-M transition through grain boundaries promotes the phase transition of connected grains at relatively low driving forces, resulting in a significant shift of T_c to the thermodynamic equilibrium temperature (~70 °C). Similar significant shift of T_c towards higher temperature of 81.8 °C has been observed by Kang et al. [31] by annealing VO₂ films on fused silica prepared via a simple solution process with inorganic precursors and polyvinylpyrrolidone (PVP) at annealing conditions (temperature of 600 °C, time 60 min).

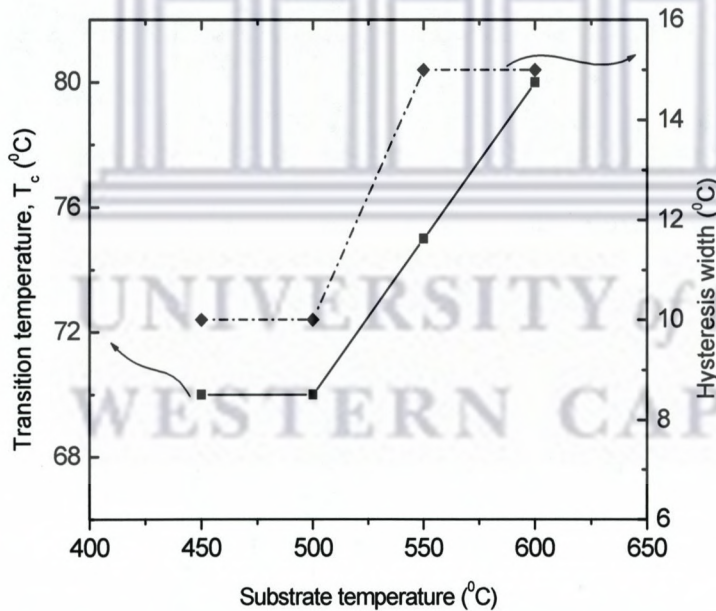


Figure 5.5: Variation of the transition temperature and hysteresis width of VO₂ film as a function of substrate temperature. It shows the possibility to tailor the semiconductor-metal phase transition by adjusting the substrate temperature.

The microstructure might also be responsible for such elevated phase transition temperature of VO₂ thin films. Hence it is demonstrated by Kang et al. [31] that the microstructure (grain boundaries, grain sizes, and size distributions) of VO₂ films has significant effects on the features of the semiconductor–metal transition. The width and sharpness of the hysteresis loops (i.e., the temperature sensitivity of the transition) can be regulated by controlling grain sizes and grain boundary conditions, which are believed to dominate the generation of the elementary hysteresis loop of each grain and the propagation of the S–M transition, respectively. However, the main factors affecting the semiconductor-metal transition are crystallinity, grain size and grain boundaries [32]. The diffusion of very low amount of some elements such as Al, Na or Ca from the Corning glass substrate or a slight deviation of the stoichiometry of the films at elevated substrate temperature would be also responsible for this anomalous shift of T_c towards higher temperatures. The hysteresis width of all the deposited films increases from 10 to 15 °C when the substrate temperature increases from 450 to 600 °C. This is consistent with those reported for reactively sputtered VO₂ continuous polycrystalline thin films [12, 28].

5.4. Conclusion

VO₂ thin films were fabricated on Corning glass substrate by radiofrequency inverted cylindrical magnetron sputtering. The effects of substrate temperature on optical, structural properties and surface morphology were investigated in a large range of substrate temperature. The semiconductor-metal phase transition temperature was found to be increased with increasing substrate temperature. A shift of ~ 10 °C towards higher temperature for undoped VO₂ films was found. Also it was showed that the crystallinity of the films and the surface morphology are substrate temperature dependent.

5.5. References

- [1] F.J. Morin, Phys. Rev. Lett. 3, (1959) 34.
- [2] J.F. De Natale, P.J. Hood, and A.B. Harker, J. Appl. Phys. 66, (1989) 5844.
- [3] H.W. Verleur, A.S. Barker Jr., C.N. Berglund, Phys. Rev. 172, (1978) 788.
- [4] M. Soltani, M. Chaker, E. Haddad, R.V. Kruzelecky, D. Nikampour, J. Vac. Sci and Technol. A: Vac. Surf. Films, 22, (2004) 859.
- [5] B.J. Kim, Y.W. Lee, B.G. Chae, S.J. Yun, S.Y. Oh, H.T. Kim, arXiv: Cond-mat/0609033 V1 (2006).
- [6] G. Xu, P. Jin, M. Tazawa, and K. Yoshimura, Sol. Energy Mater. Sol Cells 83, (2004) 29.
- [7] S.M. Babulanam, T.S. Eriksson, G.A. Niklasson, and C.G. Granqvist, Sol. Energy Mater. 16, (1987) 347.
- [8] M. Maaza, O. Nemraoui, C. Sella, A.C. Beye, B. Baruch-Barack, Opt. Commun. 254, (2005) 188.
- [9] G. Xu, Y. Chen, M. Tazawa, P. Jin, J. Phys. Chem. B 110 (2006) 2051.
- [10] J.B. Kana Kana, J.M. Ndjaka, M. Manyala, N. Nemraoui, O. Nemraoui, A.C. Beye, M. Maaza, AIP Conference Proceedings, 1047, (2008) 119.
- [11] L.A. Ladd and W. Paul, Solid State Commun. 7, (1969) 425.
- [12] D. Brassard, S. Fourmaux, M. Jean Jacques, J.C. Kieffer, and M. A. El Khakani, Appl. Phys. Lett. 87, (2005) 051910.
- [13] J.Y. Suh, R. Lopez, L.C. Feldman, R.F. Haglund, Jr., J. Appl. Phys. 96, (2004) 1209.
- [14] Y. Muraoka and Z. Hiroi, Appl. Phys. Lett. 80, (2002) 583.
- [15] I. Takahashi, M. Hibino, T. Kudo, Jpn. J. Appl. Phys. 40, (2001) 1391.
- [16] G. Xu, P. Jin, M. Tazawa, K. Yoshimura, Appl. Surf. Sci. 244, (2005) 449.
- [17] H. Miyazaki, I. Yasui, Appl. Surf. Sci. 252, (2006) 8367.
- [18] Y. Li, X. Yi, T. Zhang, Chin. Opt. Lett. 3, (2005) 719.

- [19] K. Nagashima, T. Yanagida, H. Tanaka, T. Kawai, *J. Appl. Phys.* 100, (2006) 063714.
- [20] A. Razavi, T. Hughes, J. Antinovitch, and J. Hoffman, *J. Vac. Sci. Technol.* A7, (1989) 1310.
- [21] R. Mlyuka and R.T. Kivaisi, *J. Mater. Sci.* 41, (2006) 5619.
- [22] K.G. West, J. Lu, J. Yu, D. Kirkwood, W. Chen, Y. Pei, J. Claassen, S.A. Wolf, *J. Vac. Sci. Technol. A* 26, (2008) 133.
- [23] J.B. Kana Kana, J.M. Ndjaka, P. Owono Ateba, B.D. Ngom, N. Manyala, O. Nemraoui, A.C. Beye, M. Maaza, *Appl. Surf. Sci.* 254, (2008) 3959.
- [24] B.D. Cullity, *Elements of X-ray diffraction*, 2nd Ed., Addison-Wesley, Reading, Mass. 1978, p102.
- [25] E.E. Chain, *J. Vac. Sci. Technol.* A4, (1986) 432.
- [26] F. Beteille and J. Livage, *J. Sol-Gel Sci. Technol.* 13, (1998) 915.
- [27] H. Futaki and M. Aoki, *Jpn. J. Appl. Phys.* 8, (1969) 1008.
- [28] D. Ruzmetov, K.T. Zailski, V. Narayanamurti, S. Ramanathan, *J. Appl. Phys.* 102, (2007) 113715.
- [29] R. Swanepoel, *J. Phys. E: Sci. Instrum.* 17, (1984) 896.
- [30] A. Frenzel, M.M. Qazilbash, M. Brehm, B.G. Chae, B.J. Kim, H. T. Kim, A.V. Balatsky, F. Keilmann, D.N. Basov, *Phys. Rev. B* 80 (11), (2009) 115115.
- [31] L. Kang, Y. Gao, Z. Zhang, J. Du, C. Cao, Z. Chen, and H. Luo *J. Phys. Chem. C*, 114 (4), (2010) 1901.
- [32] L. Whittaker, C. Jaye, Z. Fu, D.A. Fischer, S. Banerjee, *Am. Chem. Soc.* 131 (25), (2009) 8884.

Chapter 6

PHASES COEXISTENCE IN VO₂ REVEALED BY CONDUCTIVE ATOMIC FORCE MICROSCOPY

Abstract

VO₂ is well-known to exhibit a metal-insulator transition (MIT) at T_c = 68 °C accompanied by an abrupt resistivity change. Since the MIT of VO₂ is known to be a first-order phase transition, it is valuable to check metallic and insulating phase during the MIT process. Conductive atomic force microscopy (C-AFM) allows us to directly image nanoscale metallic puddles that appear at the onset of the MIT. In combination with scanning tunneling spectroscopy, we could distinguish metallic and insulating regions by probing the band gap.

6.1. Introduction

Correlated electron materials (CEM) offer a wide spectrum of properties featuring various types of phase transitions, such as superconductivity, metal-insulator transition and colossal magnetoresistance [1]. A spatial phase inhomogeneity or microdomain structure is frequently observed in these materials [2], where multiple physical phases co-exist at the nano to microscale at temperatures where a pure phase is expected. Despite decades of investigation, the question of whether the phase inhomogeneity is intrinsic or caused by external stimuli (extrinsic) still remains largely unanswered. This question plays a critical role in the understanding of the CEM fundamental physics.

Vanadium dioxide is such a CEM that undergoes a first-order metal-insulator (MIT) phase transition at $T_c = 68\text{ }^\circ\text{C}$ accompanied by the significant changes in conductivity by several orders of magnitude as well as optical properties in the near infrared region. The MIT is accompanied by a structural phase transition from high-temperature tetragonal phase (metallic, M) to the low-temperature monoclinic phase (insulating, I). Because of its MIT, the coexistence of the two phases at some point in the transition process might be expected. Lattice strain has been shown to cause the coexistence of metallic and insulating phases in the Mott insulator VO_2 . Tunneling spectroscopy is one of the most promising methods for the determination of the band gap. The phase's coexistence in VO_2 has been addressed by few researchers cited in chronological order: Choi et al. (1996) [3] suggested, based on optical constants in the mid-infrared region, the metallic and insulating domains coexist, and evolve dynamically as the temperature changes.

Chang et al. (2005) [4] demonstrated direct evidence on the coexistence of metallic and insulating phases just above the phase transition temperature. They also found that the different phases evolve dynamically in the process of the phase transition.

Qazilbash et al. (2007)[5] reported on the electronic properties of a prototypical correlated insulator VO_2 in which the metallic state can be induced by increasing

temperature. They also note that the phase coexistence and percolation in VO₂ are consistent with the thermodynamic evidence of the first-order nature of the phase transition. They showed the collapse of a large (0.5 eV) energy gap and the formation of heavy quasi-particles in the emergent metallic nanopuddles and the percolation occurs at a later stage when these puddles grow and connect.

Kim et al. (2009) [6] performed a tunneling spectroscopy on W-doped VO₂ single crystal near the MIT in order to investigate the change in the electronic structure through the phase transition.

Yin et al. (2009) [7] combined photoelectron spectroscopy (PES) and scanning tunneling microscopy (STM) to study the electronic and geometric structures of the VO₂ thin film surface. Using scanning tunneling spectroscopy, they clearly proved that the bandgap varies from crystallites to crystallites and therefore there is no unique relation between bandgap and crystallite size. They also reported that the bandgap within a single crystallite undergoes relatively small changes as a function of position, and vicinity to the grain boundary has no apparent influence on the local bandgap. Their measurements did not show any strong correlation between the position and the value of the electronic gap.

Cao et al. (2009) [8] used lattice strain to actively control the phase inhomogeneity in the Mott insulator VO₂. They engineered metal-insulator domains along single-crystal VO₂ nano- and microbeams by uniaxial external stress.

The band gap is expressed as a region where the current is zero in the I-V curve, and the gap distance is determined as the length of the flat bottom line in the dI/dV curves around the origin [9,10]. A band gap of less than 0.2 eV is characterized by a very small, flat, region of zero (or very small) current around E_F, and a metallic dI/dV curve lacks the flat region and adopts the characteristic V shape with a residual current at E_F. The lack of a bandgap is also readily apparent in the I-V characteristics.

In this chapter, systematic C-AFM and STS were done to understand the relationship between morphology and electrical transport properties of nanostructure VO_2 and to study the phase's coexistence in this thermochromic material.

6.2. Experimental details

VO_2 thin films were deposited on glass substrate by radiofrequency inverted cylindrical magnetron sputtering. The experimental conditions are similar to those previously reported in other chapters. The thickness of the films was about 100 nm. Conductive AFM was used as a tool to characterize for the change in morphology in VO_2 thin films.

6.3. Results and discussion

6.3.1. Surface topography

The contact mode topographic image shows a relatively island growth of VO_2 on the glass substrate surface as shown in Figure 6.1 (A). The region in between two islands, which looks like a black patch in the topography, may not be the substrate surface. It is the maximum depth beyond which C-AFM cannot probe. One particular advantage of VO_2 for the study of electronic correlations is that the transition to conducting state is initiated by increasing the temperature without the need to modify the stoichiometry. The salient features of the first-order phase transition that occurs at $T_c = 68^\circ\text{C}$ are the orders-of-magnitude increase in conductivity accompanied by a change in the lattice structure [11]. The gross features of the insulator-to-metal transition in VO_2 can be readily identified through the evolution of the C-AFM current images as shown in Figure 6.1 (B and C). Figure 6.1 (B and C) shows the electronic insulator-to-metal transition in progress. At temperature below T_c ($T = 65^\circ\text{C}$), we observed some of the metallic regions nucleate, then grow significantly with increasing temperature, and eventually connect. The metallic regions (light color) give higher conductivity compared with the insulating phase (brown color). From the resistivity measurement [12] well-known in the literature, the VO_2 is purely metallic at the temperature of 85°C . But, as shown in Figure 1 (C), insulating regions remain although many parts of the sample are in the

metallic state. This result can be explained with a percolation model. Although the insulating phase remains, conductivity appears metallic due to the conduction paths made of the metallic regions.

6.3.2. Band-gap of VO₂ nanograin

The phase coexistence of the metallic and insulating phases is well observed in Figure 6.2. We obtained using STS spectra at just above the transition at 85 °C the I-V curves recorded at two specific points representing the insulating (brown color part) and metallic regions (light color part) as shown in Figure 6.1 (C). The two phases can be easily distinguished with current values at finite sample voltage. The curve with brown color shows nearly zero current and has little voltage dependence around zero bias, while the curve with blue color shows linear voltage dependence. These results corroborate with the work done by Chang et al. [4]. These curves correspond to an insulating and a metallic state. The differential conductance of the curve with brown color indicates that the insulating region shows a finite band-gap of 0.4 eV. Yin et al. [7] found a similar value of band-gap for several VO₂ crystallites and reported different band-gap values from 0.2 to 0.8 eV for different positions of the VO₂ crystallites. But there is no strong correlation between the position and the value of the band-gap.

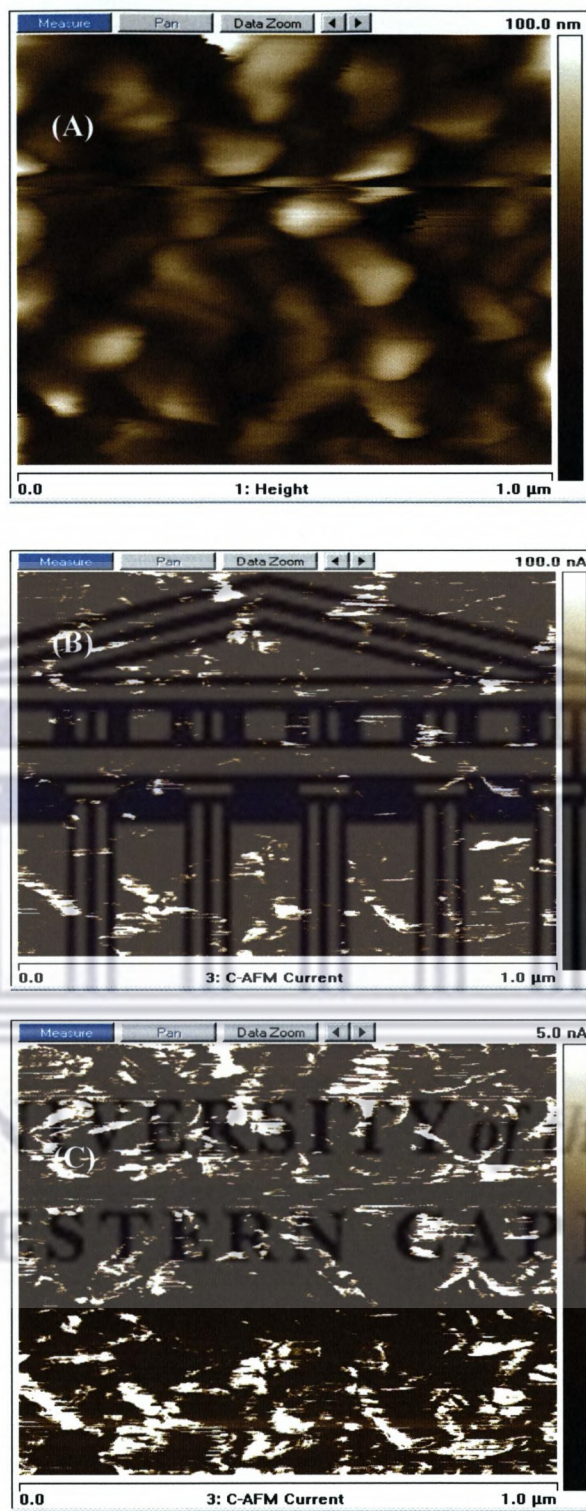


Figure 6.1: Topography (A) and current (B & C) image of a VO_2 thin film of 100 nm on Corning glass substrate sample at a bias of 1.5 volts, 25 pA, 1 μm scan size. (B) Current image of VO_2 film heated at 65 $^\circ\text{C}$ and (C) at 85 $^\circ\text{C}$.

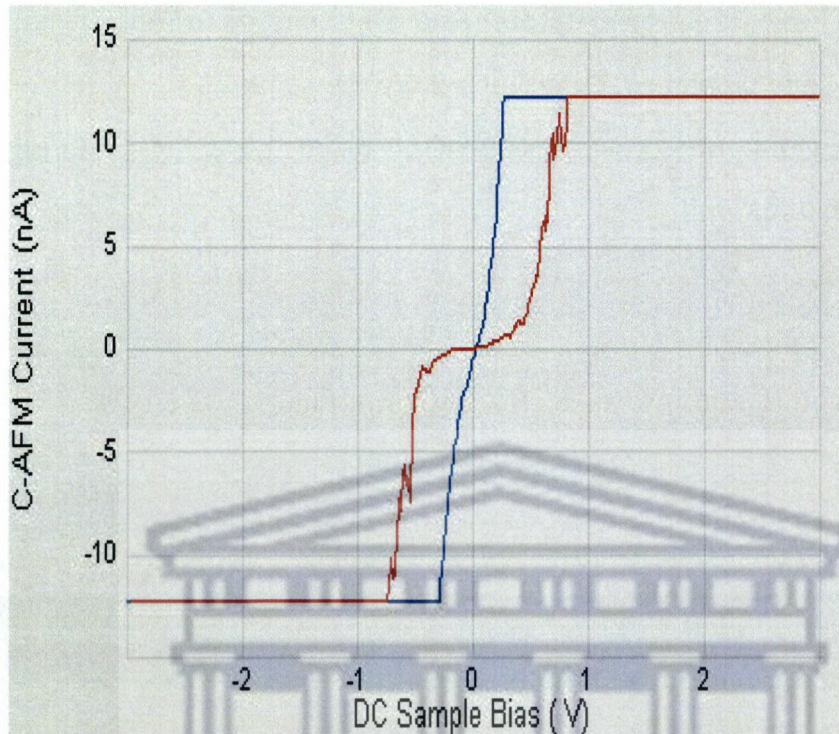


Figure 6.2: Corresponding I-V curves recorded at two specific points representing the insulating (red color) and metallic regions (blue color) as indicated in Fig 6.1C.

UNIVERSITY of the
WESTERN CAPE

6.4. Conclusion

In summary, we studied the metal-insulator phase transition of VO_2 by using Conductive AFM and scanning tunneling spectroscopy. We clearly demonstrated direct evidence on the coexistence of the metallic and insulating phases. The images of phase coexistence and percolation reported here are consistent with the thermodynamic evidence of the first-order nature of the phase transition in VO_2 demonstrated by Allen et al. (1993) [13].

6.5. References

- [1] P.A. Cox, ed., *Transition metal Oxides: An introduction to Their Electronic structure and properties*, Oxford University Press, 1992.
- [2] E. Dagotto, ed., *Nanoscale Phase Separation and Colossal Magnetoresistance*, Springer, 2002.
- [3] H.S. Choi, J.S. Ahn, J.H. Jung, T.W. Noh, D.H. Kim, *Phys. Rev.*, B 54, (1996) 4621.
- [4] J. Chang, C.H. Koo, J.S. Yang, Y.S. Kim, D.H. Kim, J.S. Lee, T.W. Noh, Hyun-Tak Kim, Y. B.G. Chae, *Thin Solid Films* 486, (2005) 46.
- [5] M.M. Qazilbash, M. Brehm, Byung-Gyu Chae, P.C. Ho, G.O. Andreev, Bong-Jun Kim, Sun Jin Yun, A.V. Balatsky, M.B. Maple, F. Keilmann, Hyun-Tak Kim, D.N. Basov, *Science* 318, (2007)1750.
- [6] C. Kim, Y. Oikawa and H. Ozaki, *J. Phys.: Condens. Mat.* 18, (2006) 9863.
- [7] W. Yin, K.G. West, J.W. Lu, Y. Pei, S.A. Wolf, P. Reinke and Y. Sun, *J. Appl. Phys.* 105, (2009) 114322.
- [8] J. Cao, E. Ertekin, V. Srinivasan, W. Fan, S. Huang, H. Zheng, J.W.L. Yim, D.R. Khanal, D.F. Ogletree, J.C. Grossman and J. Wu, *Nature Nanotechnol. Lett.* 2009/ doi: 10.1038/nnano.2009.266.
- [9] M. Preisinger, J. Moosburger-Will, M. Klemm, S. Klimm, and S. Horn, *Phys. Rev. B.* 69, (2004) 075423.
- [10] P.G. Mather, J.C. Read, and R.A. Burhman, *Phys. Rev. B* 73, (2006) 205412.
- [11] M. Imada, A. Fujimori, Y. Tokura, *Rev. Mod. Phys.* 70, (1998) 1039.
- [12] G. Garry, O. Durand, A. Lordereau, *Thin Solid Films* 453, (2004) 427.

- [13] P.B. Allen, R.M. Wentzcovitch, W.W. Schulz, P.C. Canfield, Phys. Rev. B 48, (1993) 4359.



UNIVERSITY *of the*
WESTERN CAPE

Chapter 7

Thermally Tunable Optical Constants of Vanadium Dioxide Thin films Measured by Spectroscopic Ellipsometry

Abstract

Smart materials with reversible tunable optical constants from visible to near-infrared wavelengths could enable excellent control over the resonant response in metamaterials, tunable plasmonic nanostructures, optical memory based on phase transition and thermally tunable optical devices. Vanadium dioxide (VO_2) is a promising candidate that exhibits a dramatic change in its complex refractive index or complex dielectric function arising from a structural phase transition from semiconductor to metal at a critical temperature of 70 °C. We demonstrated the thermal controllable reversible tunability of optical constants of VO_2 thin films. The optical/dielectric constants showed an abrupt thermal hysteresis which confirms clearly the electronic structural changes. Temperature dependence of dielectric constants as well as optical conductivity of sputtered VO_2 thin films was also reported and compared to previous theoretical and experimental reports.

The content of this chapter has been submitted in Optics Communications 2010.

7.1. Introduction

Thermochromic vanadium dioxide (VO_2) materials have received much attention because of their potential technological applications in photonic crystal with tunable band-gap [1,2], field effect transistor, ultraviolet detector [3,4], reversible tunable plasmonic nanostructures [5,6], optical memory based on phase transition [7], and intelligent windows [8]. Among the transition-metal oxides, VO_2 exhibits an abrupt first-order structural phase transition from a semiconductor to a metallic state near 70 °C. This transition is accompanied with a large change of electric resistivity of 3-4 orders of magnitude. Simultaneously, the optical transmission in the near-infrared decreases significantly [9,10]. Drastic changes in the optical properties of VO_2 with the phase transition enable control over the transmission and reflection properties of nanophotonic structures such as holes arrays [11] and metamaterials [12].

VO_2 has a reversible tunable absorption coefficient with an optical gap in the range of 0.5-0.6 eV [13,14]. Several theoretical studies have been performed in order to explain the dielectric response of both phases of VO_2 films. Mossaneck and Abbate [15] have investigated the dielectric response of both the metallic and semiconducting phases of VO_2 using local density approximations (LDA) approach. Tomczak and Biermann [16] used several theoretical approaches to compute the optical conductivity of VO_2 in both phases and compared their results to the experiments. The differences observed in the spectra were strongly dependent on the polarization. So far, there are three satisfying experimental works dealing with the dielectric response as well as the optical conductivity response of VO_2 bulk crystal and thin films. In chronological order, Verleur et al. [9] investigated the electron-band transitions both above and below the transition temperature (T_C) of VO_2 bulk crystal and thin films at different polarizations. In their work, the dielectric functions of VO_2 as well as their peak assignment have been analyzed qualitatively. Okazaki et al. [17] reported the optical conductivity of VO_2 at various temperatures deduced from the optical reflectivity of VO_2 thin films

epitaxially grown on TiO₂ substrate with a specific aim to evidence a strong electron-phonon interaction in the optical conductivity of the insulating phase of VO₂ thin film. Qazilbash et al. [18] reported the charge dynamics on the nanoscale of VO₂ thin films and revealed their Mott transition using well-advanced spectroscopy. Dielectric function and/or optical conductivity can be related to the electronic band structure for this smart material, therefore by analyzing carefully its optical conductivity response; one can clarify the electronic bands, phase transitions and free carrier plasma behavior. One particular advantage of VO₂ for the study of electronic correlations is that the transition from semiconducting to a conducting state occurs by increasing the external temperature stimuli without the need to modify the stoichiometry.

Optical spectroscopy has proved to be a powerful tool for investigating the semiconducting-metal phase transition in numerous strongly correlated electron systems. So far, several optical measurements with an emphasis of optical/dielectric constants have been reported for VO₂ bulk crystals and thin films using a spectrophotometer [9,19,20]. Recently, far-field infrared spectroscopy has been used to probe at the nanoscale the charge dynamics of VO₂ film [18]. Spectroscopic ellipsometry (SE) as an optical spectroscopy can provide information on the electronic transitions in the solid materials and on the overall structure of the sample, including film thicknesses, density and microstructure. Ellipsometry tends to be more powerful than simpler optical measurements. In contrast to a reflectance experiment, which provides one measured parameter, the ratio of the reflected and incident irradiances, an ellipsometry experiment provides two parameters ψ and Δ which are ultimately related to the change in tilt angle and ellipticity of the polarization state [21]. It is important to note that, SE can directly provide optical band-gap, dielectric constants and optical conductivity [22].

The optical switching properties of VO₂ bulk and thin films have been intensively investigated by many researchers in the field. However, little has been done to explore

the thermal tunability of the optical constants/functions of VO₂ thin films. In an earlier study, the dielectric functions of VO₂ bulk and thin films were studied by Verleur et al. [9] using reflectivity and transmission methods. Recently, Kakiuchida et al. [23], using ellipsometric measurements determined the optical constants of VO₂ thin films and discussed quantitatively the relationship between the optical constants and the band structure during the phase transition. However, the reversible structural phase transition through the accurate optical/dielectric constants of VO₂ thin films determined by UVISEL ellipsometer has not been reported yet.

Herein, we report the thermal controllable reversible tunability of optical constants and dielectric functions of VO₂ thin films. The optical/dielectric constants showed an abrupt thermal hysteresis loop which confirms clearly the electronic structural changes at phase transition temperature of 70 °C. We attempt to explain the various features in the deduced optical conductivity of VO₂ thin films by comparing our data to previous theoretical and experimental reports.

7.2. Experimental details

7.2.1. Samples preparation

VO₂ thin films were deposited on glass substrate by radio frequency inverted cylindrical magnetron sputtering (ICMS). The VO₂ films were deposited on glass substrate by sputtering a Vanadium target. Before sputtering, the chamber was evacuated to 5 x 10⁻⁴ Pa. the chamber was filled with a mixture of 10 % O₂ in Ar followed by high purity Ar. The discharge was ignited in a mixture of O₂/Ar (4.44 % O₂ concentration) with a total working pressure of 1.8 Pa, a radiofrequency power of 70 W and a substrate temperature of 450 °C. This low O₂ concentration of 4.44 % was sufficient to completely poison the target as demonstrated in our previous work [5]. The thickness of the films was about 82 nm measured by UVISEL ellipsometer.

7.2.2. Spectroellipsometric measurements and data analysis methodology

A Jobin Yvon – UVISEL spectroscopic ellipsometer with an attached temperature cell was used to characterize the optical properties of VO₂ thin films deposited on glass substrates. The instrument is mainly composed of a Xenon source, a polarizer, an analyser, and a monochromator handling the dispersion and the selection of the wavelength to a photomultiplier. Ellipsometric measurements were performed at two incident angles: 70° (reflexion) and 90 ° (transmission) as a function of the wavelength (spectral range 200-1600 nm) for various temperatures ranging from 30 to 85 °C. Ellipsometry is an optical technique for surface analysis based on the polarization change of light upon reflection on a flat surface. It measures the ellipsometric angles Ψ and Δ which are respectively the amplitude attenuation and the phase change. The UVISEL ellipsometer provides a powerful optical design to continuously cover the spectral range from 142 to 2100 nm. High quality data are delivered across the whole spectral range in terms of high accuracy, high resolution measurements and excellent signal to noise ratio. An optical model that describes the sample structure where each layer refers to a given material is used to compare calculated and experimental data. Unknown parameters of each layer, such as thin film thickness or optical constants or both, are fitted from the DeltaPsi2 software. DeltaPsi2 is a new generation of software based on a common GUI frame, and has been designed to provide intuitive and comprehensive user interaction with the system. This software incorporates the most powerful ellipsometric data acquisition and analysis package for accurate thin film characterization (advanced mathematical fitting algorithms, optical constants fitting, bound fit for simultaneous fitting of up to four parameters); it also includes a large variety of advanced modeling functions to provide the versatility and performance required for a wide range of applications (complete materials library based on dispersion relations, automatic backside correction, graded optical constants etc) . In order to validate the calculated optical

constants, they were determined from a multi-fit, i.e. by simultaneously fitting the measurements performed at two different incident angles. The sample structure for ellipsometric analysis was modeled using three layers: (L₁) VO₂ + air, (L₂), VO₂ films and (L₃) Corning glass substrate as illustrated in Fig.7.1.

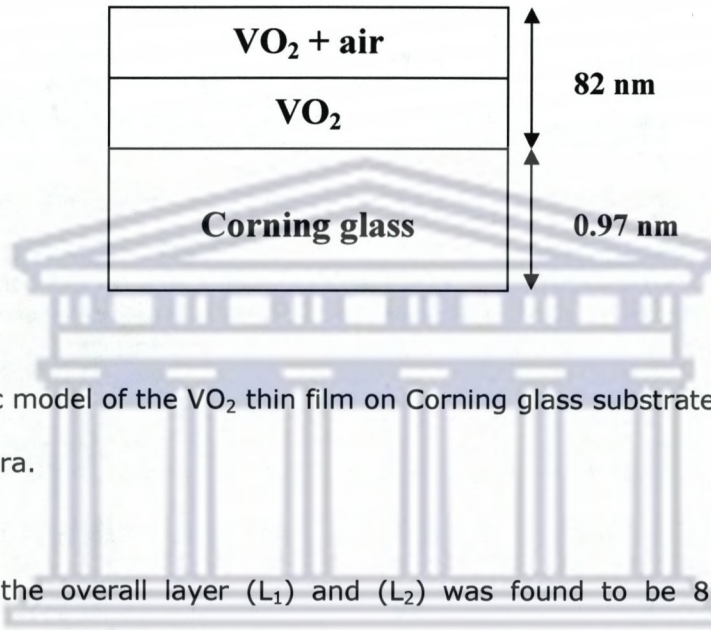


Fig.7.1: Schematic model of the VO₂ thin film on Corning glass substrate used to fit the ellipsometric spectra.

The thickness of the overall layer (L₁) and (L₂) was found to be 82 nm and the substrate thickness 0.97 mm. The effects of surface roughness on ellipsometric data are described in layer (L₁) with a mixture of VO₂ and air by using an effective medium model. The optical constants of VO₂ thin films in layer (L₂) as a function of the frequency were determined by a classical dispersion model based on the sum of Lorentz and Drude oscillators:

$$(n(\omega) + ik(\omega))^2 = \epsilon_\infty + \frac{(\epsilon_s - \epsilon_\infty) \cdot \omega_t^2}{\omega_t^2 - \omega^2 + i\Gamma_0 \cdot \omega} + \sum_{j=1}^n \frac{f_j \cdot \omega_{Lj}^2}{\omega_{Lj}^2 - \omega^2 + i\gamma_j \cdot \omega} + \frac{\omega_p^2}{-\omega^2 + i\Gamma_d \cdot \omega} \quad (1)$$

In the semiconductor phase, the optical constants of VO₂ are fitted with the three first terms corresponding to the Lorentz model dispersion. This formula is based on the classical theory of interaction between light and matter and is used to describe frequency dependent polarization due to bound charges. The constant ϵ_∞ represents a

constant contribution to the real part of the dielectric constant from high frequency electronic transitions. In the second term, ϵ_s gives the value of the static dielectric function at a zero frequency. ω_t and ω_{0j} (in eV) are the resonant frequencies of the oscillators whose energies correspond to the absorption peak. The term, Γ_0 and γ_j , are the broadening of each oscillator also known as the damping factors. The damping effect is due to the absorption process involving transitions between two states. Finally, f_j is the oscillator strength present in the expression of the multiple Lorentz oscillators. While in the case of resonant absorption, these parameters ($f_j, \omega_{0j}, \gamma_j, \dots$) of the j th oscillators have some physical significance, this in general is not true when equation (1) is applied to the spectral region covering interband transitions of bound electrons [9]. Any physical interpretation must derive from a direct study of the spectra. In the metal phase, the last term corresponding to the Drude model is added to the dielectric function because in the metallic phase, VO_2 acts like a Drude metal with strong absorption [24]. This simple model used in the classical mechanical theory of free electron is an extension of a Lorentz oscillator to the case where the restoring force and the resonance frequency are null. Here ω_p is the carrier density parameter and is related to the plasma frequency and Γ_d is the collision frequency. The dielectric functions of the VO_2 films were generated and compared with those reported in the literature by Verleur et al. [9]. A significant enhancement of the dielectric functions profiles was obtained. The oscillator parameters coming from the fit of the measurements performed at 30 °C and 85 °C are listed in the Table 7.1.

	T = 30 °C							T = 85 °C			
f_j	0.67	-0.46	1.11	2.38	1.60	3.4	0.54	0.87	1.76	2.35	-8
ω_{oj}	1.02	1.92	1.39	3.45	4.28	7.57	2.98	2.87	3.46	5.26	0.57
γ_j	0.54	3.02	0.88	1.34	2.24	2.02	0.65	0.77	1.34	2.81	3.70
ω_p								4.47			
Γ_d								0.82			

Table 7.1: Drude-Lorentz parameters values of VO₂ thin films determined from the simulation of ellipsometric spectra

7.3. Results and discussion

7.3.1 Optical Constants

The wavelength dispersions of the refractive index, n , and extinction coefficient, k , of sputtered VO₂ thin films of both phases (semiconductor at $T < T_C$ and metal at $T > T_C$) are shown in Fig.7.2. From Fig. 7.2a and b it can be clearly seen that the switching of the optical constants n and k of VO₂ as external temperature increases is highly accentuated in the near-infrared region compared to the visible region. This significant switching of the optical constants of VO₂ confirms its good thermochromic properties. It is a worth noticeable that at wavelength around 1000 nm, n decreases and increases by roughly two with the rise and drop of temperature, k increases and and decreases respectively and such a change is more marked at a longer wavelength in the optical constants spectra. A similar trend has also been observed by Kakiuchida et al. [23]. Fig. 7.3a and b shows a typical temperature dependence of the optical constants n and

k at the following different wavelengths 497 nm (visible region), 1033 and 1459 nm (near-infrared region). It is clearly seen that the optical constants n and k are tunable in a reversible manner in the visible and near-infrared regions when temperature is changed through the transition located at 70 °C. The ratios of optical constants defined as $n_1 = n_{30^\circ\text{C}}/n_{85^\circ\text{C}}$ and $k_1 = k_{30^\circ\text{C}}/k_{85^\circ\text{C}}$ at the three aforementioned wavelengths are found to be 1.20, 2.07, 1.93, and 0.93, 0.32, 0.09 respectively. Those values confirm a drastic switching of the optical constants of VO₂ typically in the near-infrared regions. From Fig.7.3a and b, it can be seen that our VO₂ film exhibits highly enhanced switching properties of n and k in the near-infrared region as well as a strong sharpness of the phase transition as compared to the work done by Kakiuchida et al. [24]. However, good switching characteristics such as transition temperature, hysteresis width and sharpness of the transition are known to indicate a high degree of stoichiometry of the VO₂ films. Hence it was been proved by Nagashima et al. [25] that the switching of n and k of VO₂ thin films strongly depends on the growing conditions. The optical constants hysteresis behavior is similar to the optical transmittance/absorbance hysteresis of VO₂ thin films. The hysteresis width of about 10 °C of the refractive index with an abrupt variation of n at 70 °C is similar to that obtained in optical transmittance of polycrystalline sputtered VO₂ thin films [26]. The extinction coefficient, k also displays excellent phase transition characteristics only in the near-infrared region. At wavelength of 497 nm, there are no switching properties at all therefore flat hysteresis behavior observed.

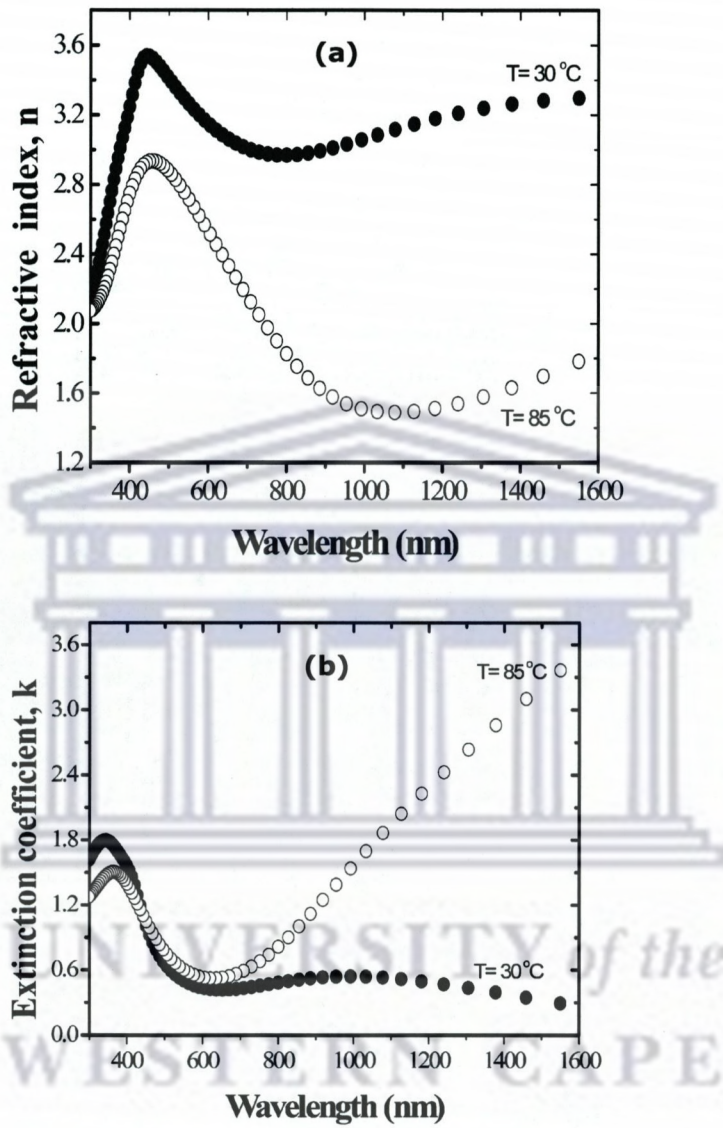


Figure 7.2: (a) Refractive index, n and (b) extinction coefficient, k of sputtered VO₂ thin films at temperature below and above the phase transition temperature of 70 °C determined by variable angle spectroscopic ellipsometry.

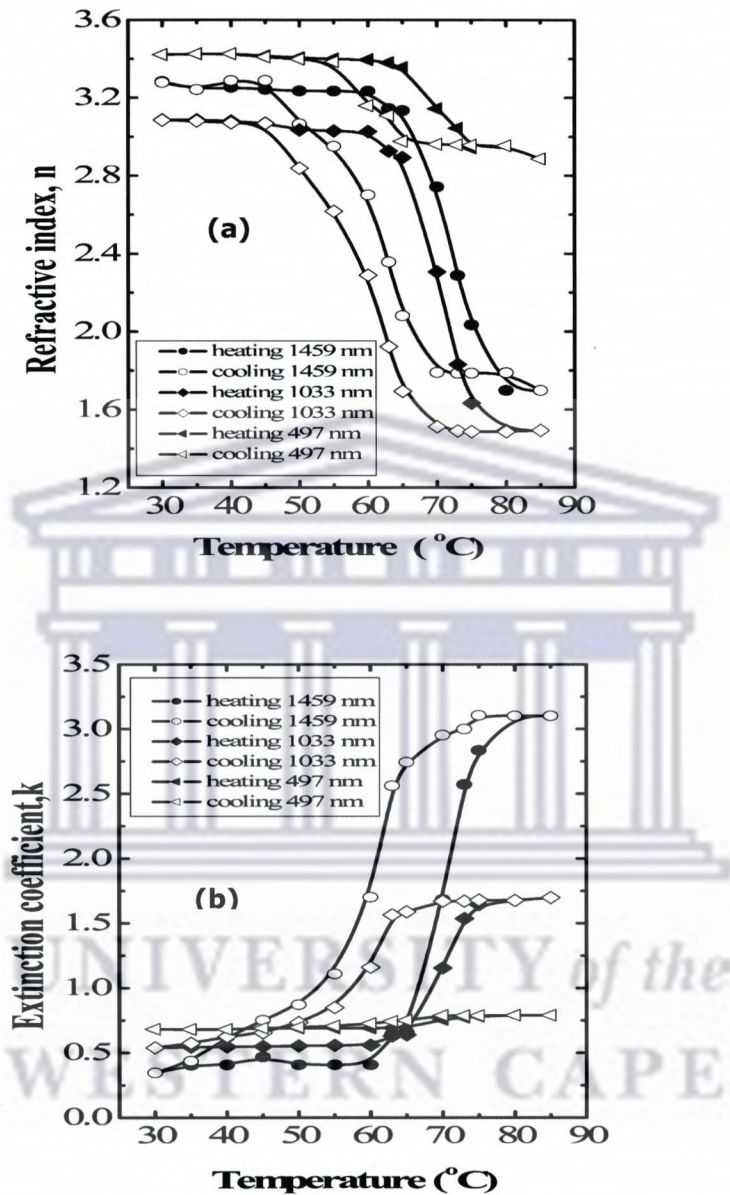


Figure 7.3: Variation of optical constants (refractive index, n (a) and extinction coefficient, k (b)) at wavelengths 497 nm (visible region), 1033 and 1459 nm (near-infrared region) as a function of external temperature stimuli of sputtered VO_2 thin films.

7.3.2. Dielectric Constants

Fig. 7.4a shows the imaginary and real part of the dielectric constant of VO₂ at temperatures below and above the critical temperature of VO₂ (T_c = 70 °C). The frequencies of peaks appearing in the imaginary parts of the dielectric constants at both temperatures T > T_c and T < T_c are listed in table 7.2. Table 7.2 presents the previous findings alongside the present findings on peaks appearing in Im[ε] of VO₂ thin films. In this table, it can be seen that the present results display few optical absorption peaks.

	Verleur et al. Ref.9	Mossaneck et al. Ref.15	Present work
	1.0		
T < T _c	1.3	1.6	1.25
	2.8	2.8	
	3.5	3.6	3.25
		3.8	
T > T _c	0.85	0.8	0.85
		1.2	
	2.8	2.8	
	3.5	3.7	3.15

Table 7.2: An outline of previous and present findings of frequencies of peaks (eV) appearing in the spectra of the imaginary part of the dielectric constant of VO₂

Apart from the fact that the nonexistence of certain optical absorption peaks in the present results, the energy position of those peaks agrees well with previous findings. We attempt to explain the various features in the dielectric constants of VO₂ thin films by comparing our data to previous theoretical and experimental reports. Peaks at finite

energies in the dielectric constants occur when there are direct optical transitions between filled and empty band in a solid. More precisely, the interband optical transitions are governed by the electric dipole transition matrix elements and peaks in the joint density of (filled and empty) states [9]. In the metallic phase, e.g. at 85 °C of the imaginary dielectric constant of VO₂, one can clearly observe a Drude-like peak below 1.5 eV and a strong peak around 3.15 eV. As a temperature decreases down to the insulating phase e.g. 30 °C the Drude like peak becomes strongly suppressed and the peak around 3.15 eV is shifted towards higher energy. The Drude-like peak can be attributed to the free carrier responses in the broad d_{||} and π* bands whereas the strong peak at 3.15 eV can be attributed to the transition from the O_{2p} to the Vπ* bands [14]. This assignment is in good agreement with Verleur et al. [9]. In the insulating phase e.g. at 30 °C above 2.5 eV structure similar to that observed at 85 °C of the Im[ε] and attributed to transitions between O_{2p} bands and the empty V_{3d} bands is present. The peak located at 1.25 eV could be assigned as the d-d transition from the occupied d_{||} to the unoccupied π* bands [14]. This assignment is consistent with recent band calculations [27].

To further probe the dependence of the real part of the dielectric function in the frequency of 0.83 eV (~1497 nm), a variation of Re[ε] as a function of the external temperature stimuli has been shown in Fig.7.4.b. It is clearly evident that Re[ε] exhibits a reversible hysteresis. The reversible change in Re[ε] against temperature due to thermochromism was observed at transition temperature of 70 °C with a strong sharpness. It is interesting to note that such abrupt changes of Re[ε] are quite similar to that associated with n and k shown in Fig.7.3a and b respectively. Hence theoretically the real and imaginary parts of the dielectric functions are directly related to the optical constants by the well-known formula reported in the literature $\text{Re}[\epsilon] = n^2 - k^2$ and $\text{Im}[\epsilon] = 2nk$. The behavior displayed by Re[ε] with external temperature stimuli confirms the nature of the semiconductor-to-metal transition.

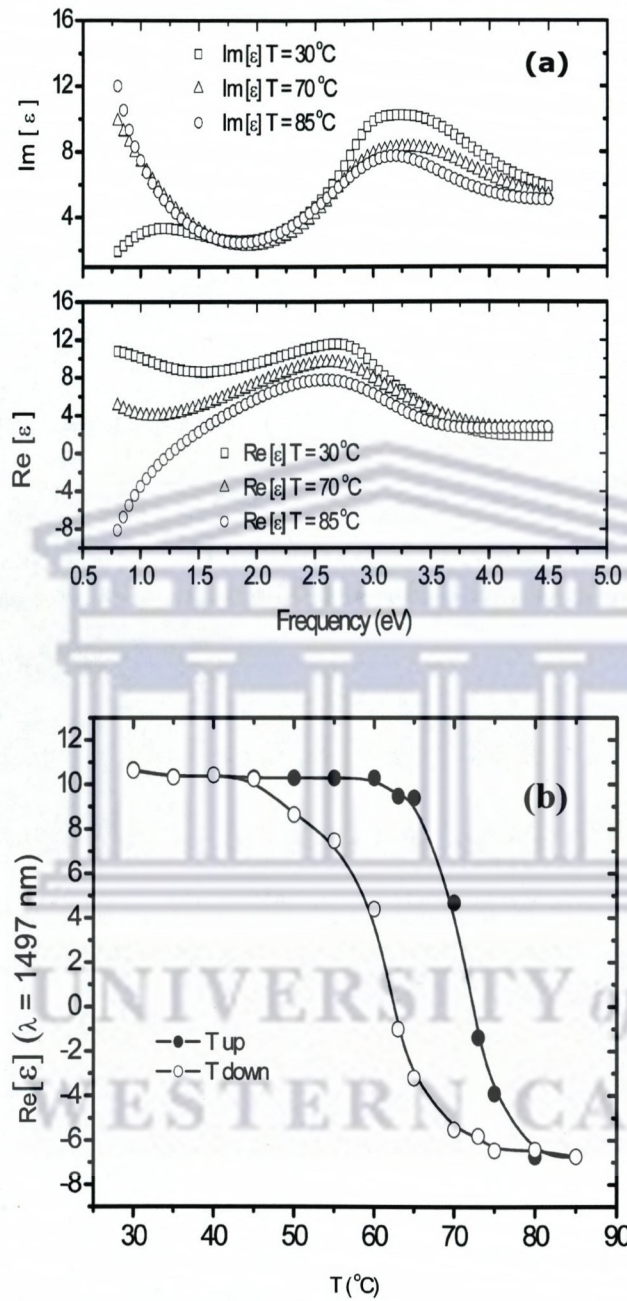


Figure 7.4: (a) Real and imaginary part of dielectric function of VO₂ thin films below, at and above the phase transition temperature $T_c = 70$ °C. (b) Thermal hysteresis behavior of the real part of the dielectric function of sputtered VO₂ thin films.

7.3.3. Optical Conductivity

Fig.5 shows the real part of the optical conductivity defined as $\sigma_1(\omega) = \frac{\omega \text{Re}[\epsilon]}{4\pi}$ of VO₂ as a function of photon energy (ω) for various external temperature stimuli. The features in $\sigma_1(\omega)$ of M1 monoclinic semiconducting phase and rutile metallic phase will be explained within the model of energy levels reported in Refs.[28-30]. Within band theory calculations, the crystal field splits the degenerate d orbitals into t_{2g} bands and e_g^σ bands. The former are lower in energy and contain the single d electron under the tetragonal crystal field. The t_{2g} bands are further split into a_{1g}, e_g^π bands, with the latter centered at higher energy compared to the former. The d_{//} and the π* orbitals correspond to the a_{1g}, e_g^π respectively. The hump in Fig.5 labeled "A" at 1.25 eV is due to optical transitions from the filled lower d_{//} band to the empty π* bands. Peak "C" at 3.50 eV is due to transitions from the filled O_{2p} bands and empty π* bands. This assignment is consistent with the electrodynamic studies of the VO₂ film reported by Qazilbash et al. [32]. We do not observe any obvious features of excitonic peak located at 2.5 eV which correspond to transitions from lower filled d_{//} band to narrow upper empty d_{//} band. Such peak of excitonic nature was found in optical conductivity of VO₂ film grown on (1010) sapphire and TiO₂ (001) [32,17]. A broad Drude-type feature is observed in the optical conductivity of the rutile metallic phase (T>T_c) (labeled "q"). A peak labeled "s" at 3.35 eV which we attribute to optical transitions from the O_{2p} bands to partially filled π*. We do observe a peculiar feature known as fingerprints of doped Mott insulator [31] named isosbestic point located at 1.54 eV. It is defined as the location of equal conductivity for all spectra obtained at different temperatures. This value is comparable to the one previously reported by Qazilbash et al. [18]. The inset of Fig.5 shows a temperature dependence of the peak "C" and "s" position as well as

their full width at half maximum. Peak "C" and "s" are described by a nearly Lorentzian line shape with half-width varying from 1.8 eV to 1.9 eV with temperature. Peak "C" at 3.5 eV shifts towards lower energy around 3.35 eV (peak "s"). Similar shift of the peak "C" position was observed by Qazilbash et al. [32] from 3.2 eV at insulating phase to 3.1 eV at rutile metallic phase. The fluctuation of the peak "C" position across the metal-insulator transition temperature could be due to the fact that the VO₂ film is in the region of strong correlation. Therefore, thermal induced transition from insulator to metal is accompanied by the changes of interband optical transitions. In VO₂ rutile metal phase, the energy gap collapses and the Fermi level crosses partially filled d_{//} and π^* bands.



UNIVERSITY *of the*
WESTERN CAPE

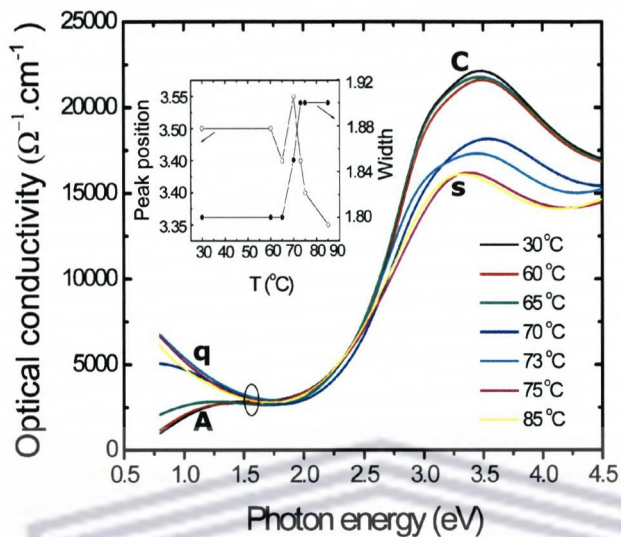


Figure 7.5: Real part of the optical conductivity of VO_2 thin films as a function of frequency for various external temperatures stimuli. The open circle shows the isosbestic (equal conductivity) point for all spectra. The inset shows the temperature dependence of the peak position (range of 3.0-3.5 eV) and its width of the real part of the optical conductivity. The straight lines in the inset are only used to guide the eyes.

7.4. Conclusion

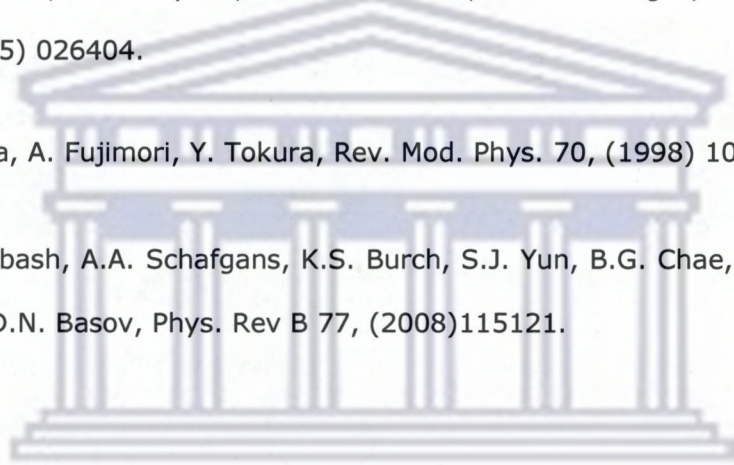
We have demonstrated the active modulation of optical constants of VO_2 thin films through the application of external temperature stimuli. The optical/dielectric constants of VO_2 have displayed an abrupt hysteresis loop which confirms their reversible tunability induced thermally, significant feature of structural phase transition. The optical conductivity of VO_2 thin films grown on glass substrate at various external temperatures stimuli deduced from spectroscopic ellipsometry has shown an excellent feature of semiconductor-metal transition comparable to previous theoretical and experimental reports.

7.5. References

- [1] D. Xiao, K.W. Kim, and J.M. Zavada, *J. Appl. Phys.* 97, (2005) 106102.
- [2] V.G. Golubev, V.Y. Davydov, N.F. Kartenko, D.A. Kurdyukov, A.V. Medvedev, A.B. Pevtsov, A.V. Scherbakov, and E.B. Shadrin, *Appl. Phys. Lett.* 79, (2001) 2127.
- [3] H.-T. Kim, B.G. Chae, D.H. Youn, S.L. Maeng, G. Kim, K.Y. Kong, and Y.S. Lim, *New J. Phys.* 6, (2004) 52.
- [4] L.A.L. de Almeida, G.S. Deep, A.M.N. Lima, and H.Neff, *Opt. Eng.* 41, (2002) 2582.
- [5] J.B. Kana Kana, J.M. Ndjaka, B.D. Ngom, N. Manyala, O. Nemraoui, A.Y. Fasasi, R. Nemutudi, A. Gibaud, D. Knoesen, M. Maaza, *Thin Solid Films* 518, (2009)1641.
- [6] M. Maaza, O. Nemraoui, C. Sella, A.C. Beye, B. Baruch-Barack, *Opt. Commun.* 254, (2005) 188.
- [7] A.A. Bugayev and M.C. Gupta, *Opt. Lett.* 28, (2003) 1463.
- [8] P. Jin, G. Xu, M. Tazawa, and K. Yoshimura, *Appl. Phys. A* 47, (2003) 455.
- [9] H.W. Verleur, A.S. Barker, Jr and C.N. Berglund, *Phys. Rev.* 172, (1968) 788.
- [10] J.B. Kana Kana, J.M. Ndjaka, P. Owono Ateba, B.D. Ngom, N. Manyala, O. Nemraoui, A.C. Beye, M. Maaza, *Appl. Surf. Sci.* 254, (2008) 3959.
- [11] J.Y. Suh, E.U. Donev, R. Lopez, L.C. Feldman and R.F. Haglund, *Appl. Phys. Lett.* 88, (2006)133115.
- [12] T. Driscoll, S. Palit, M.M. Qazilbash, M. Brehm, F. Keilmann, B.G. Chae, S.J. Yun, H.T. Kim, S.Y. Cho, N.M. Jokerst, D.R. Smith and D.N. Basov, *Appl. Phys. Lett.* 93, (2008) 024101.
- [13] L. Ladd and W. Paul, *Solid State commun.* 7, (1969) 425.

- [14] C.H. Koo, J.S. Lee, M.W. Kim, Y.J. Chang, and T.W. Noh, J.H. Jung, B.G. Chae, and H.-T Kim, ArXiv:cond-mat/0508212, 2005.
- [15] R.J.O. Mossaneck and M. Abbate, J. Phys.: Condens. Matter 19, (2007) 346225.
- [16] M. Jan Tomczak and S. Biermann, Phys. Rev. B 80, (2009) 085117.
- [17] K.Okazaki, S.Sugai, Y. Muraoka, and Z. Hiroi, Phys. Rev. B 73,(2006) 165116.
- [18] M.M. Qazilbash, M. Brehm, Byung-Gyu Chae, P.-C. Ho, G.O. Andreev, Bong-Jun Kim, Sun Jin Yun, A.V. Balatsky, M.B. Maple, F. Keilmann, Hyun-Tak Kim, D.N. Basov, Science 318, (2007)1750.
- [19] A.S. Barker Jr, H.W. Verleur and H.J. Guggenheim, Phys. Rev. Lett. 17 (1966) 1286.
- [20] H.S. Choi, J.S. Jung, T.W. Noh and D.H. Kim, Phys. Rev. B 54, (1996) 4621.
- [21] W.R. Collins and Y.T. Kim, anal. Chem., 62, (1990) 887.
- [22] A. Kasic, M. Schubert, S. Einfeldt, D. Hommel, T.E. Tiwald, Phys. Rev. B 62, (2000) 7365.
- [23] H. Kakiuchida, P. Jin, S. Nakao and M. Tazawa, Jpn. J. Appl. Phys. 46, (2007) L113.
- [24] M.J. Dicken, K. Aydin, I.M. Pryce, L.A. Sweatlock, E.M. Boyd, S. Walavalkar, J. Ma and H.A. Atwater, Optics Express 17, (2009) 18330.
- [25] M. Nagashima, H. Wada, Thin Solid Films 312, (1998) 61.

- [26] J.B. Kana Kana, J.M. Ndjaka, B.D. Ngom, A.Y. Fasasi, O. Nemraoui, R. Nemutudi, D. Knoesen, M. Maaza, *opt. Mater.* 32, (2010) 739.
- [27] A. Continenza, S. Massidda and M. Posternak, *Phys. Rev. B* 60 (1999) 15699.
- [28] J.B. Goodenough, *Phys. Rev.* 117, (1960) 1442.
- [29] V. Eyert, *Ann. Phys. (Leipzig)* 11 (2002) 9.
- [30] S. Biermann, A. Poteryaev, A.I. Lichtenstein, and A. Georges, *Phys. Rev. Lett.* 94, (2005) 026404.
- [31] M. Imada, A. Fujimori, Y. Tokura, *Rev. Mod. Phys.* 70, (1998) 1039.
- [32] M.M. Qazilbash, A.A. Schafgans, K.S. Burch, S.J. Yun, B.G. Chae, B.J Kim, H.T. Kim, and D.N. Basov, *Phys. Rev B* 77, (2008)115121.



UNIVERSITY *of the*
WESTERN CAPE

Chapter 8

THERMOCHROMIC NANOCRYSTALLINE Au-VO₂ COMPOSITE THIN FILMS PREPARED BY RADIOFREQUENCY INVERTED CYLINDRICAL

Abstract

Highly crystalline Au-VO₂ nanocomposite thin films were prepared on Corning glass substrates by radiofrequency inverted cylindrical magnetron sputtering (ICMS). It is a low cost potential coating technology for the production of large area uniform nanocomposite thin films exhibiting plasmonic properties. This paper reports the synthesis and feasibility of reliably reproduced high quality of Au-VO₂ by ICMS. Structural, morphological, interfacial analysis and optical properties of synthesized Au-VO₂ nanocomposite thin films are reported.

The content of this chapter has been published in Thin Solid Films 518 (2010) 1641-1647.

8.1. Introduction

Nanocomposite consisting of noble metal nanoparticles (Au, Ag or Cu) embedded in a dielectric matrix attracted much attention recently because of their large number of potential applications, which include ultrafast optical switches due to their nonlinear susceptibilities and fast response time [1, 2], surface enhanced spectroscopies, biomedical sensors [3-5], thermally optical switches or coatings [6], optical sensing [5,7], photothermal medical therapeutics and solar glazing [8]. The wavelength tuning of the surface plasmon resonance is highly desirable in the applications of the metallic nanoparticles. Since the surface plasmon resonance wavelength (λ_{SPR}) depends on their particle size, shape, inter-particle distance and the dielectric function of the surrounding host [9-13], the tunable λ_{SPR} in the visible and near infrared regions has been achieved by changing these parameters of the metallic nanoparticles [9-14]. Recently, a great interest has been made to tune λ_{SPR} of noble metal nanoparticles by using dielectric functional materials such as thermochromic [15-18], electrochromic [19] or photochromic [20], as the matrices. The use of dielectric functional materials as the matrices opens a range of possibilities for tuning the λ_{SPR} in a controllable manner. Recently, the effect of external temperature stimuli on the plasmon resonance of Au or Ag nanoparticles embedded in a thermochromic VO₂ matrix, of composite Au-VO₂ [17,18] or Au-on-VO₂ core shell particles [8,21] or Ag on top of VO₂ [15] has been sparsely explored with only few reports. It is well-known that VO₂ undergoes a reversible first-order phase transition from semiconductor to metal at critical temperature $T_c = 68$ °C, accompanied by large change in optical properties in the infrared region [22-24] which will be exploited to modulate the λ_{SPR} .

So far we are aware of a few reports to date on nanocomposite films consisting of noble metal nanoparticles of Au or Ag embedded in a thermochromic VO₂ matrix by some researchers. Maaza et al. synthesized Au-VO₂ films by off-axis pulsed laser deposition and presented a method to thermally tune the surface plasmon frequency in

a controllable manner [17, 18]. Xu et al. sputtered silver (Ag) and gold (Au) on top of a VO₂ thin film by planar radiofrequency (rf) magnetron sputtering, showed the dependence of the silver nanoparticles localized surface plasmon resonance (LSPR) wavelength position on the silver mass thickness [15] and demonstrated that Au nanoparticles have a marked effect on the reduction in the phase transition temperature of VO₂ [25] respectively. The modulation of the LSPR on lithographically fabricated gold nanoparticles arrays on VO₂ overlayer deposited by pulsed laser deposition was reported by Suh et al. [16]. Aggregates of gold spheres in a matrix of VO₂ prepared by Sol-gel method was investigated by Cavanna et al. in order to carry out the optical switching performances of this nanocomposite [26]. The synthesis of gold doped vanadium dioxide by hybrid aerosol assisted and atmospheric pressure chemical vapor deposition was recently presented by Binions et al. [27].

The reactive sputtering process is a widely used coating technique for the production of oxides, nitrides, carbides and nanocomposites. The main drawbacks of this process are the hysteresis behavior, which seriously limit the stability, the poisoning of the sputtering target, which substantially reduces the sputter erosion rate, the stability control and arcing effect. Considerable efforts have been devoted to eliminate these drawbacks such as (i) increasing the pumping speed, which requires larger additional costs; (ii) increasing the target-to-substrate distance, which requires larger chambers (hence, higher costs); (iii) plasma emission monitoring; (iv) pulsed reactive gas flow, which requires an amount of optimization and a continuous monitoring and adjustment of the process; (v) dual magnetrons or magnetron with a full target erosion; (vi) substoichiometric ceramic target; and (vii) voltage control [28, 29]. Planar reactive magnetron sputtering suffers most of these undesirable phenomena. Planar sputtering also suffers from being a line-of-sight process and is not well suited for coating non-planar substrates. Inverted cylindrical magnetron sputtering (ICMS) also known as hollow cathode sputtering is used to sputter from the inner surface of cylindrical

targets and produce highly conformal coatings [30]. Due to its enclosed geometry, it also produces intense and very uniform plasma next to the target surface that results in high deposition rates [31]. Hollow cathodes also lead to excellent target erosion because the sputtered atoms that are not deposited on the substrate get redeposited on the cathode. An additional advantage of hollow cathodes is their lower target cost and they produce large area uniform films [32, 33]. Despite the main feature of pulsed laser deposition (PLD) which is that the stoichiometry of the target can be retained in the deposited films, the major problems of PLD are splashing or microparticulates deposition on the films which greatly affect the growth and the properties of the films and the narrow angular distribution of the ablated species. These drawbacks limit the usefulness of PLD in producing large area uniform thin films. Production related issues of PLD concerning reproducibility [34], large-area scale-up [35] have begun to be addressed. Recently, some technological issues have been addressed on the hollow cathode sputtering. Lindberg et al. [36] reported the hysteresis behaviour in the target voltage while depositing Al-O films. They used a hollow cathode magnetron with a low-frequency AC power. Such setup resembles a dual target magnetron sputtering rather than a hollow cathode source. Pradhan et al. [37] reported that, the hollow cathode does not exhibit the hysteresis behaviour generally observed in planar reactive sputtering systems and is stable at all operating points without any feedback control. They explained the absence of the hysteresis behavior on the basis of the enclosed geometry, which significantly reduces the sputtered flux leaving the hollow cathode sputtering. These properties strongly indicate that hollow cathode sputtering has sufficient possibilities to prepare "smart" class of nanocomposite films with a wide range of technological applications. A possibility to form nanocomposite thin films of Au-VO₂ by reactive ICMS is demonstrated.

This chapter reports on the preparation of highly nanocrystalline Au-VO₂ composite thin films by radiofrequency inverted cylindrical magnetron sputtering. The structural,

morphological and optical properties of the synthesized films have been studied. Our results have been compared to those previously reported for Au-VO₂ films prepared by other deposition techniques.

8.2. Experimental details

8.2.1. Sample preparation

A cylindrical vanadium metal sheet 99.98 % purity (Alfa Aesar) 5 cm in diameter and 2.5 cm long with a triangular slice of high purity gold 99.99 % (metal basis) 1 mm thick carefully stuck by silver paint on the wall of the cylindrical vanadium metal, was used as a target. This target was mounted on the cathode of the sputter gun, also called an Inverted Cylindrical magnetron (ICM) gun or hollow cathode source. The ICM gun is mounted in a double cross-piece vacuum chamber on a standard DN 100 CF flange with a mounting depth of 12 cm. The Corning glass substrates (glass number 0810401) were ultrasonically cleaned in acetone and subsequently in ethanol for 10 min, respectively, rinsed in des-ionized water and then dried in the oven at 100 °C. The dried substrates were glued with silver paint onto the heated substrates holder perpendicular to the target and along its central axis as illustrated in Figure 8.1. The position of the substrate was a crucial parameter to fabricate high quality of films exhibiting plasmonic features. The substrates placed at any position inside the hollow cathode revealed a pure gold metallic character in few minutes of deposition because of the fast sputtering of gold slice stuck on the wall of the cylindrical vanadium metal. Films exhibiting pure gold metallic character do not show any plasmon resonance feature as reported by Xenogiannopoulou et al. [38]. The distance of 2 cm from substrate holder to sputtering head of our configuration adopted and shown in Figure 1 was an optimal distance to fabricate good quality of films revealing plasmonic feature. This position only leads to low deposition rate because the plasma is just collected at the exit of the hollow cathode. Other positions further than 2 cm lead to even lower deposition rate. The temperature of the sample holder was controlled using a k-type

thermocouple connected to a 3216 PID controller supplied by Eurotherm. After pumping the deposition chamber to a base pressure of 5×10^{-4} Pa, the chamber was backfilled with a mixture of 10 % O_2 in Ar followed by high-purity Ar. The discharge was ignited in a mixture of O_2/Ar (4.44 % O_2 concentration) with a total working pressure of 1.8 Pa. This pressure is higher than what is typically used for planar magnetron sputtering. Such high pressure is needed for a smooth operation of the hollow cathode sputtering. A very high total pressure of 8.67 Pa was obtained by Pradhan et al. [37] using hollow cathode sputtering to deposit alumina thin films. The low oxygen concentration of 4.44 % was sufficient to completely poison the target. Hence, it was well demonstrated by Pradhan et al. [37] that the transition from metallic to poison mode with hollow cathode sputtering occurs gradually at very low oxygen concentrations while in planar sputtering this transition occurs abruptly at higher oxygen concentrations. In the same trend, Delahoy et al.[39] reported that only a very small amount of oxygen is sufficient to immediately oxidize (poison) the target if the oxygen passes through the cathode of hollow cathode sputtering. We believe that this is due to the enclosed geometry of the hollow cathode sputtering, which confines most of the sputtered atoms and ions within the hollow cathode. The ICM gun was operated at a power of 70 W using a Dressler Cesar (13.56 MHz) rf power generator for 45 min. Copper cooling water tubes wrapped around the circumference of the hollow cathode were used to cool the ICM gun during operation. A pre-sputtering time of 30 min was used to remove surface contamination and oxides on the target and to ensure stabilized sputtering conditions. In this work, Au- VO_2 nanocomposites films were prepared at different substrate temperatures ranging from 400 °C to 600 °C. The thickness of the sputtered Au- VO_2 films ranges from 64 to 70 nm. The volume fraction of gold in the sputtered samples was found to be slightly changed and ranges from 6.3 to 6.9 % as determined by simulation of experimental X-ray reflectivity profiles.

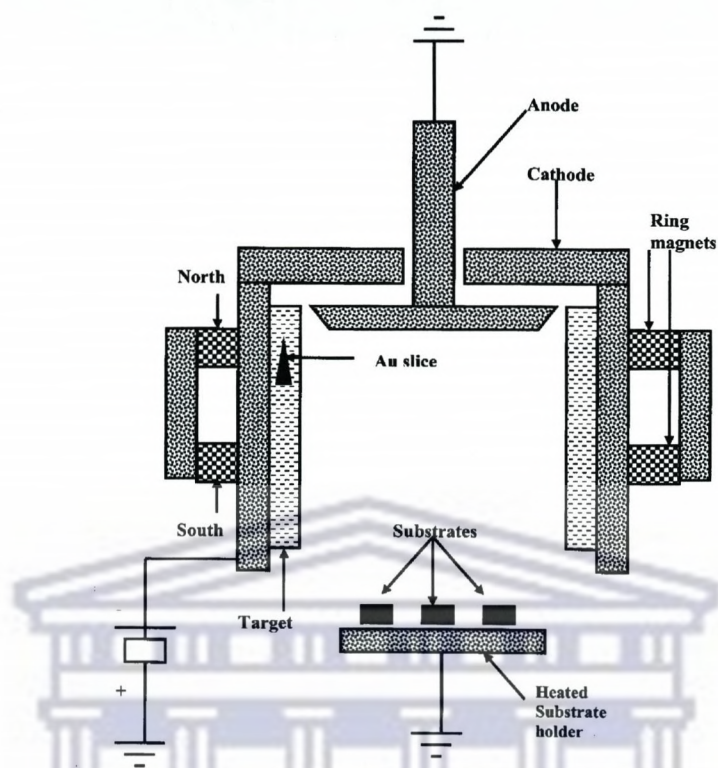


Figure 8.1: Schematic illustration of the inverted cylindrical magnetron (ICM) sputter gun. The target is the cylindrical ring vanadium metal in which a triangular slice of gold was stuck. The circular magnets were enclosed behind the target. The anode and cathode (target) are perpendicular to each other and the substrates lie perpendicular to the target.

8.2.2. Sample evaluation

The crystalline structure of the Au-VO₂ composite thin films was determined by X-ray diffractometry (XRD) in a θ -2 θ mode with CuK α (AXS Bruker). The surface morphology of the films was observed by atomic force microscopy (AFM) using Nanoscope III a, Digital Instruments operated in tapping mode under ambient conditions. X-ray reflectivity at wavelength of 1.54 Å on a Panalytical X-pert reflectometer of the

“Laboratoire de Physique de l’Etat Condensé-Université du Maine.” was used for the analysis of surface and interface of the films. The plasmonic properties and thermochromic behavior of the synthesized films were examined by using a Spectrophotometer (CECIL 2000) incorporated with Peltier thermoelectric heating and cooling stage.

8.3. Results and discussion

8.3.1. Film structure

Fig. 8.2 shows the XRD patterns of Au-VO₂ nanocomposite films sputtered in the substrate temperature range of 400-600 °C. These films were deposited on Corning glass substrates. There are diffraction peaks for both Au and VO₂ in the synthesized films. This indicates that both components were crystallized. The spectra exhibited seven peaks in the 2θ range of 20-70 °, four of which correspond to the VO₂ monoclinic (011), (002), (220) and (022) planes, and the other three peaks (111), (200), (220) are assigned to gold fcc. The same peaks occur in all the spectra for different temperatures, but their relative intensity changes. The VO₂ (002) peak gradually disappears with increasing substrate temperature and completely disappears at substrate temperature of 600 °C. Also, the VO₂ (220) and (022) peaks show a relative variation of intensity. This indicates that a texture of the host matrix VO₂ may change with increasing substrate temperature. The intensity in all gold peaks increases with increasing deposition temperature and we noticed that the higher the substrate temperature, the sharper are the gold peaks. From the strongest Au (111) and VO₂ (011) peak width, the size of the gold and VO₂ particle was calculated using Scherrer’s formula [40]. Fig. 8.3 shows the relationship between the Au and VO₂ particle size and the substrate temperature. It can be seen that the Au and VO₂ particle sizes both increased upon increasing the substrate temperature. The Au particles first grew

rapidly from 9.9 nm to 25.4 nm in the substrate temperature range of 400-500 °C, but then slightly decreased or saturated for substrate temperature higher than 500 °C. The VO₂ particle size increased linearly with increasing substrate temperature in the range of 400-550 °C and then dropped slightly at substrate temperature of 600 °C.

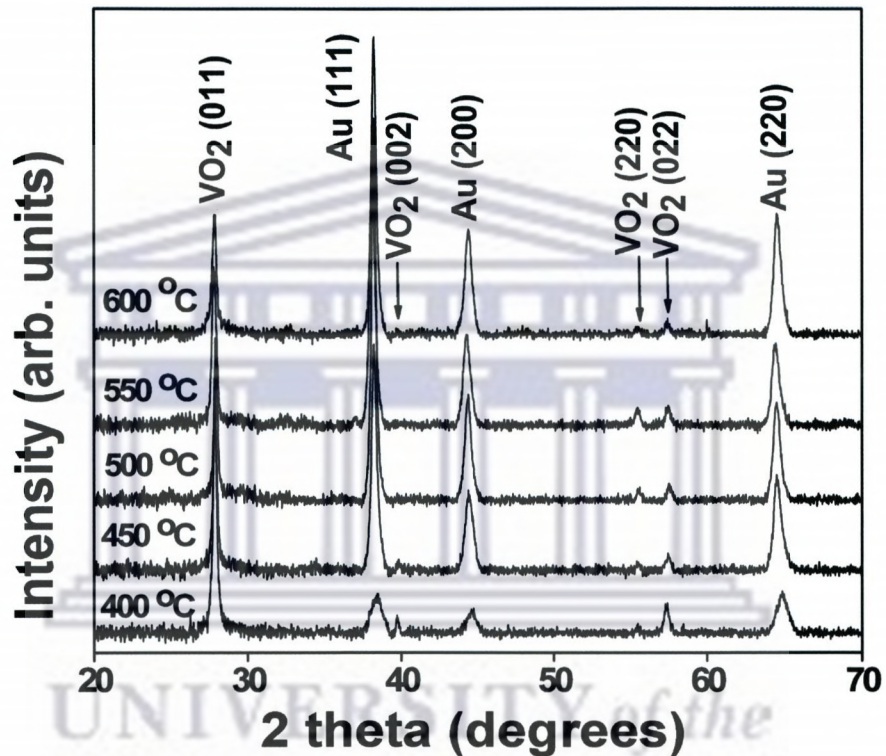


Figure 8.2: Indexed XRD patterns of Au-VO₂ nanocomposites (background-subtracted; JCPDS 82-661 for VO₂ monoclinic and JCPDS 04-0784 for gold face-centered cubic Fm3m) films sputtered at different substrate temperature ranging from 400 °C to 600 °C.

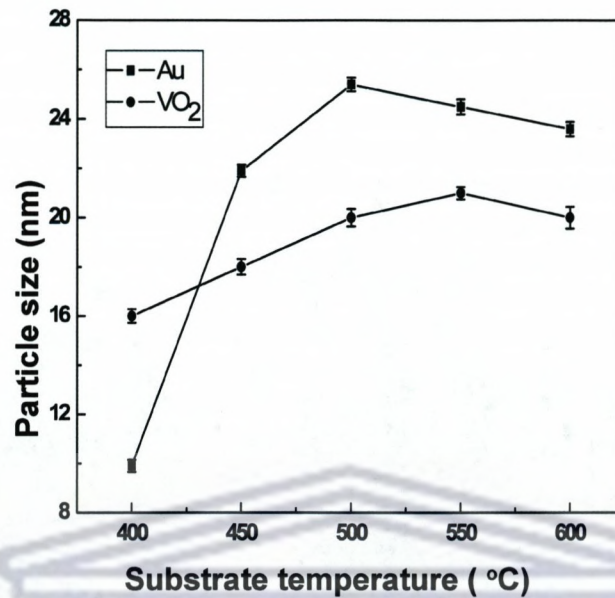


Figure 8.3: Relationship between the substrate temperature and the particle sizes of Au (square) and VO₂ (dot) estimated from Scherrer's formula.

8.3.2. Film surface morphology

AFM images of Au-VO₂ nanocomposite films were taken to determine dependence of surface morphology on substrate temperature. Fig. 8.4 (a) and (b) shows AFM images of samples sputtered at substrate temperature (T_s) of 400 °C and 600 °C, respectively. From the two-dimensional (2D) images it can be seen that the surface morphologies vary significantly among the films grown at different substrate temperature. It seems that the Au-VO₂ films sputtered at 400 °C as shown in Fig.8.4 (a), is composed of small conical-like islands dispersed with a low height of 6.14 nm, whereas those sputtered at higher substrate temperature of 600 °C as Fig. 8.4 (b) consist of very compact large conical-like islands with a significant height of 19.25 nm. The root mean square roughness shows 1.88 and 5.81 nm for $T_s = 400$ and 600 °C, respectively.

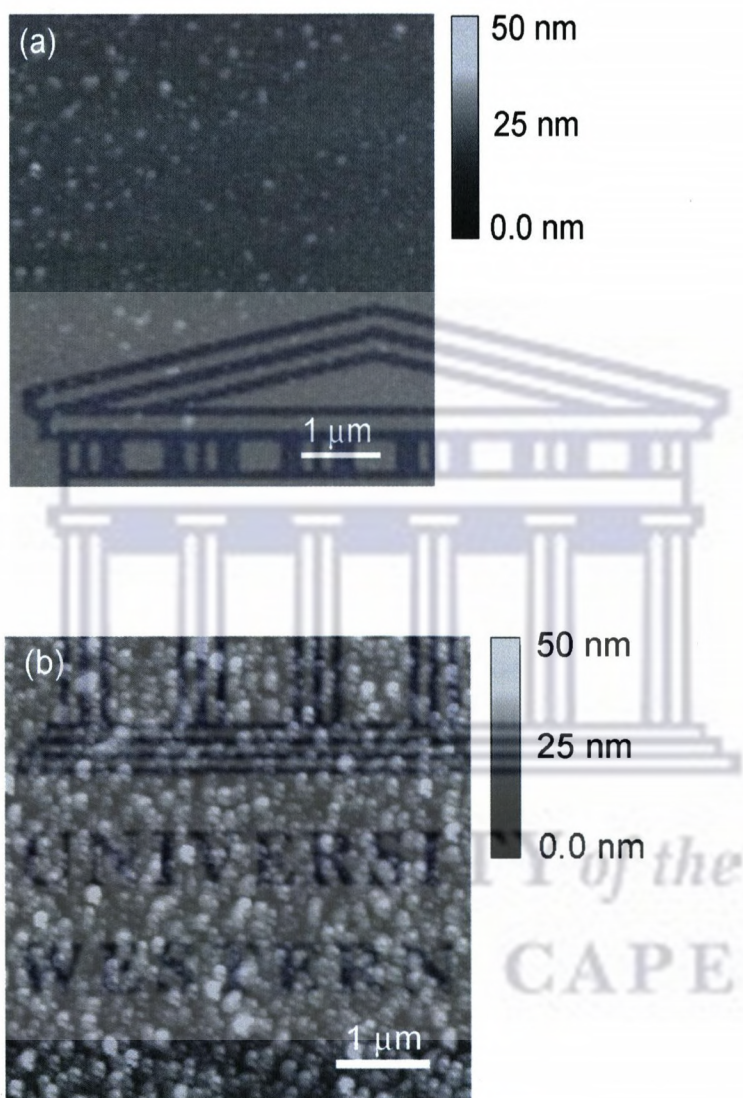


Figure 8.4: AFM topographic images of samples sputtered at substrate temperatures (a) 400 °C; (b) 600 °C.

8.3.3. Surface and interface analysis

Fig. 8.5 shows the typical X-ray reflectivity profile of Au-VO₂ films sputtered at 550 °C. It is clearly shown that, at small grazing angles, the incoming beam is totally reflected giving rise to the plateau of total reflection, over this region, usual interference fringes so called "Kiessig fringes" due to the finite film thickness are observed. The simulation of total reflection plateau and Kiessig fringes allow to deduce the mean electron density, total thickness, roughness at film surface and interfacial roughness. The extracted parameters from the electron density profile shown in inset of Fig. 8.5 are: $\sigma_0 = 3.8$ nm, $\sigma_1 = 2.4$ nm and $MED = 1.5 \text{ \AA}^{-3}$, where σ_0 , σ_1 represent roughness at film surface and film/substrate interface, respectively, and MED the mean electron density. To obtain a better fit, an interfacial layer of 1.8 nm thickness was taken into account. The surface roughness of Au-VO₂ composite thin film sputtered at 550 °C was compared by both methods XRR and AFM. AFM image of this film (not shown here) very similar to the one sputtered at 600 °C, revealed a compact large conical-like islands on the surface with significant height of 19.30 nm and a root mean square roughness (σ_{AFM}) of 5.94 nm. By comparing the roughness at film surface obtained by XRR ($\sigma_0 = 3.8$ nm) and AFM ($\sigma_{AFM} = 5.94$ nm), a huge difference is clearly observed. This can be explained by the fact that, the results of XRR and AFM measurements essentially depend on the irregularity of a surface and on the type of roughness. It is known that for very flat surfaces (with a root mean square roughness in the range of several angstroms) XRR and AFM give coincident roughness parameters [41,42]. When the surface has high irregularities such as knobs, islands with a complicated height distribution a significant discrepancy between roughness parameters obtained by both methods is observed [43,44]. Generally the surfaces having such irregularities are mostly non-Gaussian surfaces. The discrepancy between estimations of roughness parameters derived by both techniques for non-Gaussian surfaces is reported by Mironov et al. [45].

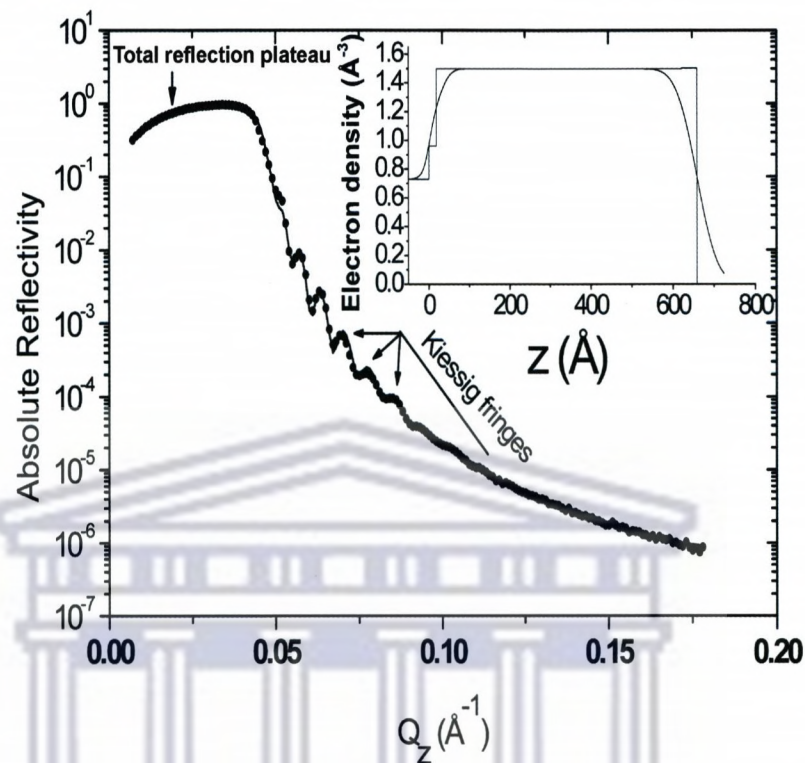


Figure 8.5: X-ray reflectivity profile of Au-VO₂ thin film on Corning glass substrate sputtered at 550 °C. The circles correspond to the experimental data and solid line the simulation.

8.3.4. Plasmonic properties

8.3.4.1. Surface plasmon resonance wavelength shift and thermochromic behavior

The optical transmittance spectra of the Au-VO₂ samples sputtered at different substrate temperatures are shown in Fig. 8.6. The spectral transmittance of the resulting films at low-temperature semiconducting phase and high-temperature metal phase are sharply contrasting in the near-infrared region due to the thermochromism properties of the host matrix VO₂. It can be noticed that, at higher substrate

temperature, the thermal switching of the semiconductor-metal transition is less pronounced. The peak absorption of small gold nanoparticles observed in the minimum of the spectral transmittance is clearly appeared in the visible region range of 590-670 nm for all sputtered samples. This peak absorption corresponds to the gold peak surface plasmon resonance (SPR). This resonant electromagnetic behavior of noble-metal nanoparticles is due to the confinement of the conduction electrons to the small particle volume. It is interesting to find that the surface plasmon resonance wavelength (λ_{SPR}) for all the samples blue shifts when the external temperature increases from 20 °C to 100 °C (heating process). Due to the reversibility of the phase transition of the host matrix, λ_{SPR} red shifts when the external temperature decreases from 100 °C to 20 °C (cooling process).

The influence of substrate temperature, T_s , on λ_{SPR} seems to be significant. Increase in T_s not only leads to a red shift of λ_{SPR} for both phases (semiconductor and metal) when the external temperature is below and above the transition temperature T_c , but also enhances the difference in λ_{SPR} , namely $\Delta\lambda_{\text{SPR}}$, between the two phases of VO_2 . For sample sputtered at $T_s = 400$ °C, the λ_{SPR} position is 635 nm below T_c , and 599 nm above T_c , with a difference of $\Delta\lambda_{\text{SPR}} = 36$ nm. In contrast, for sample sputtered at $T_s = 450$ °C, λ_{SPR} locates at 657 nm below T_c , and at 610 nm above T_c , with $\Delta\lambda_{\text{SPR}} = 47$ nm. However, for samples sputtered at 500, 550 and 600 °C the λ_{SPR} position was the same 665 nm below T_c , and 608 nm above T_c , with a difference of $\Delta\lambda_{\text{SPR}} = 57$ nm. This clearly indicates that the λ_{SPR} shifts to red as T_s increases. This red shift of λ_{SPR} with T_s increasing is consistent with an increase in the particle size of the Au nanoparticles revealed by XRD in the nanocomposite films; i.e., larger Au nanoparticles exhibit red-shifted SPR absorption [5,46]. A significant enhancement of $\Delta\lambda_{\text{SPR}}$ with increasing T_s results from the significant difference in dielectric constant of the host matrix VO_2 . In comparison to λ_{SPR} shift observed from Au- VO_2 nanocomposites synthesized by pulsed laser ablation [18] or gold-doped VO_2 produced by hybrid aerosol assisted and

atmospheric pressure chemical vapor deposition [27], there is a comparable shift of λ_{SPR} of 45 nm obtained from the sample sputtered at 450 °C and an enhanced shift of λ_{SPR} of 57 nm obtained from the sample sputtered at 600 °C.

In order to compare the phase transition characteristics of Au-VO₂ and pure VO₂ films, the transmittance at wavelength of 1100 nm at different external temperature stimuli was taken. All of the films show thermochromic behavior with transition temperature and width of hysteresis dependent on the substrate temperature. Fig. 8.7 shows the hysteresis behavior at 1100 nm of samples sputtered at 400 and 600 °C. The transition temperature is defined as the minimum of the derivative curve of the heating curve of the hysteresis loop. The hysteresis width was evaluated as the difference between the transition temperature of heating and cooling curve of the hysteresis loop. The sharpness and hysteresis width of 10 °C of Au-VO₂ thin films sputtered at 400 °C are comparable to those observed of pure polycrystalline VO₂ sputtered by ICMS at the same substrate temperature [24]. A wide hysteresis width of 20 °C obtained for Au-VO₂ film sputtered at 600 °C is probably due to the thermal stress. By comparison, samples of Au-VO₂ sputtered at substrate temperature range of 400-500 °C produced by ICMS showed a transition temperature of 60-70 °C and an optical hysteresis width of 10-15 °C similar to those produced by classical sputtering or Sol-gel [25, 26]. Those sputtered at high substrate temperatures 550-600 °C gave hysteresis width of 20 °C similar to gold-doped VO₂ films prepared by hybrid aerosol assisted-CVD [27]. A high transition temperature of 80 °C was obtained for Au-VO₂ sputtered at high substrate temperatures. A similar shift of transition temperature towards a higher temperature has been reported by Futaki et al. [47] for Ti or Ge doped VO₂.

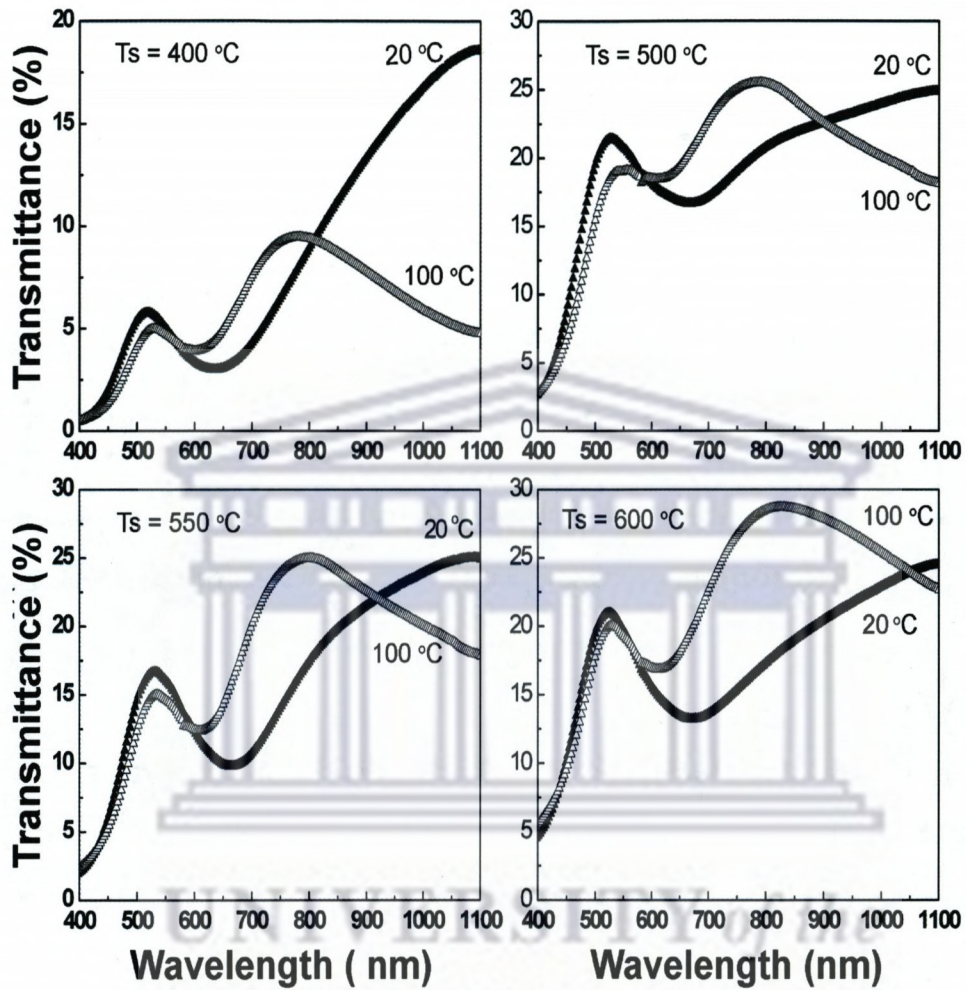


Figure 8.6: Optical transmittance (%) of Au-VO₂ thin films sputtered onto Corning glass at different substrate temperatures for spectra taken at temperature below and above the transition temperature ($T_c = 68\text{ }^\circ\text{C}$) of the host matrix VO₂.

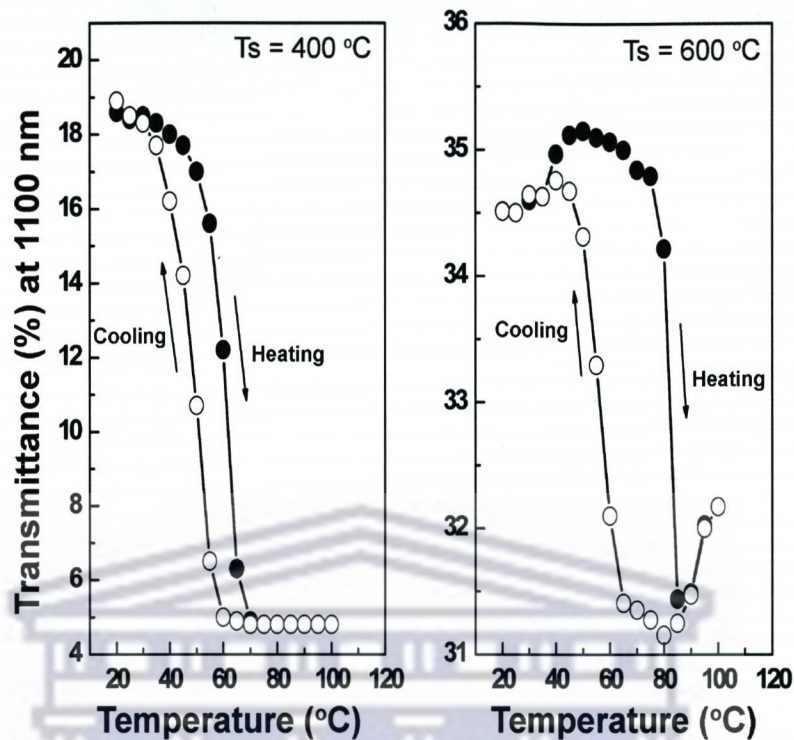


Figure 8.7: Transmittance at a wavelength of 1100 nm for Au-VO₂ thin films sputtered at 400 °C and 600 °C as a function of the external temperature stimuli.

8.3.4.2. Surface plasmon resonance hysteresis

Fig. 8.8 displays the absorbance versus wavelength of Au-VO₂ films sputtered at substrate temperature of 400 °C and 600 °C. The strength of the plasmon resonance peak of gold is clearly observed as well as the shift of plasmon resonance aforementioned. In order to study the external temperature dependence of λ_{SPR} , the absorbance measurements were taken during the rise and drop of external temperature. The wavelength at absorbance maximum corresponds to λ_{SPR} . Fig. 8.9. displays the temperature-dependent hysteresis of the λ_{SPR} . The SPR hysteresis behavior is similar to the optical hysteresis shown in Fig. 8.7. It can be seen that the Au-VO₂ sputtered at 400 °C revealed a hysteresis width of 10 °C with an abrupt variation of λ_{SPR} at 65 °C. The sharpness of the variation of the λ_{SPR} in the vicinity of

the transition temperature of single crystal VO₂ confirms the high quality of the host matrix VO₂. In comparison to SPR hysteresis observed from Au-VO₂ nanocomposites produced by laser ablation [18], the hysteresis width, abrupt variation of λ_{SPR} at 65 °C and sharpness are almost the same. The sample sputtered at high substrate temperature of 600 °C revealed a wide SPR hysteresis width of 20 °C and it indicates an abrupt fall of λ_{SPR} around 85 °C. In comparison to SPR hysteresis observed from Au-VO₂ sputtered at 600 °C produced by hybrid aerosol assisted-chemical vapor deposition [27], the hysteresis width of 20 °C is similar and comparable. These anomalous SPR hysteresis characteristics of Au-VO₂ films sputtered at higher substrate temperatures could be due to the thermal stress or microstructures of the synthesized films. Since, it is commonly assumed in the VO₂ thin-film literature that, given a controlled oxide stoichiometry, the sharpness of the phase transition [48] as well as its hysteresis width and critical temperature are dependent on the stress [49] and microstructure of the films [50].

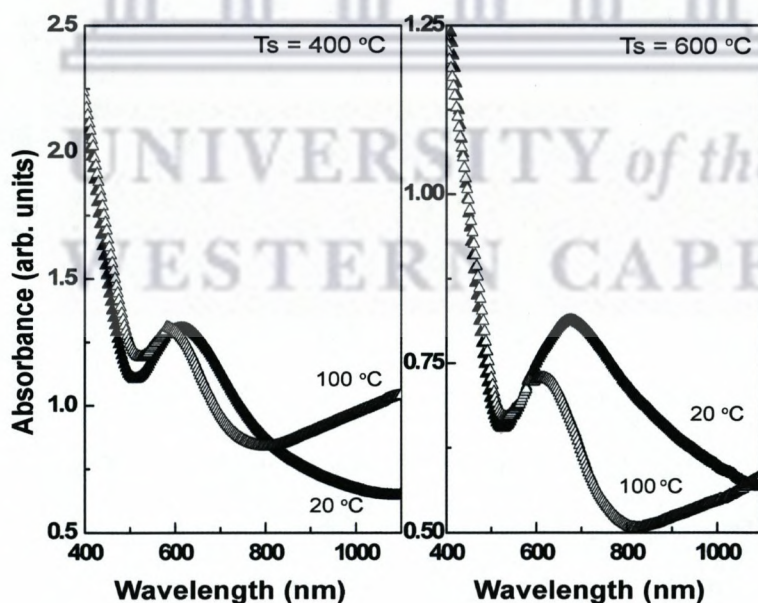


Figure 8.8: Absorbance spectra of the Au-VO₂ nanocomposite films sputtered at 400 °C and 600 °C. Measurements taken below and above the transition temperature $T_c = 68$ °C.

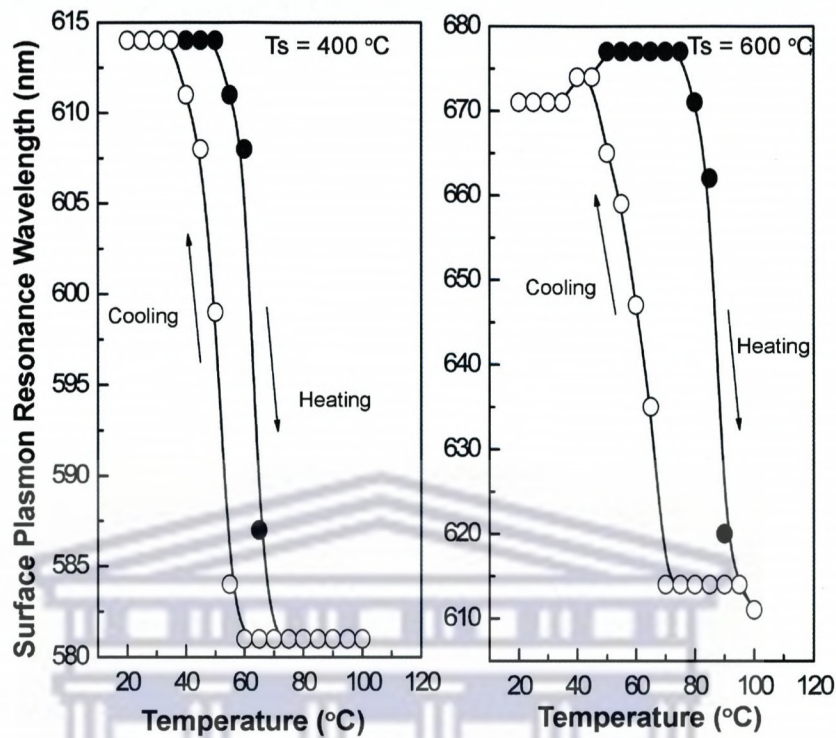


Figure 8.9: Variation of surface plasmon resonance wavelength as function of external temperature stimuli of Au-VO₂ samples sputtered at 400 °C and 600 °C.

8.4. Conclusion

"Smart" thermochromic nanocomposite thin films consisting of gold nanoparticles embedded in a thermochromic VO₂ matrix were prepared by ICMS. The structural, morphological, and plasmonic properties of Au-VO₂ synthesized films have been studied. The plasmonic properties and thermochromic behavior of the synthesized nanocomposites films of Au-VO₂ by ICMS are comparable to those seen previously with Au-VO₂ thin films grown by laser ablation, classical sputtering or other conventional coating techniques. This coating technology offers advantages over others physical vapor deposition such as laser ablation, planar reactive magnetron sputtering. It promises to be fully reproducible and suitable for the synthesis of Au-VO₂ composites thin films.

8.5. References

- [1] I. Tanahashi, H. Inouye, A. Mito, *Jpn. J. Appl. Phys.* 42, (2003) 3467.
- [2] H. Liao, W. Wen, G.K.L. Wong and G. Yang, *Opt. Lett.* 28, (2003) 1790.
- [3] K.A. Willets, R.P. Van Duyne, *Annu. Rev. Phys. Chem.* 58, (2007) 267.
- [4] C.L. Haynes and R.P. Van Duyne, *Nanosphere*, *J. Phys. Chem. B* 105, (2001) 5599.
- [5] S.A. Maier, *Plasmonics: Fundamentals and Applications*, Springer, 2007, p. 74-177.
- [6] M.B. Cortie, A. Maarooof and G. Smith, *Symposium R: Meta-Materials at the Milli, Micro and Nanoscale*, Materials Research Society Fall Conference, Boston, USA, November 28-30, 2006, paper R6.4.
- [7] S. Enoch, R. Quidant, G. Badenes, *Opt. Express.* 12, (2004) 3422.
- [8] M.B. Cortie, A. Dowd, N. Harris, and M.J. Ford, *Phys. Rev. B* 75, (2007) 113405.
- [9] R. Gupta, M.J. Dyer, and W.A. Weimer, *J. Appl. Phys.* 92, (2002) 5264
- [10] T.R. Jensen, M.D. Malinsky, C.L. Haynes, and R.P. Van Duyne, *J. Phys. Chem. B* 104, (2000) 10549.
- [11] G. Xu, M. Tazawa, P. Jin, S. Nakao, and K. Yoshimura, *Appl. Phys. Lett.* 82, (2003) 3811.
- [12] U. Kreibig and M. Vollmer, *Optical Properties of Metal Clusters*, Springer, Berlin, 1995, p.532.
- [13] S.A. Maier and H.A. Atwater, *J. Appl. Phys.* 98, (2005) 011101.
- [14] M. Hirai, A. Kumar, *J. Appl. Phys.* 100, (2006) 014309.
- [15] G. Xu, Y. Chen, M. Tazawa, P. Jin, *J. Phys. Chem. B* 110, (2006) 2051.
- [16] J.Y. Suh, E.U. Donev, D.W. Ferrara, K.A. Tetz, L.C. Feldman and R.F. Haglund Jr., *J. Opt. A: Pure Appl. Opt.* 10, (2008) 055202.
- [17] M. Maaza, O. Nemraoui, C. Sella, A.C. Beye, *Gold Bull.* 38, (2005) 100.

- [18] M. Maaza, O. Nemraoui, C. Sella, A.C. Beye, B. Baruch-Barack, *Opt. Commun.* 254, (2005) 188.
- [19] Z. Wang, G. Chumanov, *Adv. Mater.* 15, (2003) 1285.
- [20] Y. Ohko, T. Tatsuma, T. Fujii, K. Naoi, C. Niwa, Y. Kubota, A. Fujishima, *Nat. Mater.* 2. (2003) 29.
- [21] O.P. Mikheeva and A.I. Sidorov, *Tech. Phys.* 48, (2003) 602.
- [22] H.W. Verleur, A.S. Barker Jr, and C.N. Berglund, *Phys. Rev.* 172, (1968) 788.
- [23] H. Kakiuchida, P. Jin, S. Nakao, M. Tazawa, *Jpn. J. Appl.* 46, (2007) L113.
- [24] J.B. Kana Kana, J.M.Ndjaka, P.Owono Ateba, B.D.Ngom, N.Manyala, O. Nemraoui, A.C. Beye, M.Maaza, *Appl. Surf. Sci.* 254, (2008) 3959.
- [25] G. Xu, C.M. Huang, M. Tazawa, P. Jin, D.M. Chen, and L. Miao, *Appl. Phys. Lett.* 93, (2008) 061911.
- [26] E. Cavanna, J.P. Segaud, and J. Livage, *Mater. Res. Bull.* 34, (1999)167.
- [27] R. Binions, C. Piccirillo, R.G. Palgrave, and I.P. Parkin, *Chem. Vap. Deposition* 14, (2008) 33.
- [28] I. Safi, *Surf. Coat. Technol.* 127, (2000) 203.
- [29] J. Musil, P. Baroch, J. Vlcek, K.H. Nam, J.G. Han, *Thin Solid Films*, 475, (2005) 208.
- [30] J.A.Thornton and A.S.Penfold, *Cylindrical Magnetron Sputtering in: Thin films Processes*, edited by J.L. Vossen and W. Kern, Academic Press, New-York, 1978, p75.
- [31] D.A. Glocker, *Proceedings of the Annual SCV Technical Conference* (1995), p. 298.
- [32] D.E. Siegfried, D. Cook, Ion Tech, Inc., Ft.Collins, CO; D.Glocker, Isoflux,Inc., Rush, NY, 39th Annual Technical Conference Proceedings of the Society of Vacuum Coaters 505/856 (1996) 97.

- [33] J. A. Thornton and V. Hedgcoth, *J. Vac. Sci. Technol.* 12, (1975) 93.
- [34] J. T. Cheung, I.M. Gergis, J. James and R. E. DeWames, *Appl. Phys. Lett.* 60, (1992) 3180.
- [35] J.A. Greer and H. J. Van Hook, *Mater. Res. Soc. Symp. Proc.* 191, (1990) 171.
- [36] V.W. Lindberg, A.R. Woodard and D.A. Glocker, *Surf. Coat. Technol.* 133/134, (2000) 484.
- [37] A.A. Pradhan, S.I. Shah, K.M. Unruch, *Rev. Sci. Instrum.* 73, (2002) 3841.
- [38] E. Xenogiannopoulou, P. Aloukos, S. Couris, E. Kaminska, A. Piotrowska, E. Dynowska, *Opt. Com.* 275, (2007) 217.
- [39] A.E. Delahoy, S.Y. Guo, C. Paduraru and A. Belkind, *J. Vac. Sci. Technol. A* 22(4), (2004) 1697.
- [40] B.D. Cullity, *Elements of X-ray diffraction*, 2nd edn, Addison-Wesley, Reading, Mass.1978, p.102.
- [41] A.A. Bukharaev, E.F. Kukovitski, D.V. Ovchinnikov, N.A. Sainov, and N.I. Nurgazizov, *Phys. Solid State* 39, (1997) 1846.
- [42] C. Teichert, J.F. Mackay, D.E. Savage, M.G. Lagally, M. Brohl, and P. Wagner, *Appl. Phys. Lett.* 66, (1995) 2346.
- [43] A.A. Fraerman, S.V. Gaponov, B.A. Gribkov, V.L. Mironov, and N.N. Salashchenko, *Phys. Low-Dimens. Semicond. Struct.* (2002) 79.
- [44] V.W. Stone, A.M. Jonas, B. Nysten, and R. Legras, *Phys. Rev. B* 60, (1999)5883.
- [45] V.L. Mironov, O.G. Udalov, B.A. Gribkov, and A.A. Fraerman, *J. Appl. Phys.* 104, (2008) 064301.
- [46] K.L. Kelly, E. Coronado, L.L. Zhao, G.C. Schatz, *J. Phys. Chem. B*.107, (2003) 668.
- [47] M. Futaki and M. Aoki, *Jpn. J. Appl. Phys.* 8, (1969) 1008.

- [48] M. Borek, F. Quian, V. Nagabushnam, and R.K. Singh, *Appl. Phys. Lett.* 63, (1993) 3288.
- [49] F.C. Case, *J. Vac. Sci. Technol. A* 2, (1984) 1509.
- [50] J.F. De Natale, P.J. Hood, and A.B. Harker, *J. Appl. Phys.* 66, (1989) 5844.



UNIVERSITY *of the*
WESTERN CAPE

Chapter 9

CONCLUSIONS AND OUTLOOK

The findings associated with this thesis have added to the understanding of the VO₂ nanoscale thin films and active optically nanosystem Au-VO₂. The influence of the growth parameters such as thickness, substrate temperature on the microstructure, morphology and optical properties of VO₂, host matrix, thin films was systematically investigated. It was revealed that the semiconductor–metal phase transition temperature considerably decreases as film thickness increases in particular for the film with thickness greater than 100 nm. The process parameters, especially the substrate temperature and oxygen partial pressure can strongly influence the stoichiometry of the system, drastically altering its material properties. Hence high substrate temperatures were revealed to induce an anomalous shift of transition temperature towards higher temperature.

From the conductive Atomic Force Microscopy associated with scanning tunneling spectroscopy (STS) spectra, we were able to distinguish metallic and insulating regions by nano-imaging and by probing the band gap in order to prove the phase's coexistence in the metal-insulator transition of VO₂ thin films.

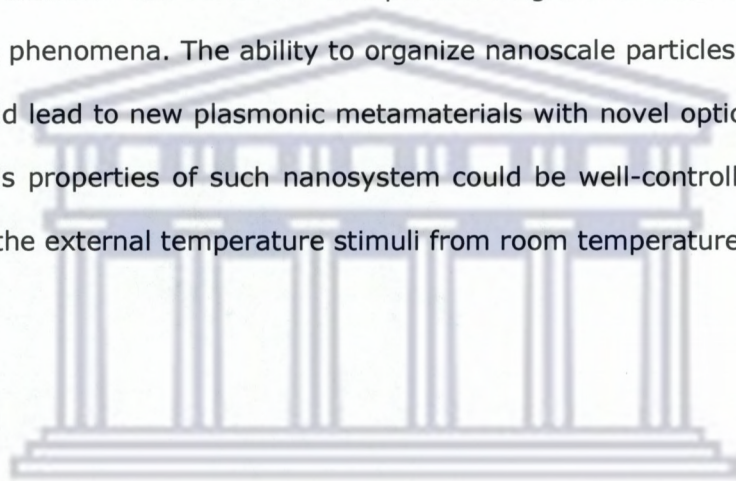
The optical constants of a vanadium dioxide (VO₂) thermochromic film deposited on glass substrate by spectroscopic ellipsometry in wavelength range from 380 nm to 1700 nm were determined and the reversible tunability of refractive index and extinction coefficient with external temperature stimuli was well-observed.

Using a novel growth technique called radiofrequency inverted cylindrical reactive magnetron sputtering or Hollow cathode sputtering (ICMS), we have successfully prepared highly oriented nanocrystalline Au-VO₂ composite thin films on glass substrates at various growth temperatures ranging from 400 to 600 °C. The influence of the growth parameters on the microstructure, morphology, interface and plasmonic properties of Au-VO₂ thin films was systematically investigated. The reversible tenability of surface plasmon resonance with external temperature stimuli is clearly shown. The technological issues of our novel growth technique have been raised and compared to other conventional physical vapor deposition techniques such as pulsed laser deposition (PLD) and planar reactive magnetron sputtering. ICMS was revealed to be a promising and suitable candidate growth technique of such complex nanocomposites because of its capability to eliminate all the drawbacks encountered with planar reactive magnetron sputtering or PLD and also its up-scalability and reproducibility.

For the continuation of this work in pure condensed matter field, we are suggesting the synchrotron radiation experiments. Firstly, the comparative study of temperature dependent metal-insulator (M-I) phase transition of the valence band density of states (DOS) in VO₂ and Au-VO₂ thin films using Ultraviolet Photoemission Spectroscopy (UPS). Since this transition is a bulk property, to study carefully the change in the DOS of the above thin films with thermal cycling across the M-I phase transition, a low photon energy source is needed in order to be mainly sensible to the bulk properties. This comparative study using UPS of pure VO₂ and Au-VO₂ will be very helpful to point out the differences in the electronic structure by embedding gold nanoparticles in the host matrix VO₂. Secondly, a photoemission study of Au-VO₂ nanostructure using synchrotron radiation can be suggested. In this case, the metal-matrix interaction in Au-VO₂ nanocomposite will be studied using soft X-ray photoelectron spectroscopy. However, the position of Au 4f peaks depends strongly on the chemical/electronic

environment surrounding it, hence it is necessary to check if Au nanoparticles embedded in the matrix of VO₂ remain in elemental state without forming any oxide species on the surface or alloy, or Au-V mixed oxide.

In nanotechnology point of view, the novel tunable plasmonic metamaterials (negative permeability and refraction at visible wavelengths) can be targeted by patterning gold nanoparticles arrays on VO₂ thin films deposited on glass substrate with different varying inter-distance (center to center) for example 70 nm, 140 nm and 210 nm. The gold nanoparticle diameter can be 25 nm and particle height of 17 nm. Such structure display plasmonic phenomena. The ability to organize nanoscale particles over multiple length scales could lead to new plasmonic metamaterials with novel optical properties. The metamaterials properties of such nanosystem could be well-controlled and tuned by just changing the external temperature stimuli from room temperature to 100 °C.



UNIVERSITY *of the*
WESTERN CAPE